Uncovering the Nature of Various Scattering Sites, Extended and Magnetic, in $Bi_2Sr_2CaCu_2O_{8+\delta}$ using Atomic Resolved Spectroscopy by

Eduardo Manuel Calleja

B.S., University of Florida, 2005

M.S., University of Colorado at Boulder, 2011

A thesis submitted to the

Faculty of the Graduate School of the

University of Colorado in partial fulfillment

of the requirement for the degree of

Doctor of Philosophy

Department of Physics

2013

This thesis entitled:
Uncovering the Nature of Various Scattering Sites, Extended and Magnetic, in $Bi_2Sr_2CaCu_2O_{8+d}$ using Atomic Resolved Spectroscopy written by Eduardo Manuel Calleja
has been approved for the Department of Physics

_____
Dr. Kyle P. McElroy

_____
Dr. Minhyea Lee

Date_____

The final copy of this thesis has been examined by the signatories, and we
Find that both the content and the form meet acceptable presentation standards
Of scholarly work in the above mentioned discipline.

Calleja, Manuel Eduardo (Ph.D., Physics)

Uncovering the Nature of Various Scattering Sites, Extended and Magnetic, in $Bi_2Sr_2CaCu_2O_{8+d}$ using Atomic Resolved Spectroscopy

Thesis directed by Assistant Professor Kyle P. McElroy

The superconducting cuprates represent one of the most intriguing condensed matter systems due to their potential to impact future technologies. As such they have garnered a substantial amount of theoretical and experimental interest over the last 27 years. In spite of this fact, many questions remain unanswered such as the nature of the superconducting pairing mechanism and the origin of the structure of their phase diagram. Spectroscopic Imagining Scanning Tunneling Microscopy (SI-STM) has proven to be an extremely useful probe for studying these materials due to the fact that SI-STM allows for the simultaneous measurement of the real space electronic states with atomic precision and the nature of the momentum K-space states.

In this thesis the design and construction of a 5K SI-STM designed for looking at cleavable surfaces, such as the superconducting cuprates, is presented. The k-space nature of the electronic states on Bi2212, as measured by SI-STM, seems to indicate that there is a portion of the Fermi surface which does not super conduct. However, evidence from other probes is mixed. In this thesis, a framework which explains how these "Fermi Arcs" can arise from experimental effects is presented. Followed by an experiment on Bi2212 that shows how one could mistakenly see this "Fermi Arc" signal by adjusting simple experimental dials.

In addition, in this thesis we present a comprehensive study of Bi2212 samples where Fe has been substituted for Cu in the CuO plane. This study reveals a highly localized bound state, with the density of states showing a large asymmetry favoring the hole side. The density of states can be interpreted within a co-tunneling picture which is only valid if the impurity is coupled to the conduction electrons resulting in a local Kondo-like effect. This is the first time a Kondo-like impurity is observed in a d-wave superconductor. Comparisons to experiments where Kondo impurities are observed in s-wave superconductors are presented as well.

This thesis is dedicated to my late grandmother Herminda “Mimi” Rodrigez and my grandmother Adelfa “Mami” Gonzales, both of which possess the unique ability to make my troubles disappear with a glass of milk.

ACKNOWLEDGEMENTS

I truly believe we are products of the environment and the people that surround us. I have been extremely fortunate to have been surrounded by some remarkable people who have made this journey possible. There are definitely too many people to mention and I am sure, that in spite of my best efforts, I will leave some people out. So let me start off by saying that if you have been part of my life over the last 16 years (since the first time I stepped into a physics research laboratory), I deeply thank you for helping me get to where I am at today.

Any mention of my initial journey into science has to begin with my 6 th grade teacher Mrs. Maria Castellanos, whose irrational faith in my scholarly ability was the spring board to my current success, to her I say thank you and this work would not be possible without your inspiration and love.

I was then blessed to attend MAST Academy where 3 professors would forever change my thinking about science and research. They are Dr. Julie Hood, Dr. Wafa Khalil, and Mr. Joseph Zowadny. They held me to the highest standards possible and involved me in professional physics research at age 16. Without their influence I don't believe I would have ever pursued a career in science. I thank them very much for never letting me take a day off.

I then attended the University of Florida, where I worked in Professor Yoonseok Lee's lab performing experiments in low temperature physics. It was

without question one of the greatest experiences of my young career. I enjoyed coming to work every day and it led me to realize that I wanted to pursue a career in physics. I thank him for always having such confidence in me and being and excellent teacher, I learned a tremendous amount from working with Yoonseok.

I then went on to attend the University of Colorado at Boulder for my ph.d studies and this is where I have resided over the last 8 years of my life. To say the journey has always been a good one will be to lie. There have been highs and lows and I want to take this opportunity to thank the people who have been with me through the highs and the lows.

Let me first begin my thanking the folks who would play soccer and basketball with me on Fridays the first couple fo years of graduate school. They are Marcio Miranda, Fan-Chi Lee, and Ricardo Jimenez, and Simon Braun. I very much need to thank Chester Rubbo for being my workout partner and a great advocate during my graduate studies.

I'd also like to thank my distant friends Mike Hetzel, Kent Bitzer, Christopher Del Rosario, and Christina Choi. You guys made my nights tolerable and a lot of fun. I think graduate school would have been a complete disaster without you guys.

I'd like to thank the undergraduates I have gotten he pleasure of working with throughout the years, Alex Cooper, Daniel Schiffman, Donald Royer, William Kent, Tony Zhou and Thomas Myers. Some of you were absolutely impressive with

your work ethic, others were not so much. Regardless I enjoyed working and getting to know all of you.

To my cousin George Calleja who no matter the distance always allows me to call him, regardless of hour, for advice. Thank you for always being there for me.

To my brother Alejandro Calleja, I thank for being my absolute best friend and confidant throughout all of these years. Me and my brother are 6 years apart and I never thought that he and I would grow as close as we have over the last 8 years. In many ways the trials and tribulations of life have brought us closer than one could ever imagine.

To my grandmother Adelfa Gonzales, who's love and support for me never seizes to amaze me. She always seems to make all my troubles disappear just by simply offering me a glass of milk.

Without question my largest supporters during this time has been my parents, Adelfa Estrada and Ricardo Calleja. They have not enjoyed having me be this far apart from them and getting to see them as little as I do. But they have always supported and encouraged my endeavors. I truly hope that I have made them proud.

Of course this work would not be possible without the support of my advisor Dr. Kyle P. McElroy. Me and Kyle don't often see eye to eye, but we have learned to work very well with each other. Kyle has challenged me every day and because of it I am the scientist I am today. I thank him for always pushing me and not ever accepting anything less than my very best.

I would also like to thank Jixia Dai who has been my lab mate all of these years. Jixia is an excellent scientist and I have learned a tremendous amount from working with him. This would work would not be possible without his help and I very much thank him for being an excellent co-worker and a great friend.

Finally I would like to thank Ms. Sarah D. Urriste. She is my former partner in crime and without question on of my closet and dearest friends. Without her love and support these last 8 years there is absolutely no question in my mind that I would not be here much less finish this thesis.

There are many more people who have helped me get to where I am certainly I'd like to thank my thesis committee of Dr. Minyeah Lee, Dr. Daniel Dessau, Dr. Charles Rodgers, and Dr. Scott Bunch. All of which have helped me in my endeavors countless times throughout the years.There are countless other people who have made this day possible and although I am not able to thank you in writing I thank you in spirit.

CONTENTS

CHAPTER
1 INTRODUCTION 1

1.1 Coopers Problem.....1

1.2 BCS Theory.....4

1.3 Green's Function.....6

1.4 Conventional Superconductors.....7

1.5 High Temperature Superconductors.....9

1.6 Probing the High T_c cuprates.....14

2 SCANNING TUNNELING MICROSCOPY.....17

2.1 Introduction.....17

2.2 Tunneling Current.....18

2.3 Topography.....20

2.4 Walking and STM body.....26

2.5 Noise considerations.....30

2.6 Spectroscopic Data Taking.....33

3 QUASIPARTICLE INTERFERENCE.....41

3.1 Theory.....41

3.2 Comparison to Angle Resolved Photo Emission.....46

3.3 Simple QPI simulation.....49

3.4 Matrix Element.....51

3.5 Finite k-space resolution.....53

3.6 Experimentally Simulating Fermi Arcs.....55

3.7 Conclusion.....56

4 MAGNETIC IMPURITIES IN Bi2212.....58

4.1 Impurity Studies in Bi2212.....58

4.2 STM studies on magnetic impurities.....59

4.3 Investigation of Fe impurities in Bi2212.....66

4.4 Interplay of Fe atoms with Superconductivity.....77

4.5 Understanding the Spatial Structure.....80

4.6 Zero Bias Enhancement.....89

4.7 Understanding the Spectra..... 92

4.8 Conclusion.....99

REFRENCES.....101

FIGURES

Figure

1.1: A typical excitation in Cooper' s problem [17]……2

1.2: A graphical depiction of how phonon mediated superconductivity manifest itself physically……..5

1.3: A graphical depiction of a BCS s-wave order parameter in k-space. ……8

1.4: Resistivity of Mercury as a function of temperature, the transition from normal to superconductor happens at 4.2K [1]……..8

1.5: Highest superconducting transition temperatures from 1911 to 2000, red indicates materials for which noble prizes were awarded. ……9

1.6: Unit cells for (a) $La_{2-x}Sr_xCuO_4$ (b) $YBa_2Cu_3O_{7-\delta}$ (c) $Bi_2Sr_2CaCu_2O_{8+\delta}$ 11

1.7: Summery of the different types of disorder in the cuprate family from [11].12

1.8: A toy model of the cuprate phase diagram. Where AFI stands for anti-ferromagnetic insulator, PG stands for pseudogap, d-SC stands for d wave superconductor, NFL stands for non-Fermi liquid, M stands for metal, all of these phases are found in all cuprates but at slightly different doping. Evidence exist for the following three phases in Bi2212, SG which stands for spin glass, CO which stands for charge ordering, and fl-SC which stands for fluctuating superconductor. Note this is not a generic model of the cuprate phase diagram. ……13

1.9: The different energy scales measured by different probes in Bi2212 as reported in [14]……15

2.1: Schematic showing the local density of state (LDOS) at a particular location on the sample, which appears on the left hand side, the LDOS of the tip, which appears on the right hand side. The middle region is a vacuum region which acts as a potential barrier between tip and sample, ε_F is the Fermi energy of either tip or sample. When a bias voltage eV is applied to the sample the Fermi energy of the sample shifts relative to the Fermi energy of the tip, allowing the electrons to tunnel into a particular energy window of the LDOS of the sample, which is the Fermi energy of the sample minus the applied bias voltage, this energy window is labeled $e\delta V$……18

2.2: A) Scan tube piezo form the PI Corporation showing the z extension. B) Scan tube piezo form the PI Corporation showing the 4 electrodes for x-y deflection..22

2.3: STM topography on $NbSe_2$ at T=5.2K, with set up condition I_{set}=100 pA and V_{bias}=-100 mV.....24

2.4: The red dots indicate the current as a function of z piezo distance. The blue line displays the fit to the data with the functional form $= A * e^{-\frac{x}{x_0}} + c$. Where for this data $x_0 = 0.53$ Å which implies $\phi = 4.1\ eV$.....26

2.5: Schematic showing the assembly of our homebuilt piezo stacks. The grey pads represent individual piezos and the copper colored pads represent thin copper foil used as electrodes between individual piezos.....28

2.6: A) An illustration of the coarse approach mechanism using the shear piezo actuators, where each leg is shown firing at different times time. B) The voltage profiles applied to each piezo actuator. [32].....29

2.7: A) STM body viewed from the front. B) STM viewed from the top with the titanium cover removed to show the tip holder, scan tube holder, shear piezos, and tip holder as indicated in the figure.....29

2.8 : Schematic of home built current amplifier used for measuring the tunneling current in our home built 5.2K STM.....31

2.9: Typical averaged LDOS of an OP91K Bi2212 sample. Taken with set up conditions of I=200pA and V=-200mV.....35

2.10: A typical gap map of an OP91K Bi2212 sample taken over a 15nm x 15nm field of view. With the set up condition of I=200 pA and V=-200mV. The field of view shows a gap variation of roughly 35 mV over a length scale of roughly 3nm.....36

2.11: A) Topographic image of UD Bi2212 with 1.5% Fe doping over a 6 nm x 6nm FoV with set up conditions of I=10 pA and V=-1V. B) $LDOS(\vec{r}, -1V)$ over the same FoV as the topography, where the white spots represent areas of increased spectral weight believed to be dopant oxygen atoms.....39

2.12: Typical line cut on OP Bi2212 with 0.5% Fe dopant. The inset shows the $LDOS(\vec{r}, 23.5V)$ of an Fe impurity. The red line indicates the line over which the spectra where acquired, there are 1000 spectra displayed in the figure with initial set conditions I=100 pA and V=-100 mV, the bright red spot on the line cut indicates the Fe impurity.....40.

3.1: The FT-STM measured by [36] in an optimally doped Bi2212 sample…….42

3.2: Simulated Bi2212 fermi surface using the band structure from [38]…….43

3.3: Simulated A(k,w) showing the superconducting banana's around the hole pockets of the Fermi surface given in figure 3.2……..44

3.4: the seven unique wave vectors formed by quasi particles scattered from the edges of the superconducting banana [36]……45

3.5: The Fermi surface and k-space gap reconstruction from [36]……..46

3.6: (A) The reconstructed k-space gap from [39], normalized by the gap maximum. (B) The maximum gap as a function of number of holes……..47

3.7: (A)The reconstructed upper quarter of the Fermi surface from [41] across 6 different hole doping's. (B) The reconstructed k-space gap across 6 different doping's, offset for clarity……..48

3.8: The reconstructed k-space gap of a underdoped Tc=37K sample as a function of temperature [42]……49

3.9: (A) Raw QPI data of an optimally doped sample. (B) Simulated data using the simple model……50

3.10: (A) Reconstructed k-space gap from the basic simulation as a function of broadening. (B) Reconstructed Fermi surface from the basic simulation as a function of broadening……...51

3.11: (A) Raw QPI data of an optimally doped sample. (B) Simulated data using the simple model with the hopping matrix element……...52

3.12: (A) Reconstructed k-space gap from the basic simulation with the hopping matrix element. (B) Reconstructed Fermi surface from the basic simulation with the hopping matrix element……53

3.13: (A) Raw QPI data of an optimally doped sample. (B) Simulated data using the simple model with the hopping matrix element and k space broadening……54

3.14: (A) Reconstructed Fermi surface (B) element. Reconstructed k-space gap……..54

3.15: A simple schematic of how increasing the bias modulation effectively broadens the dI/dV signal. Where the red line represents the I-V characteristic of Bi2212 and the blue line indicates the bias modulation of some voltage amplitude Vm and δI is the amount of current measured after it has been broadened……55

3.16: A) Reconstructed Fermi surface using q1 and q3 on a UD58K sample at two different bias modulations, where the blue circles represent a bias modulation of 6 meV and the red squares represent a bias modulation of 2 meV. The black line represents the computed Fermi surface of Bi2212 using a tight binding model. B) Reconstructed k-space gap from the same UD 58K sample at two different bias modulations. The green line represents the fit to Eq. 3.5. The data was taken with a set up condition of I_{set}=200 pA and V_{bias}=-200 mV……..56

3.17: Comparison of nodal avoidance from [42] with the simulated data. The simulated data is given by the blue squares and its axis is displayed on the left hand side and the data from [42] is shown as red circles and its axis is displayed on the left hand side.....57

4.1: A) LDOS(E) of a Ni impurity in Bi2212 at different locations, the top spectra shows the LDOS on site. The top inset shows the positive $LDOS(E,\vec{r})$ at the impurity energy and the bottom inset shows negative $LDOS(E,\vec{r})$. B) LDOS(E) of a Zn impurity in Bi2212, the black spectra is the normal spectra in Bi2212. The inset shows $LDOS(E,\vec{r})$ for a Zn impurity……..59

4.2: The LDOS on a Co atom and off a Co atom from [55]. The spectra off the Co atom shows a flat DOS as expected for a Au(111) surface where the LDOS on the Co atom shows evidence of a Fano resonance……..60

4.3: Schematic displaying a co tunneling process between tunneling into a continuum (E_c) and an impurity (E_b) where when tunneling into the impurity the electron tunnels through the impurity into the continuum with broadening ν. Where tc represents the tunneling amplitude into the continuum and t_f represents the tunneling amplitude into the impurity……..61

4.4: A) The measured dI/dV from [52] using superconducting-insulator-superconducting (SIS) tunneling. B) The deconvolved dI/dV spectra measured by [52], this represents the dI/dV of the surface. C) The dI/dV measured at higher energies by [52] indicating a non-particle number conserving asymmetry thought to be a Fano resonance……..63

4.5: Measurements made from [52], represented as black dots, compared to the theoretical model of [57]. The Kondo temperature was a extracted from non-

superconducting spectra and the bound state energy was measured as the energy location of the enhanced coherence peak……65

4.6: A) Topographic image of the intial 24 nm x 24 nm area surveyed on OP83K with a nominal Fe concentration of 0.05% and a set up condition of I=100 pA and V=-100 mV. B) The concurrent LDOS map taken over the same field of view and set up condition displayed at a bias voltage of 22 mV…….....67

4.7: Individual spectra on 17 different Fe impurities, note that the energy location of the bound state shifts as a function of gap. The set up condition was I=100 pA and V=-100mV, taken with a 2mV bias modulation, and with an energy resolution of 1.56 mV/point……68

4.8: $K(\vec{r})$ for the FOV in figure 1A, the bright white spots represent the signature of an Fe impurity……70

4.9: A) Topograph of a 15 nm x 15 nm FOV taken with I= 100 pA and V=-100 mV. B) LDOS map taken concurrently with figure A, with an energy layer of 22.5 mV dispayed. C) Computed $K(\vec{r})$ for the FOV shown in figure A……70

4.10: The relationship between the electron peak (Δ) and the bound state peak (Ω). The data is combined from the FOV's shown in figure 1 and figure 4. The fitted line gives a slope of 1.2 with and intercept of -15.2 mV……71

4.11: A) Topograph of the 50 nm x 50 nm FOV of OP83K with nominal 0.05% Fe doping. B) he concurrent LDOS map taken over the same field of view displayed at a bias voltage of 23.3 mV. C) The dashed lines represent the LDOS over the entire FOV excluding the Fe atoms. The solid line represents the LDOS on the Fe atoms averaged over every Fe atom in the FOV. D) The computed $K(\vec{r})$in the FOV, the bright white spots represent Fe impurities. E) A small FOV taken around the red box in figure 4.11 A showing the spatial structure of a typical Fe impurity……74

4.12: Gap map of the FOV shown in figure 7a, where the white circles represent the location of Fe impurities……75

4.13: The average gap a as a function of distance from the Fe impurity site. This was computed by taking a circular mask around each Fe impurity and successively increasing the distance from the impurity site……76

4.14: Gap map of a 24nm x 24nm FOV on an OP91K sample……78

4.15: Comparison of gap distributions between the OP91K sample shown in figure 4.13 with the Fe doped sample shown in figure 4.11. The OP 91K sample is displayed in blue, the Fe doped sample is displayed in red, and the Fe doped sample with the Fe atoms artificially removed is displayed in black……...79

4.16: The gap distribution of the optimally doped Fe doped sample (displayed in black) with the gap set to zero around the Fe impurities with a 1 coherence length radius compared with the gap distribution of a no Fe doped OP91K sample(blue). Both distributions have been scaled by the average gap……..80

4.17: Topographic image and LDOS(r,E) of 4 different Fe impurities. The LDOS are given at energy W and the impurity is indicated in the topograph by a red circle. A-B) Δ=34.4 mV, Ω=20.3 mV C-D) Δ=31.3 mV, Ω=21.8 mV E-F) Δ=29.7 mV, Ω=25 mV, G-H) Δ=37.5 mV, Ω=40.6 mV……...82

4.18: Line cuts taken across high symmetry directions for figures 4.17 d,h,f. The bright red spot indicates the location of the Fe atom……83

4.19: The line cute from figure 15a with arrows indicating the spatial spectroscopic signature of the Fe impurity……...84

4.20: Amplitude of the LDOS taken at the energy of the impurity along the direction of the next nearest neighbor. A) Cut taken from figure 4.18 a. B) Cut taken from figure 4.18 c. C) Cut taken from figure 4.18 e……86

4.21: Amplitude of the LDOS taken at the energy of the impurity along the direction of the nearest neighbor. A) Cut taken from figure 4.18 a. B) Cut taken from figure 4.18 c. C) Cut taken from figure 4.18 e……87

4.22: Peak height extracted from figures 17 a-c plotted against distance from the Fe impurity. A) Peak height from 4.18 a. B) Peak height from 4.18 c. C) Peak height from figure 4.18 e……...89

4.23: Spatially variance of Γ from Eq. 4.5. The black circle indicates the location of te Fe atom. The data shows no significant decrease in quasiparticle lifetime near the Fe impurity……..91

4.24: Zero Bias layer of a 24nm x 24 nm field of view. The green circles indicate the location of Fe impurities and the red circles indicated the location of native Cu vacancies. Zero bias conductance is enhanced but details depend on particular impurity……92

4.25: Averaged LDOS for different Fe impurities. The dashed line indicate the fit to the model from [66] using the offsite LDOS as the nonmagnetic DOS. The red arrows indicate the bound state energy (E_b) extracted from the model and the black arrows indicate the location of the superconducting gap extracted from a Dynes fitting to the electron side of the LDOS. A) Spectra averaged every 10 Fe impurities sorted by the extracted magnetic correlation temperature (T_{MC}) for OP Bi2212 with 0.5% Fe substituted for Cu at T=5.2K, with set up conditions of I_{set}=100 pA and V_{bias}=-100 mV. B) Spectra averaged every 5 Fe impurities sorted by the extracted magnetic correlation temperature (T_{MC}) for UD Bi2212 with 0.5% Fe substituted for Cu at T=5.2K, with set up conditions of I_{set}=100 pA and V_{bias}=-300 mV.....95

4.26: A) Relationship between the bound state energy(E_b) and the extracted magnetic correlation temperature (T_{MC}) extracted from the model in [66] using the offsite LDOS as the non-magnetic DOS. The parameters are extracted from the fits to the spectra shown in figure 4.25 A and 4.25 B for both dopings. The plot shows a linear relationship. B) Relationship between E_b and T_{MC} scaled by the superconducting gap (extracted by a Dynes fitting to the electron side of the LDOS). The data indicates a deviation from self-consistency calculations of non-disordered s-wave superconductors.....96

4.27: Extracted parameters from the theoretical model(the red and blue dots) of [66] from the optimally doped Bi2212 sample compared to the theoretical model of [57]. The experimental data shows a clear deviation from the expected trend.....96

4.28: A) Typical topography in UD Bi2212 Tc=55K with 1.5% Fe conectration, with intila set up conditions of I=30pA and V=-300 mV. B) $LDOS(r, +95mV)$over the FoV in part A, withequvilant set up conditions. The localized dark spots are spectroscopic signatures of Fe impurities.....97

4.29: Local doping extracted from the local superconducting gap using the phenomelogical relationship from [16] vs the magnetic correlation temperature extracted from the fits to the spectra shown in figure4. 25A and 4.25B, where the blue markers are the T_{MC} for the OP sample and the green markers are the T_{MC} for the UD sample. The red markers indicate the magnetic gap temperature as measured by neutron scattering on a YBCO sample across the indicated doping[88]. The measured T_{MC} for BSCCO goes to 0 at a p~0.22 consistent with the theoretically predicted value for the Anti Ferromagnetic Quantum Critical Point[89].....99

CHAPTER 1

INTRODUCTION

Superconductivity, which is characterized as a metal with zero electrical resistance and perfect diamagnetism, was one of the greatest triumphs of quantum physics. It was originally discovered by Heike Kamerlingh Onnes [1] on April 8, 1911 in Leiden. In a somewhat ironic twist of fate Onnes was actually quite annoyed by the observance of superconductivity, he thought it was an experimental error. But in due time he recognized the discovery and was subsequently awarded the 1913 noble prize.

Although superconductivity was observed in 1911 it would take another 46 years before the phenomena would be understood from a microscopic point of view. It was the theory of Bardeen, Cooper and Schrieffer (BCS) [2] that finally provided a complete theory of the phenomena. Even after the theory was understood a new class of materials emerged that exhibited superconductivity but at temperatures much higher than previously observed. These new class of materials were creatively called "high temperature" superconductors and they will be the central topic of this thesis. However, we begin by giving a description of BCS theory.

1.1 Cooper's Problem

As mentioned above superconductivity is characterized by two phenomena, the first is zero electrical resistance, this was discovered by Onnes[1], the second is the

expulsion of all magnetic fields, this was discovered by Meissner and Oshenfeld [3] in 1933. In order to understand the microscopic nature of this phenomena BCS assumed that the underlying phenomena was electron pairing.

To understand some of the consequences of pairing it's useful to consider Coopers problem [4]. Cooper asked the question, does a bound state exist of two electrons of opposite spin coupled together by an attractive potential above a filled Fermi sea. The Fermi Sea is filled simply to satisfy the Pauli exclusion principle and prevent states from below the Fermi surface from participating in the two particle problem. A schematic of this is shown in figure 1.1.

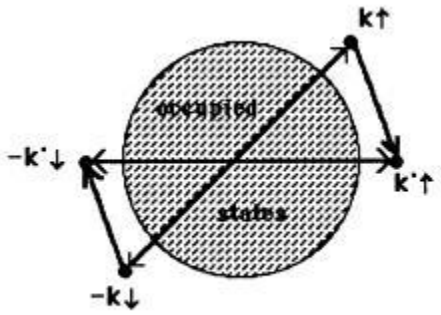

Figure 1.1: A typical excitation in Cooper's problem [17].

If we assume the system is translationally invariant and neglect spin dependent forces, then the center of mass momentum of the pair and the total spin S are constants of motion. If we only consider the zero momentum (**q**=0) state, for simplicity, we may expand the pair wave function as follows,

$$\psi(\vec{r}_1,\vec{r}_2) = \sum_k a_k e^{-i\vec{k}\cdot\vec{r}_1} e^{-i\vec{k}\cdot\vec{r}_2} \qquad (1.1).$$

In order to find whether or not a bound state exists we need to find the eigen values (W) from Schrodinger's equation$(W - H_0)\psi = V\psi$, where $H_0\psi = \epsilon_k$. When Eq. 1.1 is plugged in to Schrodinger's equation we arrive at

$$(W - 2\epsilon_k)a_k = \sum_k V_{kk'}a_{k'} \tag{1.2}$$

where $V_{kk'} = \langle k, -k|V|k', -k'\rangle$. If we assume that the potential $V_{kk'}$ is factorable and isotropic, it can then be expanded into its partial wave components. This leads to the following form of the potential, $V_l(|k||k'|) = \lambda_l \omega_k^l \omega_{k'}^{l*}$. Which, with a little algebra, this expansion for the potential leads to the following formula for the eigen energies,

$$1 = \lambda_l \sum_k \left|\omega_k^l\right| \frac{1}{W_{lm} - 2\epsilon_k} \tag{1.3}.$$

If we take the following simple case for the potential,

$$\omega_k^l = \begin{cases} 1 & 0 < \epsilon_k < \omega_c \\ 0 & \text{otherwise} \end{cases} \tag{1.4}$$

where $\lambda_l < 0$ to make the potential attractive and ω_c is a cut off energy, then with a little bit of effort and assuming $N(0)|\lambda_l| \ll 1$,which is the weak coupling limit, where N(0) is the density of states of the normal metal, we arrive at the following expression for the eigen energies,

$$|W_{lm}| \cong 2\omega_c \exp\left[-\frac{2}{N(0)|\lambda_l|}\right] \tag{1.5}.$$

From Eq. 1.5 we see that the binding energy is an extremely sensitive function of the coupling strength for the weak coupling approximation. However, a bound state exists for an arbitrarily weak coupling so long as the potential is attractive near the

Fermi surface [4]. Copper suggested that electrons entering this type of bound state were associated with the superconducting state.

The careful reader will immediately raise an objection to this bound state. The bound state has a very small binding energy ~10^{-4} eV, hence won't strong correlations between electrons in the normal state lead to fluctuations that will break the pair? This can be resolved by recalling that Landau's Fermi liquid theory[5] gives an appropriate account of the low lying states in the normal state. The cornerstone of this theory is to treat the effects of electron-electron interactions as a single electron like particle with a renormalized mass. This particle is referred to as a quasi-particle. These quasi-particles, and not bare electrons, are what form stable excitations in a metal in the vicinity of the Fermi surface. According to Fermi liquid theory there can be residual interactions between quasi particles that are not taken into account in the mass renormalization, it's these interactions which lead to superconductivity.

1.2 BCS Theory

With an understanding that any full theory will involve quasi-particles, it is possible to write down a Hamiltonian that describes superconductivity, this was done by [2] and is given below

$$H = \sum_{ks} \epsilon_k n_{ks} + \sum_{kk'} V_{kk'} b_{k'}^{+} b_k \tag{1.6}$$

where $n_{ks}$is the number operator and $b_{k'}^{+}(b_k)$ are pair creation (annihilation) operators. The ground state wave function is given below,

$$|\psi_g\rangle = \prod_k (u_k + v_k c_{k\uparrow}^{+} c_{-k\downarrow}^{+})|0\rangle \tag{1.7}.$$

Where $|u_k|^2 + |v_k|^2 = 1$ is the normalization and $|0\rangle$ is vacuum. The coefficients of the ground state are found by using a variational method to minimize the expectation value of Eq. 1.6, this was done successfully by [2]. Immediately several features begin to emerge, the most prominent one is the appearance of an energy gap. This energy gap represents an energy range were no quasiparticle states can exist. The nature of the BCS wave function causes particles and holes to be mixed [6]. Therefore a superconducting density of states will have particle-hole symmetry.

Up to this point we have not made any mention of the physical cause of the attractive interaction between the quasi particles. Physically how this happens is as follows; and electron with negative charge attracts positive ions as it moves inside the solid, this causes a distortion behind it which creates a brief positive charge. This positive charge attracts another electron creating the cooper pair, which is formed as long as this positive charge is greater than the electron-electron coulomb interactions. A graphical depiction of this process is given in figure 1.2. It's important to note that the theory just simply states that an attractive potential needs to be present, it does not mandate that it manifest itself in this fashion.

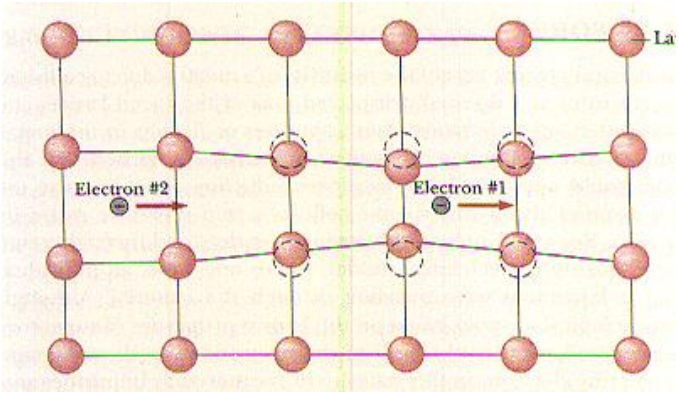

Figure 1.2: A graphical depiction of how phonon mediated superconductivity manifest itself physically.

BCS theory also correctly predicts the second physical characteristic of superconductivity which is perfect diamagnetism. There are two types of classification for superconductors (type I and type II) depending on how perfect their diamagnetism manifests itself. Type I superconductors where discovered by [3] and show perfect diamagnetism below the superconducting transition temperature (T_c) and below some critical field (H_c). Inside the bulk of a type I superconductor the field is zero, however at the surface the field decays rapidly over a characteristic length scale called the penetration depth. In type II superconductors the superconductivity does not break down discontinuously at some critical field (H_{c1}), but rather flux begins to penetrate the solid in discrete pockets until superconductivity is destroyed completely at some upper critical field H_{c2}.

1.3 Green's Function

A more useful approach to BCS theory is to deploy the greens function method. This was developed by Gor'kov following the work of Nambu. The basic idea is to introduce a four vector spinor representation of particle and hole states, $\Psi^+ = (\psi_\uparrow^+, \psi_\downarrow^+, \psi_{\uparrow,}\psi_\downarrow)$. The matrix green's function that follows is defined as the following time order product, $G(x,x') = \langle T_\tau \Psi(x)\Psi^+(x')\rangle$. For a singlet homogenous superconductor the Hamiltonian takes on the following form in the Nambu space,

$$H = \int \Psi^+(\vec{r})\,[\xi(-i\nabla)\tau_3 + \Delta\tau_1\sigma_2]\Psi(\vec{r}) \qquad (1.8).$$

In the equation above ξ represents the Bloch bands typically determined by either an LDA or tight binding calculation, Δ is the gap order parameter which typically

determines the nature of the pairing,τ_i are the pauli matrices in particle hole space, and $\tau_i\sigma_j$ denotes a direct product of matrices operating in the four dimensional Nambu space. The green's function for the Hamiltonian in Eq. 1.8 was computed by [7], and is given below,

$$G_0{}^{-1}(\vec{k},\omega) = i\omega_n - \xi(\vec{k})\tau_3 - \Delta(\vec{k})\sigma_2\tau_1 \qquad (1.9).$$

Here $\omega_n = \pi T(2n+1)$ is the Matsubara frequency. This formalism will be particularly useful when computing the density of states (DOS) of superconductors, because the $LDOS(\vec{r},\omega) = -\frac{\pi}{2}Im[G(\vec{r},\omega)]$. The DOS will be one of the most important quantities in this thesis.

1.4 Conventional Superconductors

Typically conventional superconductors are type I superconductors. Another feature of conventional superconductors is their simple s-wave gap order parameter. An s-wave superconducting gap is isotropic and spherical in k-space as shown in figure 1.3. The real space gap in conventional super conductors is also spatially homogenous. Furthermore, the gap size is related to the critical temperature as follows, $\Delta = 3.5k_BT_c$, which is a consequence of a weak coupling BCS theory. The green function in Eq. 1.9 can be computed by setting $\Delta(\vec{k}) = \Delta_0$. The typical transition temperatures for conventional superconductors are of order ~4K, and they are usually observed in pure metals such as lead, niobium, and aluminum. The resistivity of mercury is given in figure 1.4 as an example.

Obviously there would be great technological benefits if the superconducting state could be attained at temperatures greater than that of liquid helium, and for

much of the 20th century this goal was the focus of a tremendous amount of research. But, until 1986 many physicist believed that the highest superconducting temperature allowed by BCS was 30 K.

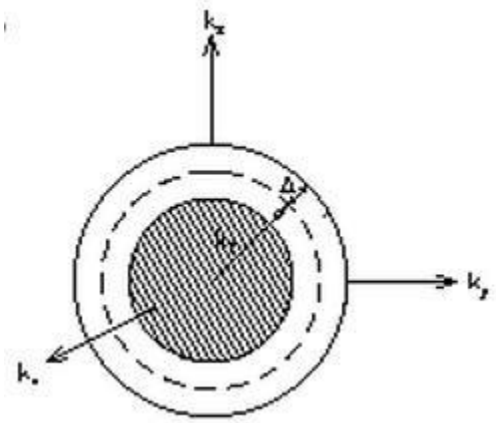

Figure 1.3: A graphical depiction of a BCS s-wave order parameter in k-space.

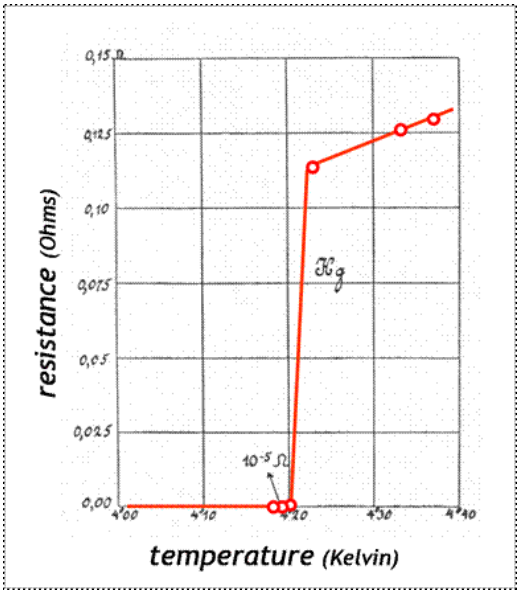

Figure 1.4: Resistivity of Mercury as a function of temperature, the transition from normal to superconductor happens at 4.2K [1].

1.5 High Temperature Superconductors

Prior to 1986 the highest T_c's belonged to Nb_3Sn (18K) and Nb_3Ge (23K), however in 1986 Bednorz and Muller discovered superconductivity in a lanthanum based cuprate perovskite with a T_c of 35K [8]. It was soon found that replacing La with Y increased the T_c to 92K. A graph of T_c throughout the last century is given in figure 1.5. This discovery, for which Bednorz and Muller were given the 1987 Nobel Prize, had tantalizing technological applications. Yet these new superconductors were not simple alloys as their predecessors were. Furthermore, some unusual behavior began to arise almost immediately.

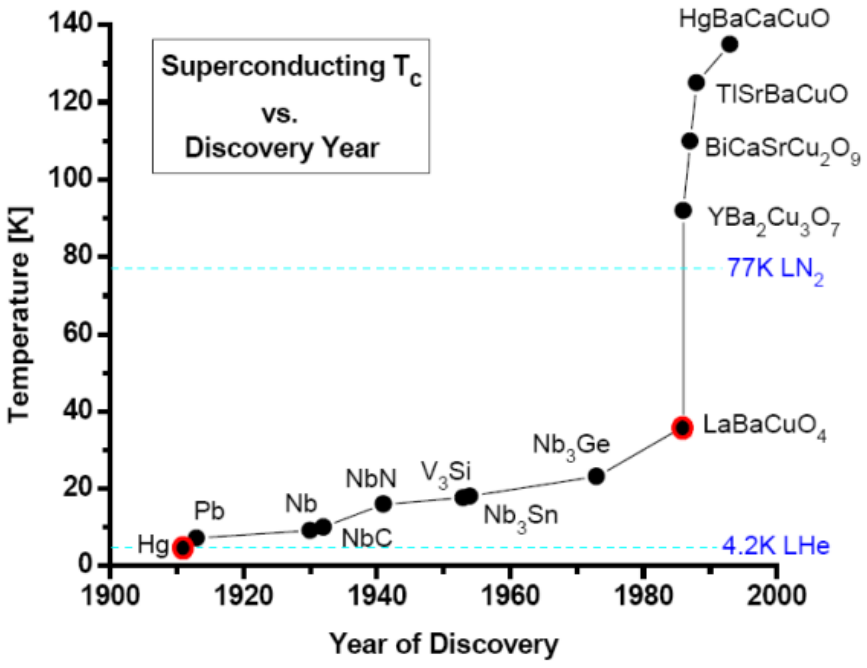

Figure 1.5: Highest superconducting transition temperatures from 1911 to 2000, red indicates materials for which noble prizes were awarded.

They were the first oxide superconductors to be observed, their parent compound (meaning zero hole doping) were anti ferro magnetic Mott insulators. This seemed odd because one would not expect magnetism and superconductivity to be able to coexist. The new class of superconductors also showed a phase rich

diagram which was in contrast to conventional superconductors. The cuprates are also class II superconductors but with an unusually high H_{C2} ~60T [9]. Gap size was also measured to be quite large in the cuprates (~40 meV at optimal doping) which was in contrast to conventional superconductors (~5 meV). Furthermore, their gap size did not follow the weak coupling BCS behavior described in section 1.4, but rather followed the following trend $\Delta = 7.9 k_B T_c$ for optimal and overdoped samples [10], this was indicative of strong coupling behavior. All these strange behaviors led to a flurry of work, which is ongoing in these materials.

The first challenge of the new class of superconductors was to understand their underlying structure. This was accomplished by various x-ray experiments[67,68,69,70,71], which showed that the cuprates have a multilayer orthorhombic unit cell. The typical unit cell for the three most common cuprates is shown in figure 1.6.

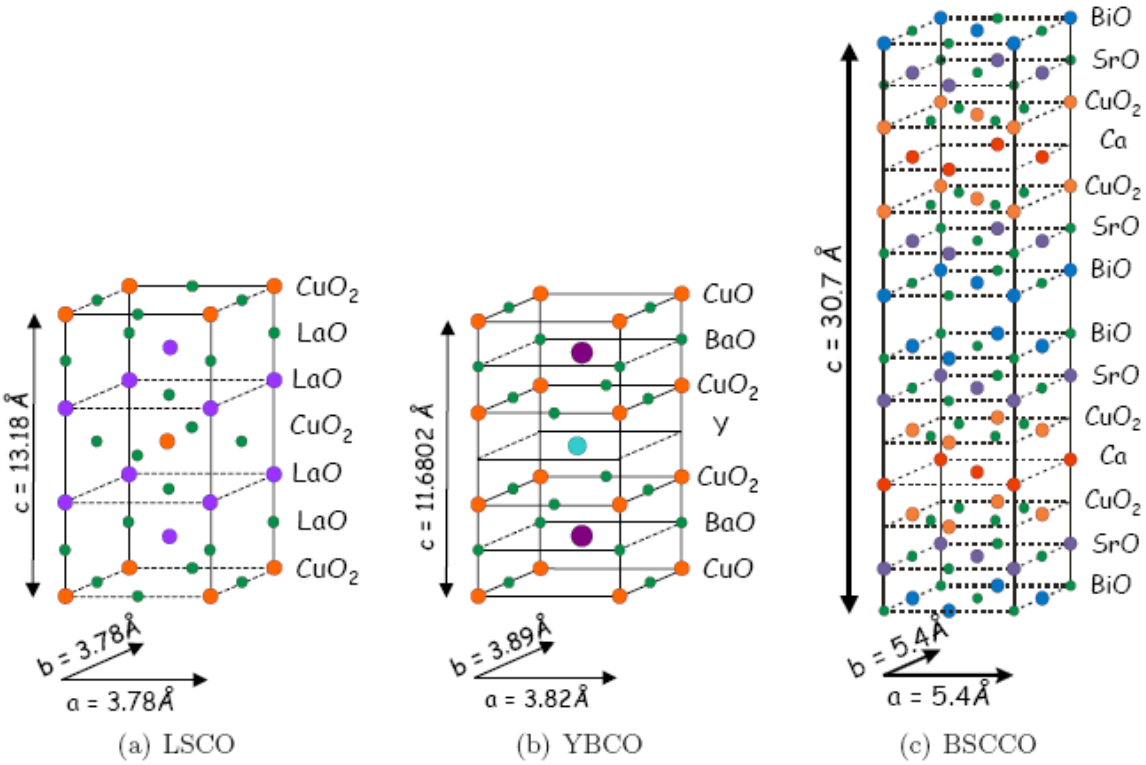

Figure 1.6: Unit cells for (a) $La_{2-x}Sr_xCuO_4$ (b) $YBa_2Cu_3O_{7-\delta}$ (c) $Bi_2Sr_2CaCu_2O_{8+\delta}$

Stoichiometric data also showed large amounts of disorder in LSCO and BSCCO [11]. These types of disorder include Bi-Sr substitution in Bi2212, Y-Ca substitution in Bi2212. There is also disorder away from the CuO_2 plane such as excessive oxygen and oxygen vacancies in Bi2212. All of these disorders seem to have an effect on T_c, making the cuprate problem that much more difficult. A summary of the disorder from [11], is given in figure 1.7.

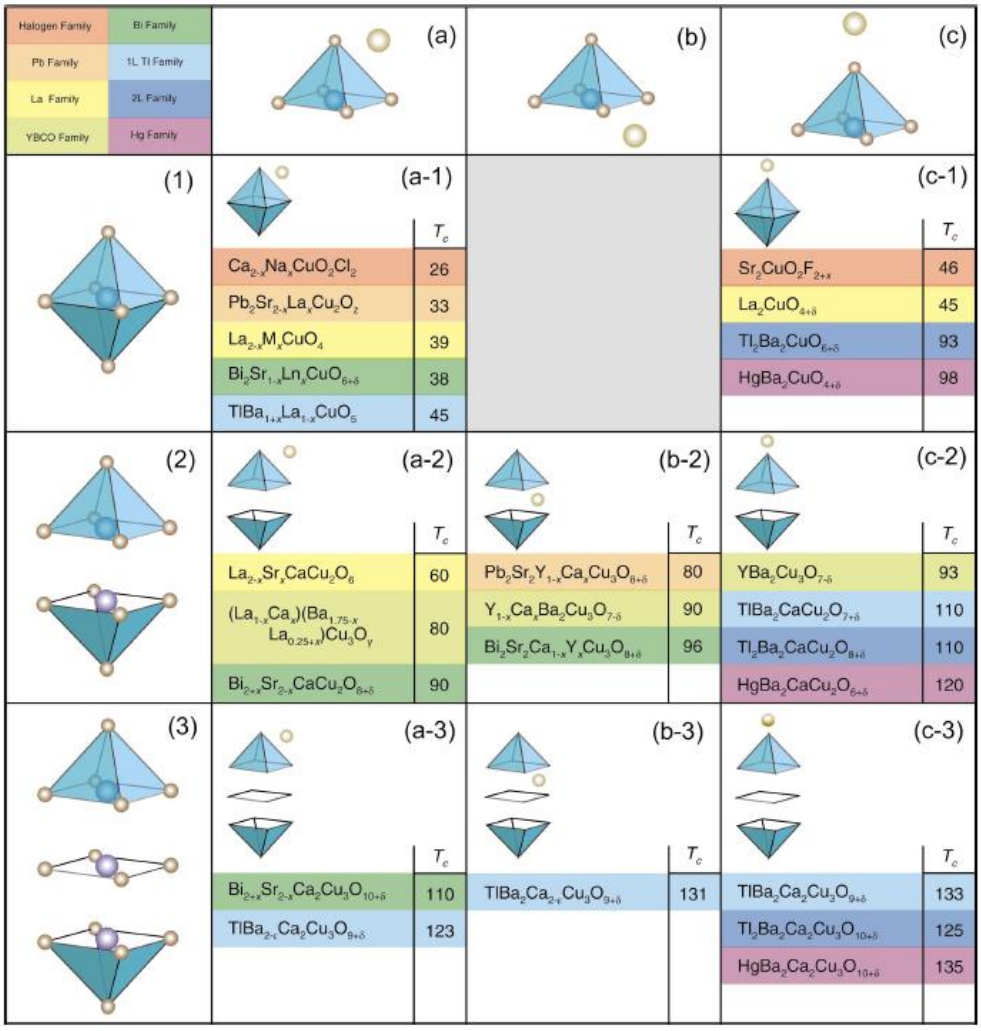

Figure 1.7: Summery of the different types of disorder in the cuprate family from [11]

The cuprates also exhibit an unusual gap order parameter. Instead of the typical s-wave order parameter they possess a d-wave order parameter. This means that electrons traveling in different directions in the crystal feel a different pairing potential. The existence of this new gap order parameter was first discovered by flux modulation experiments in a YBCO dc-squid [12] and then confirmed by flux magnetization in trivalent YBCO [13]. The cuprates were the first physical system to possess a d-wave gap order parameter.

As mentioned above the cuprates also have a rich phase diagram, a toy model of the phases that exist in the cuprates is given in figure 1.8. It's important to note that this is not an actual generic phase diagram of the cuprates, because the behavior of each family varies widely. But, there are 3 phase that are present in all family of cuprate superconductors they are, 1) the anti-ferromagnetic mott insulator parent compound 2) the d-wave superconducting dome, and 3) the existence of a non-superconducting energy gap phase, termed the pseudo gap.

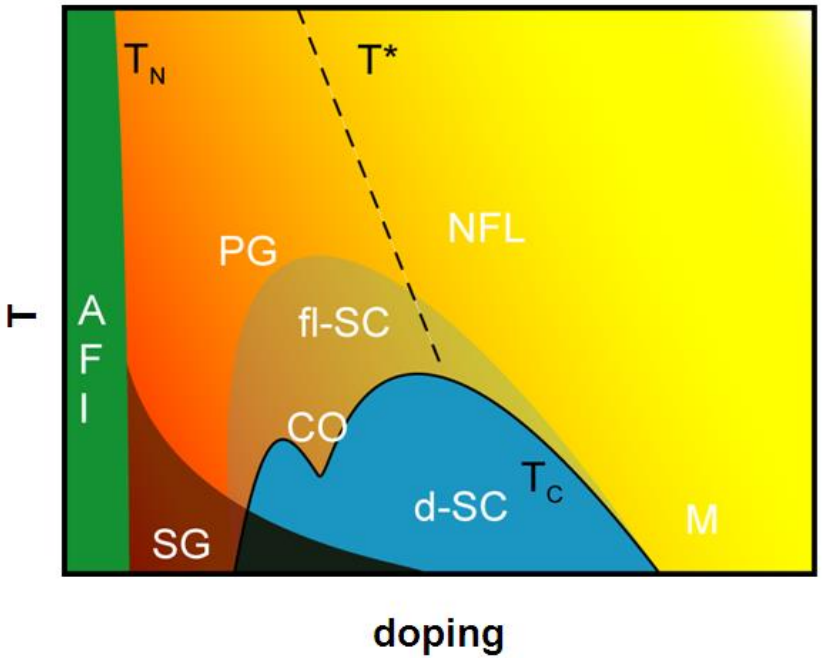

Figure 1.8: A toy model of the cuprate phase diagram. Where AFI stands for anti-ferromagnetic insulator, PG stands for pseudogap, d-SC stands for d wave superconductor, NFL stands for non-Fermi liquid, M stands for metal, all of these phases are found in all cuprates but at slightly different doping. Evidence exist for the following three phases in Bi2212, SG which stands for spin glass, CO which stands for charge ordering, and fl-SC which stands for fluctuating superconductor. Note this is not a generic model of the cuprate phase diagram.

In general one would not associate insulators with superconductors, in particular Mott insulators. A Mott insulator is an insulator in which the onsite coulomb repulsion localizes the electrons on a lattice site. In the cuprates this

manifests itself by the Cu atoms being in the +2 valance state and being singly occupied due to large coulomb repulsion, ~6-8 eV. The spin of the nearest neighbor is also singly occupied by an electron of opposite spin, hence the anti-ferromagnetism. As of this writing the problem of doping into a Mott insulator remains unsolved and it is intriguing that it makes an appearance in high temperature superconductivity.

The dome like structure of superconductivity in these materials also raises many interesting possibilities. It is clear from the phase diagram in figure 1.8 that the T_c is a function of carrier concentration, which is done by increasing the number of holes in the material. But the question arises, why the dome? Many theories as to why this happens are tied to the pseudo gap [72, 73, 74, 75, 76]. As of this writing the origin of the pseudo gap remains unknown. Theories on the pseudo gap range from a competing phase of matter, non-coherent superconductivity, and quantum phase transitions.

1.6 Probing the High T_c cuprates

In order to study the cuprate superconductors many probes are employed such as Scanning Tunneling Microscopy (STM), Angle Resolved Photoemission (ARPES), Inelastic Neutron Scattering (INS), Raman spectroscopy, break junction experiments, just to name a few. A summary of the energy scales measured in Bi2212 by these different probes is given in figure 1.9.

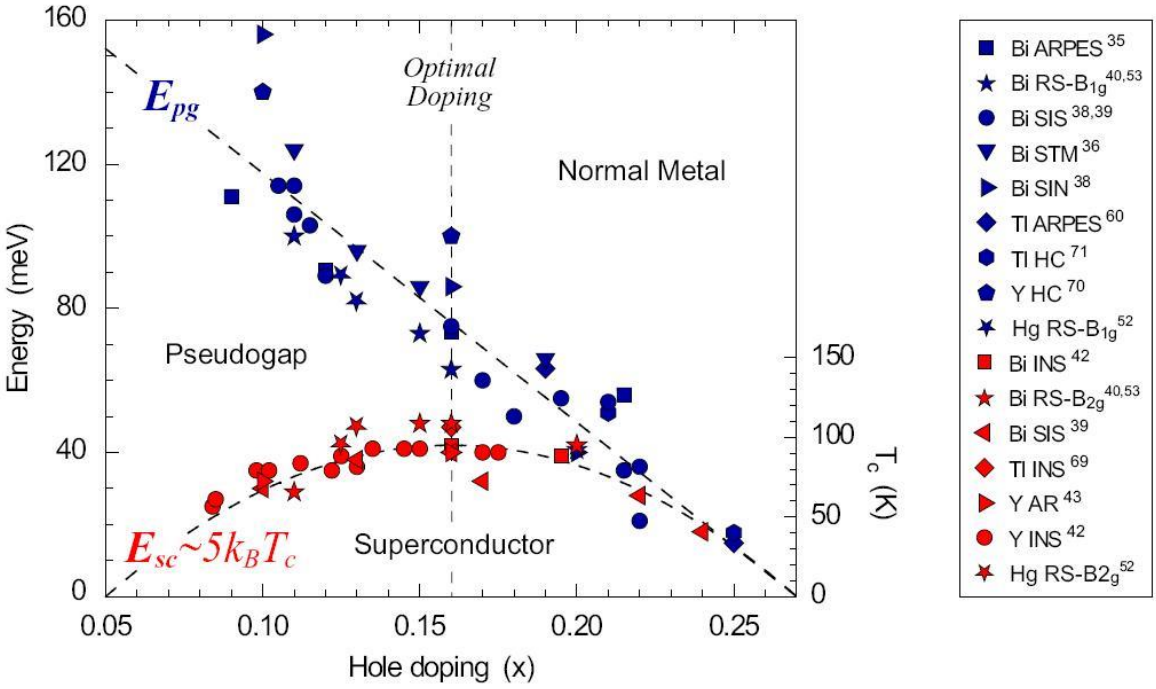

Figure 1.9: The different energy scales measured by different probes in Bi2212 as reported in [14].

It's clear that there are two distinct energy scales in this material, the superconducting energy scale and the pseudo gap energy scale. Yet from this report [14] it would appear that no probe is sensitive to both energy scales simultaneously. Many studies have been [15,16] conducted in order to identify both energy scales simultaneously. In particular STM studies on Bi2212 seem to show fantastic progress in this regard. However, making STM agree with other probes quantatively is something that has yet to be addressed by the community. In particular STM also allows for the probing of the real space states while also simultaneously probing the q-space states through a technique called quasiparticle interference (QPI), which will be explained in chapter 3.

Agreement between QPI data and data from k-space probes will be one of the topics discussed in this thesis.

Of the probing on the cuprates a tremendous amount seems to be done on the underdoped side. In fact there is evidence for various phase of matter from STM data such as a spin glass state [21], nematic ordering [18], charge density wave [19], and a fluctuating stripe ordering [20]. A lot of these phases seem to suggest that there is a phase competition that occurs on the underdoped side of the cuprates which causes the closing of the dome on that side of the phase diagram.

Another way to probe the cuprates is to introduce impurities to replace Cu in the CuO plane. The CuO plane is the one thing that all cuprates have in common and is believed to be where super conductivity presents itself. The insertion of magnetic impurities might help determine if the superconductivity in the cuprates is mediated by magnetic interactions instead of phonon interactions. Previous work of this nature [22, 23] seemed to suggest that insertion of a pure magnetic scatterer is not possible since Ni and Zn behave as strong charge scatterers. However, in chapter 4 we report the realization of a magnetic scatterer in Bi2212.

These new ways to probe cuprate superconductivity will be the subject of this thesis. Chapter 3 will reconcile the QPI STM data with direct k-space probes. Chapter 4 will present the observation of magnetic scatterers in a cuprate superconductor.

CHAPTER 2

SCANNING TUNNELING MICROSCOPY

The idea behind scanning tunneling microscopy (STM) comes from the simple energy barrier problem typically discussed in an introductory quantum mechanics class. However, understanding how the tunneling process works in metals can be quite subtle. This chapter attempts to elucidate some of these subtleties as well as describe how our home built STM was designed and constructed.

2.1 Introduction

In the simplest picture an STM is basically taking a sharp metallic tip and bringing it near (~5Å) a metallic surface. This essentially recreates the energy barrier problem of introductory quantum mechanics where the vacuum acts as the barrier potential. While the idea behind such an instrument was understood in the early days of quantum theory it would not be realized until 1981 when Gerad Binning and Heinrich Rohrer [24] developed the procedure to create this particular kind of microscope and were subsequently awarded the Nobel prize in 1986. Since its invention techniques for STM have been created to operate the STM not only in ultra-high vacuum environments but also ambient pressure and with a temperature range that's spans millikelvin all the way up to hundreds of degree Celsius. STM proves to be a very useful probe when one wants to probe materials on sub-atomic length scale and find information about the local electronic structure. As such the STM is uniquely suited to study material where there is a variation on the atomic scale, such as $Bi_2Sr_2Ca_2CuO_{8+\delta}$.

2.2 Tunneling Current

The only quantity which the STM measures is a tunneling current, which arises from the application of a bias voltage to the sample which in turn shifts its Fermi energy relative to the tip. This opens up states for electrons to tunnel from the tip to the sample or from the sample to the tip depending on the sign of the bias voltage; the situation is shown schematically in figure 2.1.

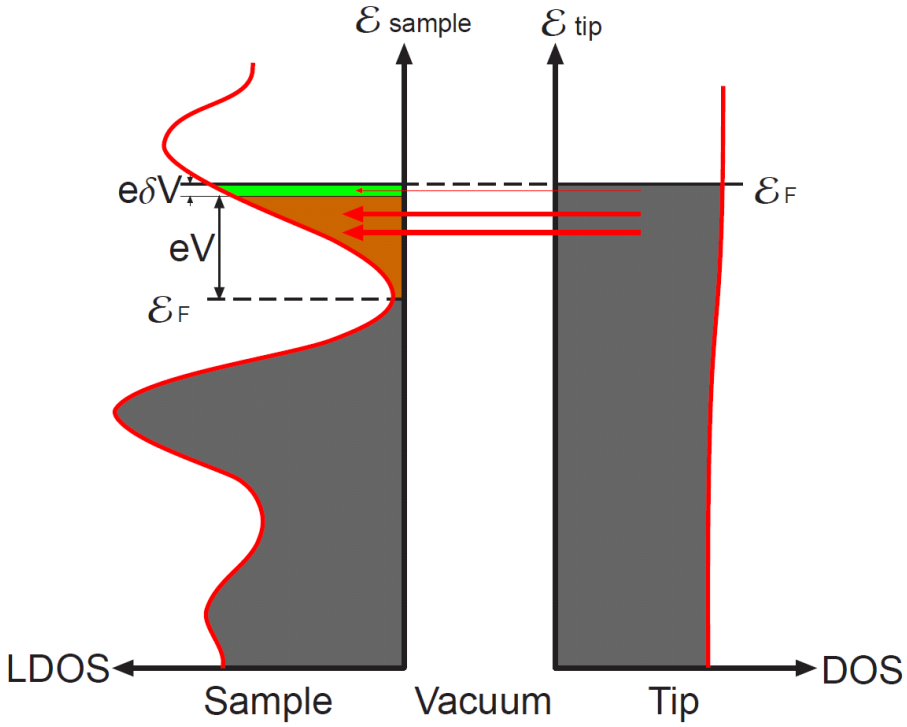

Figure 2.1: Schematic showing the local density of state (LDOS) at a particular location on the sample, which appears on the left hand side, the LDOS of the tip, which appears on the right hand side. The middle region is a vacuum region which acts as a potential barrier between tip and sample, ε_F is the Fermi energy of either tip or sample. When a bias voltage eV is applied to the sample the Fermi energy of the sample shifts relative to the Fermi energy of the tip, allowing the electrons to tunnel into a particular energy window of the LDOS of the sample, which is the Fermi energy of the sample minus the applied bias voltage, this energy window is labeled $e\delta V$.

The elastic tunneling current can be easily written down by using second order perturbation theory and it is as follows:

$$I = -\frac{4\pi e}{\hbar}\int_{-\varepsilon_F}^{\infty} |M|^2 \rho_S(\varepsilon)\rho_t(\varepsilon + eV)\{f(\varepsilon)[1-f(\varepsilon+eV)]-[1-f(\varepsilon)]f(\varepsilon+eV)\}d\varepsilon \qquad (2.1).$$

Where M is the matrix element, ρ is the density of states of either sample or tip, and f represents the Fermi function:

$$f(\varepsilon) = \frac{1}{1+e^{\frac{\varepsilon}{k_B T}}} \tag{2.2}$$

where ε is energy, T is temperature, and k_B is Boltzmann constant. The factor of $\frac{4\pi e}{\hbar}$ comes from $2e * \frac{2\pi}{\hbar}$ where the factor of two comes from spin, and it is important to notice that we are tunneling single electrons and not quasiparitcles or cooper pairs. Because all the work presented in this thesis is done at 5.2 K it is possible to simplify the integral in Eq. 2.1 by approximating the Fermi functions in the $T \to 0$ limit, furthermore one typically selects a metal with a constant density of states to act as the tip, this allows for a further simplification to Eq 2.1, where $\rho_t(\varepsilon)$ is assumed to be constant, $\rho_t(0)$. With all these simplifications taken into account, keeping in mind that the simplifications can be made due to the experimental environment, Eq 2.1 reduces to:

$$I \approx \frac{4\pi e}{\hbar} \rho_t(0) \int_{-eV}^{0} |M|^2 \rho_S(\varepsilon) d\varepsilon \tag{2.3}.$$

The tunneling matrix element was computed by [25] and it is as follows:

$$M_{tip-sample} = -\frac{\hbar^2}{2m_e} \int d\vec{S} * (\psi_{tip} \nabla \psi_{sample} - \psi_{sample} \nabla \psi_{tip}) \tag{2.4}$$

where $\psi_{tip}(\psi_{sample})$ are the unperturbed electronic states of the tip (sample) and $m_e$is the mass of the electron. The integral in Eq. 2.4 has to be evaluated over any surface lying inside the vacuum barrier separating the two metals. Therefore, explicit forms of ψ_{tip} and $\psi_{sample}$are required. This is a difficult proposition because in general the atomic structure of the tip is not known. Hence, a model tip wave

function has to be assumed for the evaluation of Eq. 2.4. The most common used model for the tip wave functions is those developed by [26,27] where the tip is assumed to have simple spherical symmetry. With these assumptions the matrix element can be evaluated assuming a simple s wave form for the tip wave function, where contributions to the tip wave function with angular dependence are neglected. This leads to the following evaluation of Eq.2.4:

$$M_{tip-sample} \approx \exp(\sqrt{\frac{8m_e\phi}{\hbar^2}} * z) \tag{2.5}$$

where z is the distance between the tip and sample and ϕ is the local barrier height. In the model described in [26,27] ϕ is assumed not to depend on lateral position, hence it is possible to interpret ϕ as the surface work function. Essentially the tunneling matrix element is a measure of the amount of overlap between the tip wave function and the sample wave function. Combining the result of Eq 2.5 with Eq 2.3 we arrive at the STM tunneling current:

$$I \approx \frac{4\pi e}{\hbar} e^{-x\sqrt{\frac{8m\varphi}{\hbar^2}}} \rho_t(0) \int_{-eV}^{0} \rho_S(\varepsilon) d\varepsilon \tag{2.6}.$$

Section 2.3 Topography

From Eq. 2.6 it becomes evident that it is possible to image the integrated density of states on a surface, and the spatial resolution of this imaging will be determine by the resolution in the x-y direction. Fortunately, [28] discovered the phenomena of piezoelectricity about 100 years before the first STM was constructed. They observed a voltage after applying pressure to a tin foil with one end grounded. Immediately after the discovery of piezoelectricity, inverse piezoelectricity was observed [29], where the application of a voltage to a quartz crystal caused a

structural deformation. It is this inverse piezoelectric effect that would prove to be crucial for STM.

One can model inverse piezoelectricity by simply realizing that when a voltage V is applied to a material it causes an electric filed (E) inside it. In the inverse piezoelectric effect this causes a distortion of the material (Δx). Therefore we can write down the inverse piezoelectric effect as follows:

$$\Delta x = \overleftrightarrow{D} * \vec{E} \tag{2.7}$$

where D is a tensor due to the fact that the material can be distorted in different directions. Two common materials that show the inverse piezo electric effect are quartz and lead zirconate titanate ceramics (PZT), as we shall see the latter material turns out to be the most useful for 4K STM construction. Many of the materials initially showing inverse piezoelectricity only had a shear and deflection deformations. However, in 1986 [30] invented the tube scanner [30]. This new piezo was a tube of PZT metalized in the outer and inner surfaces and radially poled. It had the advantage of being able to extend vertically (z direction) and by connecting 4 electrode to the sided it could deflect in the x or y direction, therefore giving it a range in the x-y plane, a schematic of a tube scanner from the PI corporation is shown in figure 2.2 a and b.

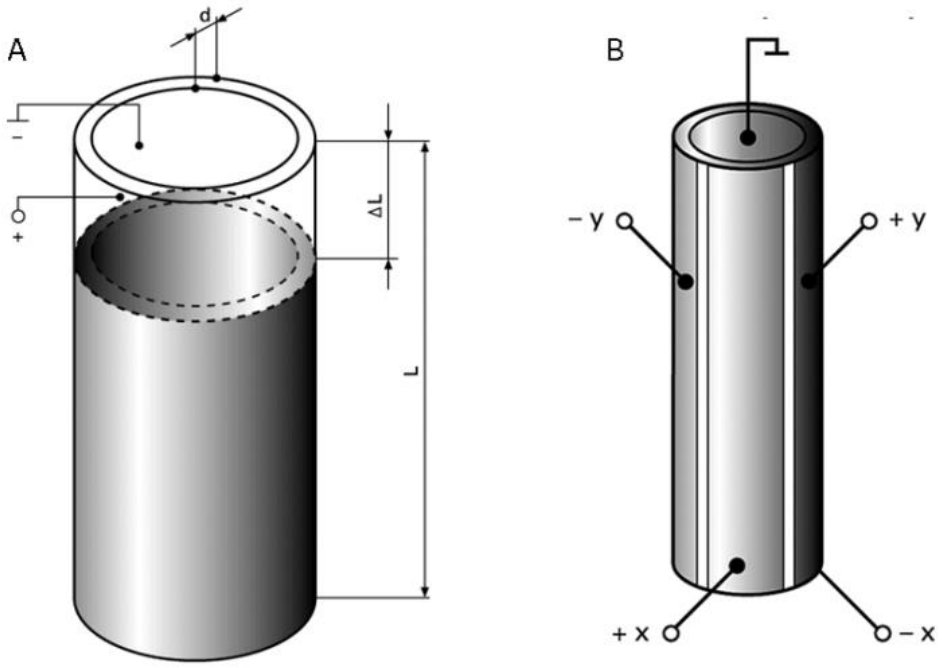

Figure 2.2: A) Scan tube piezo form the PI Corporation showing the z extension. B) Scan tube piezo form the PI Corporation showing the 4 electrodes for x-y deflection.

The displacement of a tube piezo in the z direction can be estimated using the following equation:

$$\Delta x \approx d_{31} * L * \frac{U}{d} \tag{2.8}$$

where d_{31} is the coefficient from the tensor in Eq. 2.7, L is the length of the piezo tube, d is the thickness of the ceramic layer, and U is the applied voltage. Similarly, the x-y deflection is given by the following eqation:

$$\Delta x \approx (2\sqrt{2} * d_{31} * U * L^2)/(\pi * ID * D) \tag{2.9}$$

where ID is the inner diameter of the piezo scanner. It is clear from Eq. 2.8 and 2.9 that d_{31}we will be extremely important in design considerations.

Typical values of $d_{31} \sim -95\, pm/V$ for PZT 8 [31], it is important to note that this value is decreased by approximately a factor of 4 at a temperature of 4K, therefore from Eq. 2.9 and 2.8 we see that at room temperature a PZT 8 scanner with an ID=24.5 mm, L=12 mm, and D=2.159 mm has 2.3 Å$/V$ resolution in the x-y direction and 5.3 Å$/V$ in the z direction. This makes it possible for an STM to image the integrated density of states atom by atom, assuming that the tip is limited to one atom at the end of it, and that you can approach the surface to within 5 Å (this will be explained in section 2.3).

Experimentally this imaging achieved by applying a bias voltage to the sample and using a feedback mechanism that changes the z voltage in order to maintain a pre-set tunneling current value (I_{set}). Therefore, by recording the z voltage we can map the height of the surface. We typically select I_{set} and V_{bias} depending on the density of states of the material. That is, form Eq. 2.6 we see that we are measuring an integrated density of states when we are taking topography, so in principle we would like to take the bias voltage as high as possible. In practice this is very sample dependent, for example in Bi2212 it is not wise to use high bias voltages because the sample is a brittle ceramic and at too high a bias voltage the sample actually rips a part from the surface. Furthermore, at high bias voltages the tunneling barrier becomes asymmetric and it is not possible to interpret the results from Eq. 2.6. A typical topograph on $NbSe_2$,at T=5.2K, a material which shows a strong charge modulation thought to be caused by the formation of a charge density wave is show in in figure 2.3.

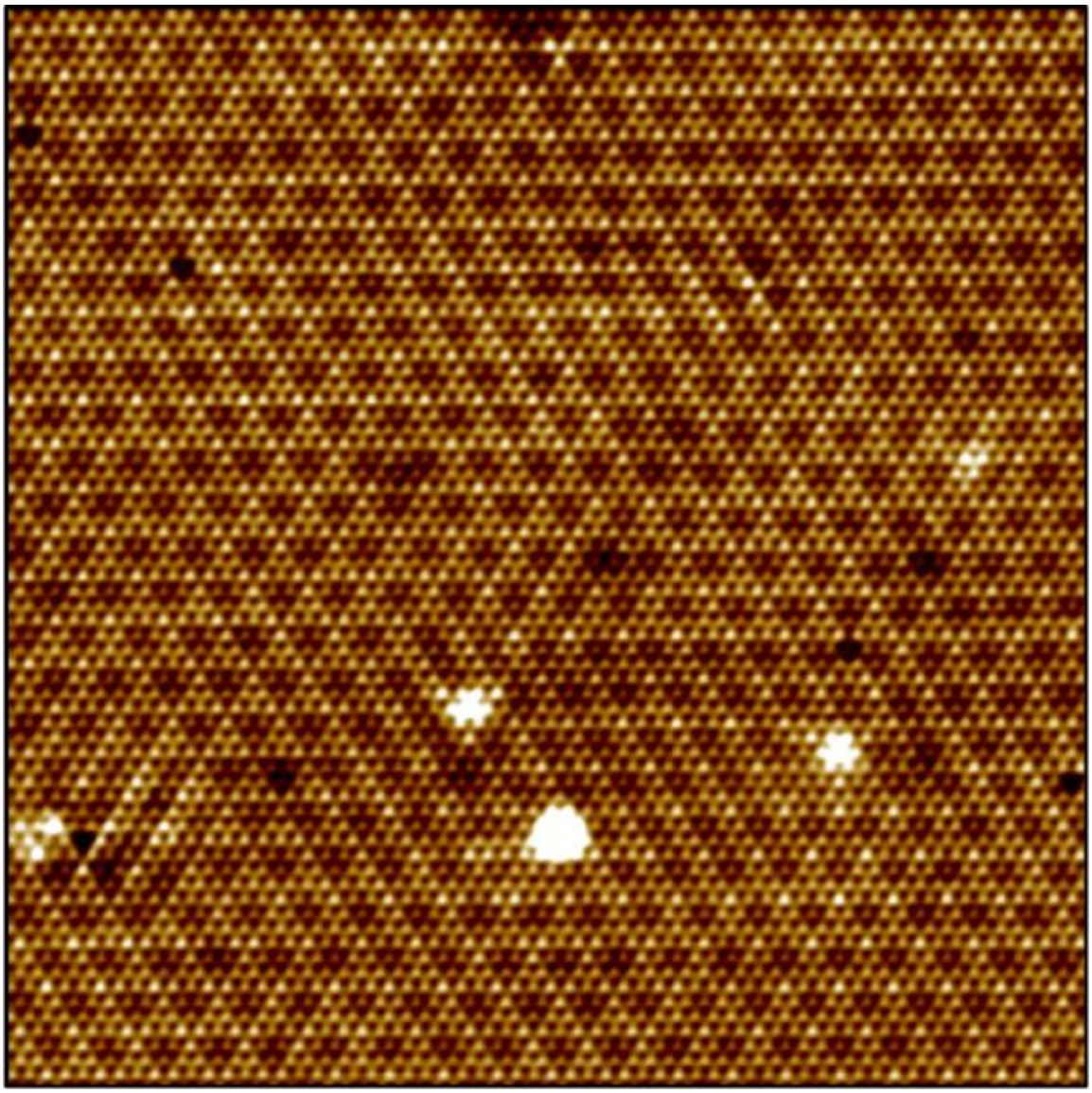

Figure 2.3: STM topography on $NbSe_2$ at T=5.2K, with set up condition I_{set}=100 pA and V_{bias}=-100 mV.

At this point one might ask how we can prepare a tip to be single atom. In our experiment we typically use home etched tungsten tips. The tips are placed into the STM at room temperature and out of vacuum. Therefore a thin oxide layer typically develops at the edge of the tip. In order to clean the tip it is necessary to apply a high electric field which causes high energy electrons to bombard the tip

eventually melting off the oxide layer and leaving behind a clean surface. Typically we repeat this process until we are convinced that the tip is only a few atoms large. As mentioned in the previous paragraph this would destroy a BI2212 sample, therefore the so called field emission is done on an amorphous gold surface.

The careful reader might have noticed that Eq. 2.6 suggest that we could measure the surface work function from the tunneling current if we could vary the vertical position of the tip relative to the surface. The use of a scan tube piezo allows us to do just that. Furthermore, the check of the work functions gives us a necessary tool for checking the health of our junction. Typical work functions on gold are roughly 4-5 eV. Experimentally this is measured by turning off the feedback loop and decreasing the z voltage of the scan tube which causes the scan tube to retract. We then measure the z voltage and convert it into a position using Eq. 2.8 and can then fit the resulting data with $y = A * e^{-\frac{x}{x_0}} + c$ which has the same form as Eq. 2.6 and hence we interpret x_0 as $\sqrt{\frac{8m_e\phi}{\hbar^2}}$ allowing for the extraction of the surface work function ϕ. A typical graph obtained by this method is shown in figure 2.4 where we measure the work function to be 4.5 eV indicating a good junction.

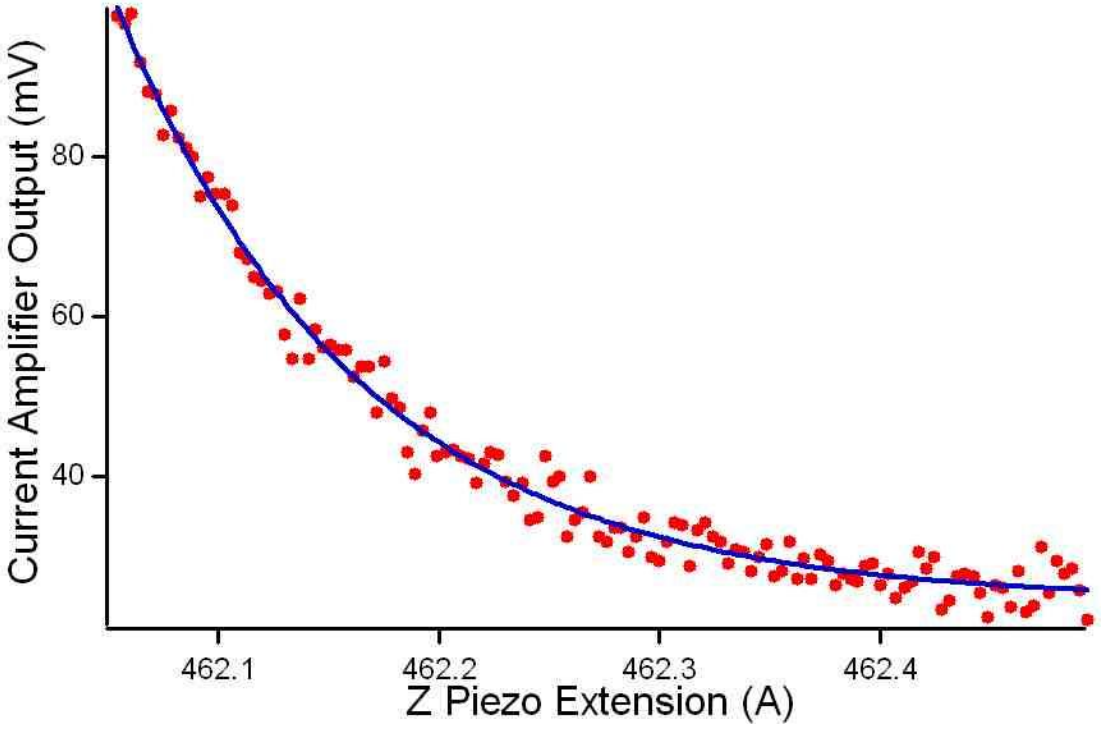

Figure 2.4: The red dots indicate the current as a function of z piezo distance. The blue line displays the fit to the data with the functional form $y = A * e^{-\frac{x}{x_0}} + c$. Where for this data $x_0 = 0.53$ Å which implies $\phi = 4.1\ eV$.

2.4 Walking and STM body

With the invention of the scan piezo it was possible to raster a tip across a surface to measure the integrated density of states with atomic resolution. However, this does not solve the issue of how one gets the tip close enough to the surface (~5Å) to generate a tunneling current in the first place. Traditionally there have been several methods used for this such as the beetle, kangaroo, louse, inchworm, match, etc. But as we shall see in section **2.6** we will be extremely interested in measuring the tunneling current with our feedback loop turned off, hence requiring maximum stability in order to avoid crashing into the surface. Over the past 20 years an approaching method developed by [32], which utilizes 6 shear

mode peizo stack actuators to force course movement of the STM tip, has proven to be the most stable for out of feedback work. In order make the tip coarse approach it is necessary to machine a piece to hold the scan tube piezo, then at the top of the scan tube piezo a piece to hold the tip is also machined and glued on top using torr seal. In our home build 5.2K STM this is accomplished by having a thin caliper tube acting as the tip holder, where the ground of the tip is kept isolated from the scan tube to avoid electrical cross talk in the tunneling current. The scan tube holder is then placed into a sapphire piece that has been machined to have 3 flat sides, the diameter of the scan tube holder is purposely machined bigger than the hole of the sapphire piece in order to make the fit as snug as possible. The piezo stacks are then assembled in the lab as shown in figure 2.5 with AlO plates glued, using torr seal, at the top of each stack. The STM body and scan tube holder are machined using macor since the differential thermal contraction of macor closely matches that of the other material used in the STM.

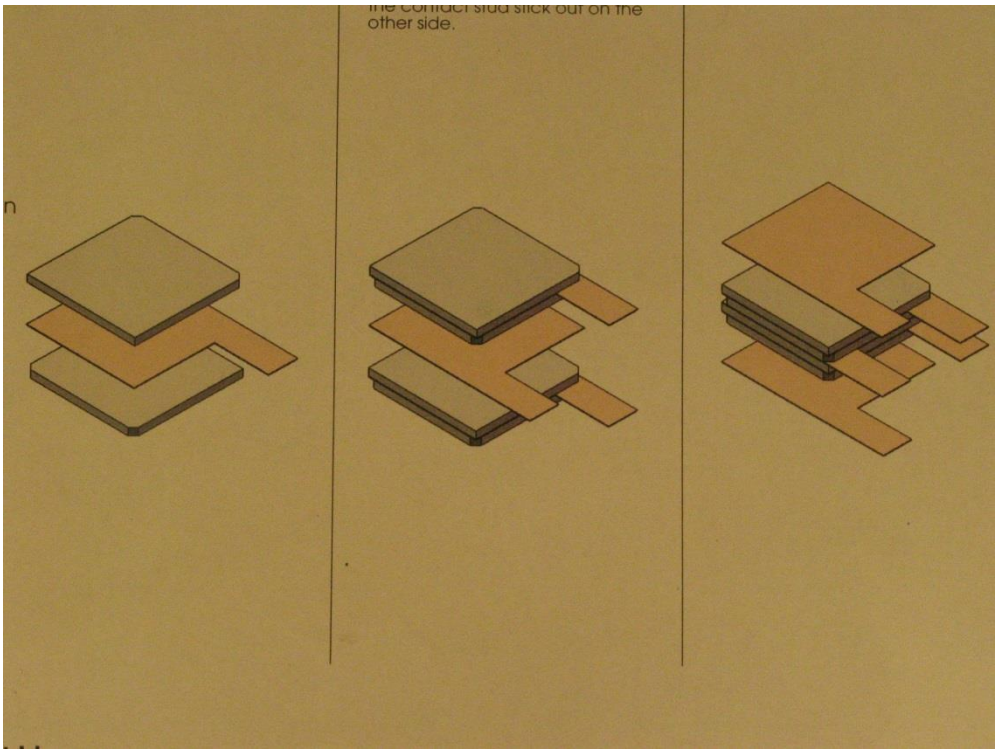

Figure 2.5: Schematic showing the assembly of our homebuilt piezo stacks. The grey pads represent individual piezos and the copper colored pads represent thin copper foil used as electrodes between individual piezos.

The coarse walking process happens by applying a voltage to one of the 6 shear piezos and then applying the same voltage to the next shear piezo after some time delay, and the process continues until all 6 shear piezos have now sheared in the opposite direction of the desired motion by having the same voltage applied to all 6 of them with a time delay between voltage applications. The voltage is then released on all 6 piezos simultaneously resulting in the sapphire beam being pushed up some course amount, typically ~40 nm/step at 5.2K. A schematic of the coarse walking is shown in figure 2.6. A schematic of our home built STM is shown in figure 2.7 A and a top view showing the piezo stacks is shown in figure 2.7 B.

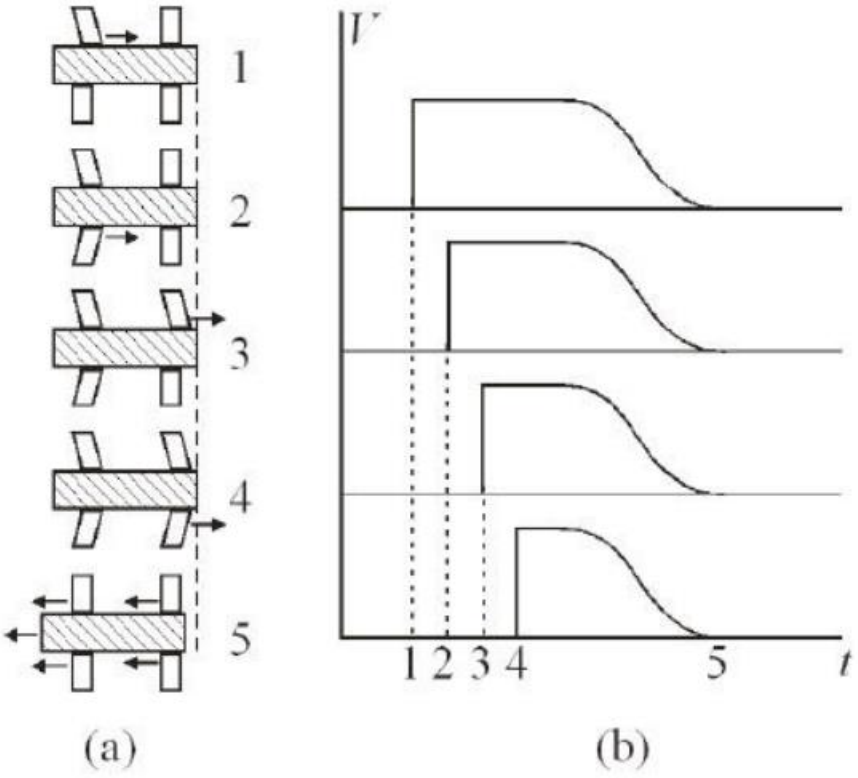

Figure 2.6: A) An illustration of the coarse approach mechanism using the shear piezo actuators, where each leg is shown firing at different times time. B) The voltage profiles applied to each piezo actuator. [32]

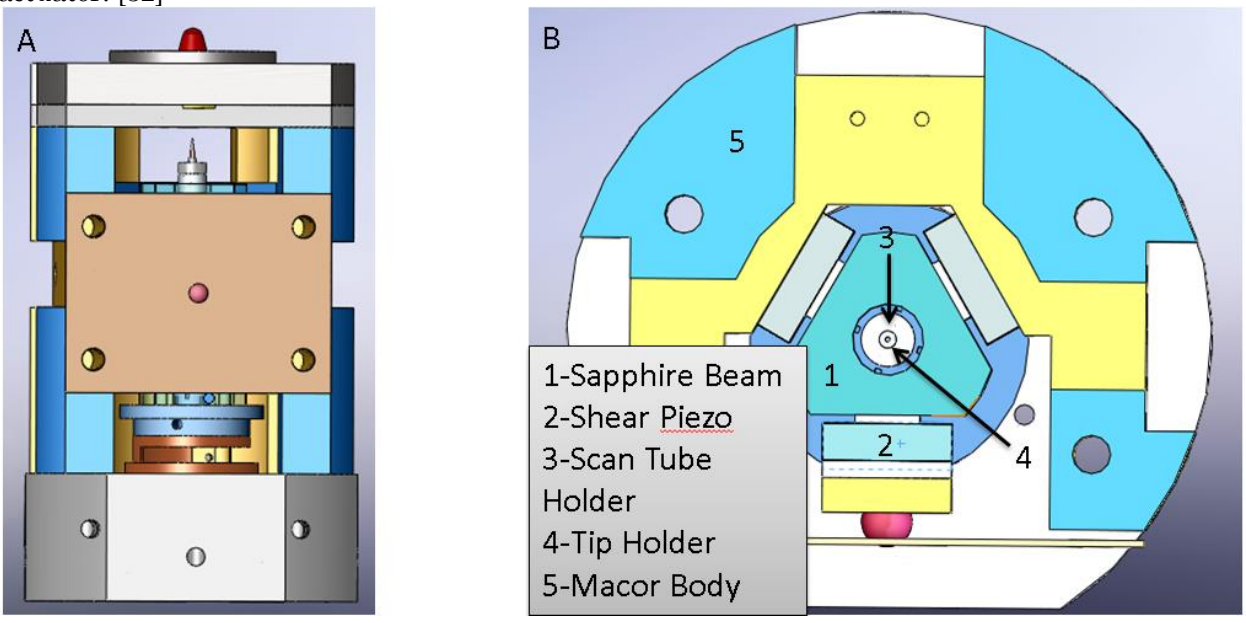

Figure 2.7: A) STM body viewed from the front. B) STM viewed from the top with the titanium cover removed to show the tip holder, scan tube holder, shear piezos, and tip holder as indicated in the figure.

This type of coarse walking also has some other benefits besides its vibrational stability. It allows for a compact STM design, the height of our STM is 61 mm with a diameter of 38 mm, this is crucial for doing low temperature work as most 4K dip probes do not have a lot of space. This type of walker also shows extremely reliable step sizes, we have measured consistent step sizes in over 50 temperature cycles. Furthermore, the piezo legs maintain the piezo scanner ridged without having a voltage applied to them, helping maintain vibrational stability with minimal electrical cross talk to the tunneling current.

2.5 Noise considerations

As previously mentioned the STM only measures a tunneling current. The typical size of this tunneling current can be as small as 10 pA, this makes it susceptible to ambient and electrical noise. In order to measure the tunneling current a homebuilt current amplifier was constructed whose schematics are given in figure 2.8.

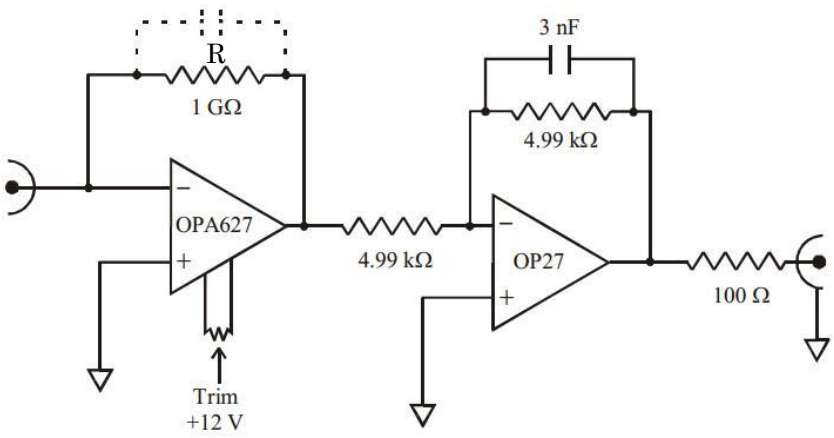

Figure 2.8 : Shematic of home built current amplifier used for measuring the tunneling current in our home built 5.2K STM.

As can be seen from figure 2.8 our current amplifier has an amplification of 10^9, and the current has a Johnson noise contribution (this is the noise caused from the thermal motion of the electrons) of $= \sqrt{\frac{4k_B TB}{R}} \approx 0.3$ pA , where B is the bandwidth which for our homebuilt amplifier the bandwidth is 3kHz, R is the resistance which is 1GΩ as seen in figure 2.8, and T is the temperature which is 300K for this calculation. However, our system runs at 5.2K hence while taking data the Johnson noise is actually reduced by a factor of $\sqrt{\frac{300k}{5.2K}} = 7.6$, making the contribution from Jonhson noise negligible at operating temperature. There is also noise that arises from the discrete nature of the current, this is called shot noise and its contribution to the current is $I_{Shot} = \sqrt{2e\bar{I}B} \approx 5.66 \times 10^{-10}\sqrt{\bar{I}}$, where e is the electronic charge constant and $\bar{I}$ is the average dc current. So as we can see the shot noise does not

contribute significantly unless the tunneling current is extremely small < 1 pA. As shall be shown momentarily the STM never operates at currents below 10 pA.

The Johnson and shot noise are not major contributors to the overall current noise. However, there is a capacitance at the input of the amplifier. This input capacitance ends up generating a current noise that is proportional to the input capacitance. The total noise on the amplifier can be described as [33] $i = \sqrt{\left(\frac{e_n}{R}\right)^2 + {i_n}^2 + \frac{4k_B T}{R} + \left(2\pi C_{input} e_n\right)^2}$, where e_n is the voltage noise, i_n is the current noise, R is the resistance indicate din figure 2.8, T is the temperature, k_B is Boltzmann constant, and C_{input} is the capacitance seen at the input of the amplifier. Clearly the first term is the ohmic noise cause by the input voltage noise of the op amp which is small considering the high resistance, the next term is the intrinsic input current noise, which is also small due to the op amps used in the circuit design, the following term is the Johnson noise. The final term is actually the main source of current noise contribution as previously stated, this is because the capacitance can be substantial, in our initial set up it was ~ 400 pF. This lead to a measured current noise of ~10 pA, we reduced this input capacitance by designing the amplifier such that it could be attached at the top the fridge and reducing the length of the coaxial cables that run down to the STM as much as possible. This reduced our input capacitance to ~100 pF, and reduced our measured current noise to ~2 pA. Hence, allowing us to operate at tunneling currents as low as ~5 pA. In practice we do not operate below ~10 pA for precautionary reasons. The current

noise can be further dropped by running home built low capacitance coaxial cables down the fridge in an isolated manner.

The other predominant noise source in the STM is vibrational noise. As can be seen from eq 2.3 one will see a fractional increase in the current that goes as $\frac{\delta I}{I} = -\frac{\delta z}{z_0}$ where $z_0 = \sqrt{\frac{8m_e\phi}{\hbar^2}}$ and z is the tip-sample separation. Typical values of ϕ are between 4-4.5 eV, making z_0~0.5 Å. This implies that for a 1% increase in current noise the z piezo would have to move by 0.5 pm. Hence sub pico meter vibrational stability is required to run an STM. In our home built STM this achieved by using 3 air springs with a resonance of roughly 1 Hz and the pan style walker which has a measured resonance of 1.5 kHz. The walker and the air springs create a coupled oscillator system which effetely cancels out all vibrational noise in a 1kHz bandwidth. In order to prevent any of the vibrational frequencies from being driven by the outside environment the STM is housed in a sound room. The sound room is covered with sound foam in order to dampen any potential vibrational noise which might leak in from the outside environment.

2.6 Spectroscopic Data Taking

From Eq. 2.6 it is clear that $\frac{dI}{dV} \propto \mathrm{LDOS(E)}$, this gives the STM a unique and powerful capability, since the derivative of the tunneling current is proportional to the local density of state (LDOS) it is possible to use the STM's sub Å spatial resolution to image the LDOS spatially $\mathrm{LDOS}(\vec{r}, \mathrm{E})$. Experimentally this accomplished by placing the tip at the desired location that one wishes to measure

the LDOS, the feedback loop is then turned off, hence the z piezo is held constant, then a small AC signal is feed to the bias voltage, making the tunneling current:

$$I(V + \delta V_{mod} \sin \omega t) \approx I(V) + \frac{dI}{dV}|_V \delta V_{mod} \sin \omega t + \cdots \quad (2.10).$$

The AC component of Eq. 2.10 can easily be read with a lock in amplifier. In the field this method is referred to as the standard lock in technique and it is how all the LDOS data presented in this thesis is collected. The ability to image the LDOS allows for various important measurements in superconducting samples. A typical averaged LDOS of Bi2212 is given in figure 2.9, clearly two particle hole symmetric peaks are present (which are the superconducting coherence peaks).By measuring the voltage location of the two peaks (Δ_-, Δ_+) we can define a measurement of the gap in Bi2212 as:

$$\Delta = \frac{|\Delta_- - \Delta_+|}{2} \quad (2.11).$$

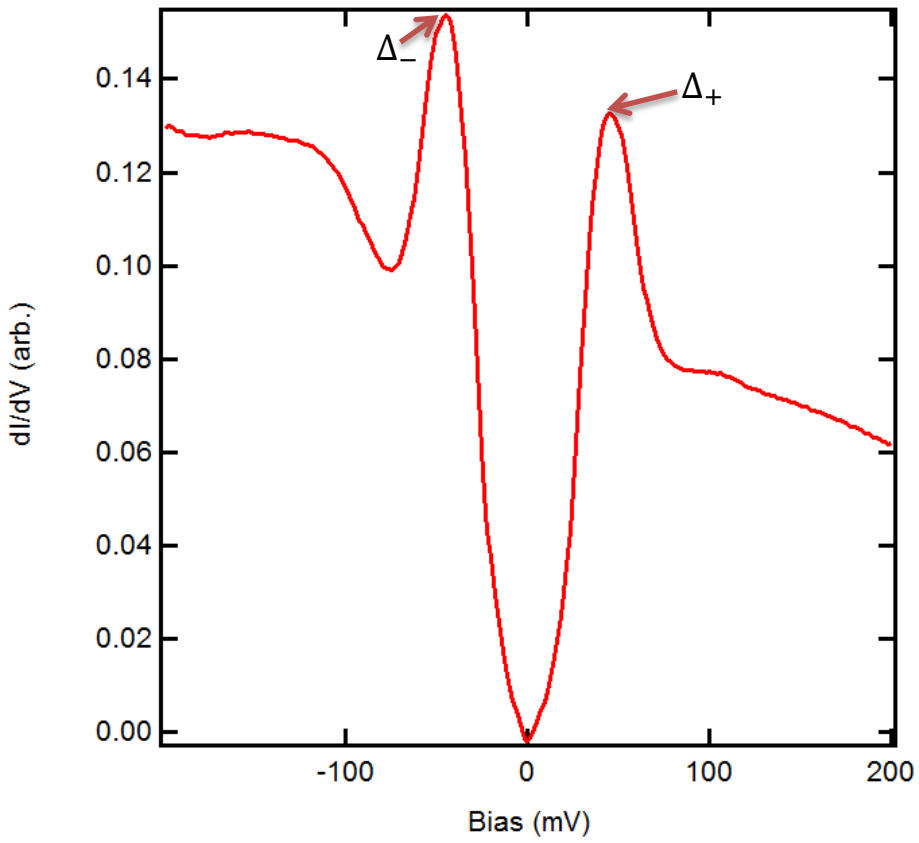

Figure 2.9: Typical averaged LDOS of an OP91K Bi2212 sample. Taken with set up conditions of I=200 pA and V=-200mV.

This allows the STM to measure the local gap variation over a superconducting surface which is termed a gap map, which from the point of view of a simple BCS superconductor the gap map should show no variation, however when the quantity is computed for Bi2212 there is large scale variations of the gap on a nm length scale as shown in figure 2.10. It is important to point out how these nano scale variations could not be observed with a bulk probe, in order to probe the LDOS at these subatomic length scales an STM becomes necessary.

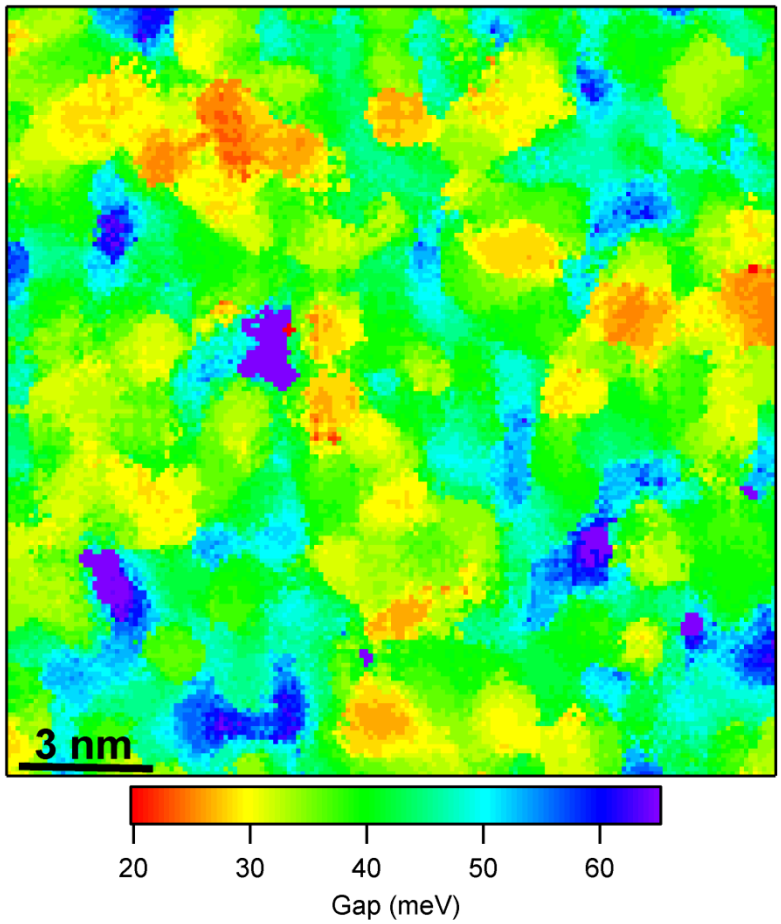

Figure 2.10: A typical gap map of an OP91K Bi2212 sample taken over a 15nm x 15nm field of view. With the set up condition of I=200 pA and V=-200mV. The field of view shows a gap variation of roughly 35 mV over a length scale of roughly 3nm.

The imaging of the LDOS can be quite lengthy depending on the spatial resolution required and the size of the field of view. This is because the lock in amplifier places the signal through a series of RC filters with a manually set time constant. The higher one sets the time constant the more averaging the lock in amplifier performs on the signal. However, since the filters are RC filters there is an exponential rise time one must wait in order to recover the averaged signal which is dependent on the preset number of poles of the filter, which for data presented in this thesis is 24 dB/octave. It is trivial to work out that one must wait

5 time constants in order to recover 99% of the signal if the number of poles in the filter is set to 24 dB/octave. The time constant is limited by the frequency of the bias twitle which must be less than the bandwidth of the amplifier, in particular it is necessary to set this frequency below the 3kHz roll off of our home built current amplifier so that no signal is lost. In the case of the data presented in this thesis the bias modulation frequency is set near 1kHz, hence allowing for the time constant to be set to 10 ms or more. Which means that we must wait 50 ms at each point in energy, however there is also a filter on the input of the controller which is set to the same time constant as the lock in, this forces us to wait another 50 ms. There will also be a delay time between each point spatially in order for the piezo to relax, this is set manually and is typically .1 min/scan line, there is also a 600 ms delay per spatial point which comes from the controller electronics. Hence, if one wishes to take 256x256 pixel imaging of the LDOS it would take ~36 hours. During this time period the STM is mostly out of feedback and very susceptible to vibrational noise, hence why vibrational stability is imperative.

Furthermore, the LDOS can also be used to find the location of particular atoms, in particular in Bi2212 the dopant oxygen atoms where found to have an LDOS signature at bias voltages of -1 V [34, 35]. This experiment can be dangerous to the junction because as previously mentioned applying high bias voltages to ceramic surfaces such as Bi2212 can result in completely destroying the surface. Therefore, in previous studies it could take months to take the data to find these dopant atoms. However, we have developed a new technique. By taking advantage

of the fact that the lock in amplifier averages the dI/dV signal, it is possible to set the gain of the feedback loop extremely low so that there is minimal z piezo variation while still allowing the STM controller to scan the surface. The z piezo movement is minimized due to the fact that lowering the gain of the feedback loop lowers the response of the z piezo, hence the piezo will only pull in and out of the surface in response to sizable features. Since we are dealing with an atomically flat surface the movement will be minimal. The scan speed can be chosen such that the time between each point is longer than the averaging time of the lock in amplifier and the bias modulation can be set extremely high (~100 mV) as to amplify the signal. This allows the junction resistance to be set at a very high value ~50GΩ making the junction extremely safe even with the high bias voltage, since the tip is so far away from the surface. If one knows the spectroscopic signature of the dopant atoms, in the case of Bi2212 its -1V, the bias voltage can be set to the particular voltage and the STM can be allowed to scan he surface therefore yielding a $LDOS(\vec{r}, E)$ at the energy in question. This allows one to obtain the data of the dopant oxygen atoms in Bi2212 in a time scale of ~30 minutes, a typical result is show in figure 2.11.

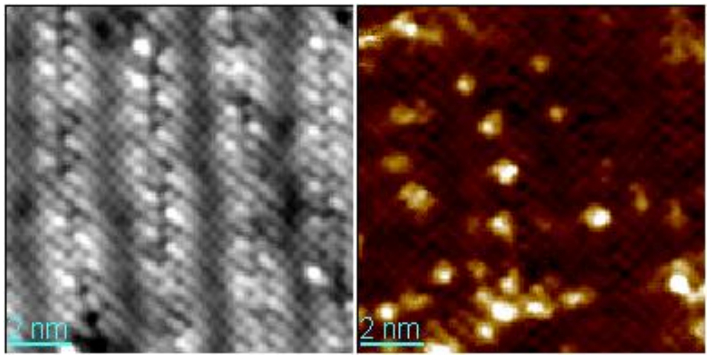

Figure 2.11: A) Topographic image of UD Bi2212 with 1.5% Fe doping over a 6 nm x 6nm FoV with set up conditions of I=10 pA and V=-1V. B) $LDOS(\vec{r}, -1V)$ over the same FoV as the topography, where the white spots represent areas of increased spectral weight believed to be dopant oxygen atoms.

There is also another data taking mode for STM, it is possible to image the LDOS over a straight line. This is much more time efficient than a map if one wants to find the spatial variation of the LDOS along and axis of high symmetry. In our home built STM this is accomplished by selecting two points on the topographic image a line is then extrapolated between the two points and spectra is taken along the extrapolated line, the number of spectra taken along the line is set manually by the user. A typical line cut data is shown in figure 2.12.

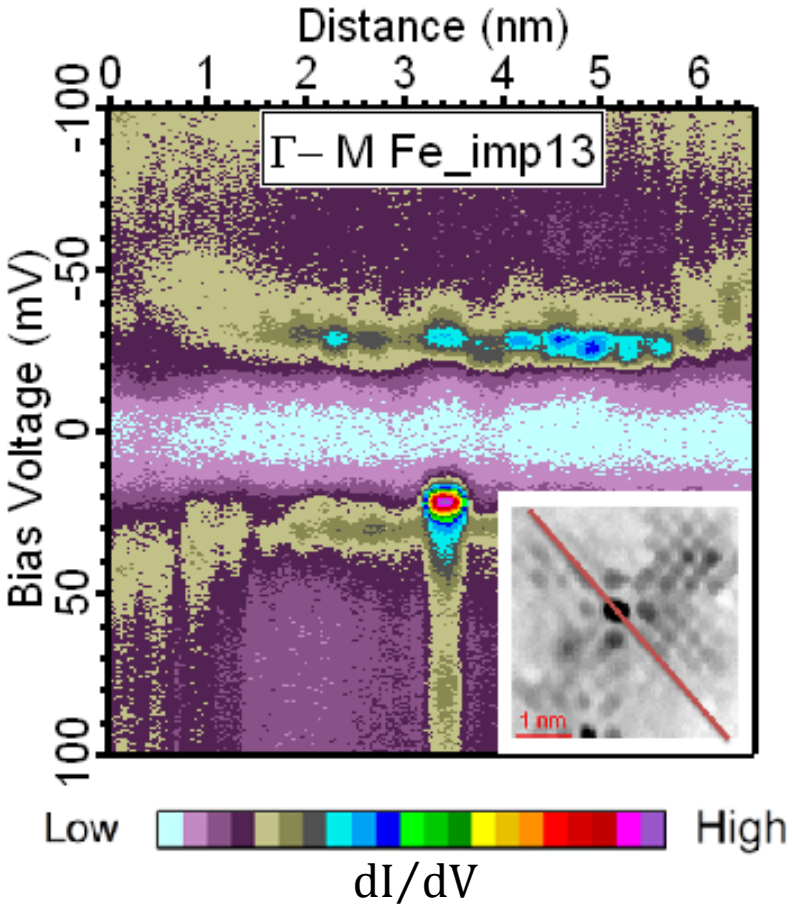

Figure 2.12: Typical line cut on OP Bi2212 with 0.5% Fe dopant. The inset shows the $LDOS(\vec{r}, 23.5V)$ of an Fe impurity. The red line indicates the line over which the spectra where acquired, there are 1000 spectra displayed in the figure with initial set conditions I=100 pA and V=-100 mV, the bright red spot on the line cut indicates the Fe impurity.

Finally it is also possible to measure I vs V, this quantity represents the integrated density of state and of course can be mapped spatially and in a line cut. Taking IV has the advantage of not having to put the current through the lock in amplifier hence IV can be mapped spatially in half the time of dI/dV. But typically the quantity of interest is the LDOS, and if one wishes to take the numerical derivative of IV and have the same signal to noise as the lock in measurement by taking the numerical derivative it is necessary to take a large number of points in energy which in turn makes the IV mapping take just as long as dI/dv mapping.

CHAPTER 3

QUASIPARTICLE INTERFERENCE

3.1 Theory

One of the unique capabilities of STM is that it allows for the spatial imaging of the LDOS while simultaneously allowing one to probe the k-space structure of the electronic states. This can be accomplished by realizing that by definition the LDOS is $\mathrm{LDOS}(\vec{r},V) = -\frac{\pi}{2}\,\mathrm{Im}\,G(\vec{r},\omega)$ where $G(\vec{r},\omega)$ is the real space green's function. In the presence of a scattering potential the green's function to first order can be computed as follows,

$$G(\vec{r},\omega) = G_0(\vec{r},\omega) + G_0(\vec{r}-\vec{r_1},\omega)V(\vec{r_1})G_0(\vec{r_1}-\vec{r},\omega) \qquad (3.1).$$

If we assume that the potential is a scalar potential and then take the Fourier transform of the second term of Eq. 3.1 the surviving term looks as follows,

$$G(\vec{q},\omega) = \int d^2\vec{k}\; G(\vec{k},\omega)\, G(\vec{k}+\vec{q},\omega) \qquad (3.2).$$

Where $G(\vec{k},\omega)$ is the k space greens function in the Nambu space given in Eq. 1.9, this leads to the surviving term of 3.2 being $\int d^2\vec{k}\; \mathrm{Re}\big[G(\vec{k},\omega)\big]\mathrm{Im}[\,G(\vec{k}+\vec{q},\omega)]$. However, for reasons that as of date are unclear, STM data is interpreted with in the so called JDOS model which is as follows,

$$\mathrm{JDOS}(\vec{q},\omega) = \int d^2\vec{k}\; \mathrm{Im}\big[G(\vec{k},\omega)\big]\mathrm{Im}[\,G(\vec{k}+\vec{q},\omega)] \qquad (3.3).$$

Technically speaking the term in 3.3 does not survive in the expansion of 3.2, and it is a question of theoretical intrigue as to why 3.3 describe the STM data.

Experimentally the JDOS can be realized as follows:

1) Topographically map out a region of interest

2) Map the LDOS spatially and in energy in the region of interest

3) Fourier transform the spatial LDOS in each energy layer

This was first accomplished by [36,37] the resulting JDOS is given in figure 3.1. Immediately one notices the appearance of 28 peaks, which as we will see shortly due to symmetry, are only 7 unique peaks.

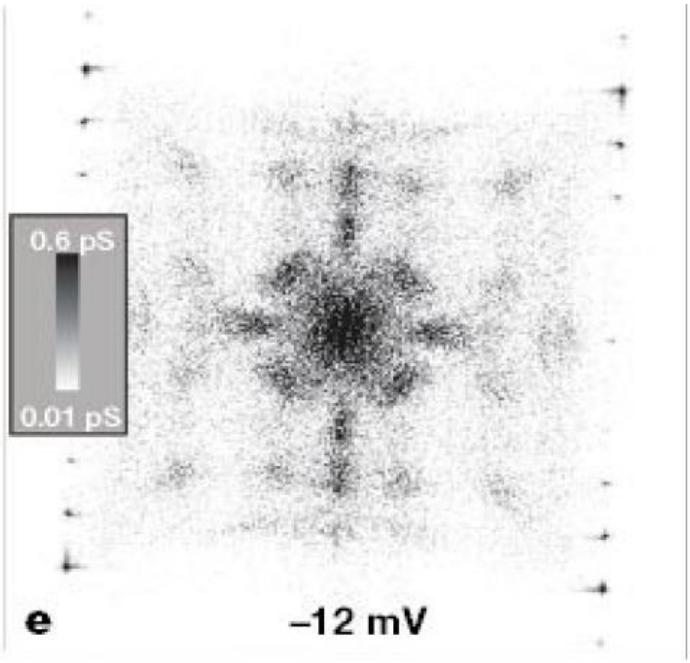

Figure 3.1: The FT-STM measured by [36] in an optimally doped Bi2212 sample.

In order to understand how the peaks are connected to k-space, let us examine the Fermi surface of Bi2212, this is simulated in figure 3.2 using the tight binding calculations from [38]. We immediately notice that the Fermi surface is four fold symmetric with 4 hole pockets as expected. The application of superconductivity to the Fermi surface leads to the appearance of superconducting banana's around the hole pockets, as shown in figure 3.3. The bananas are a consequence of the fact that the superconducting state generates a forbidden zone

(gap) for electronic states but does not cause them to disappear, therefore they "pileup" outside the gap.

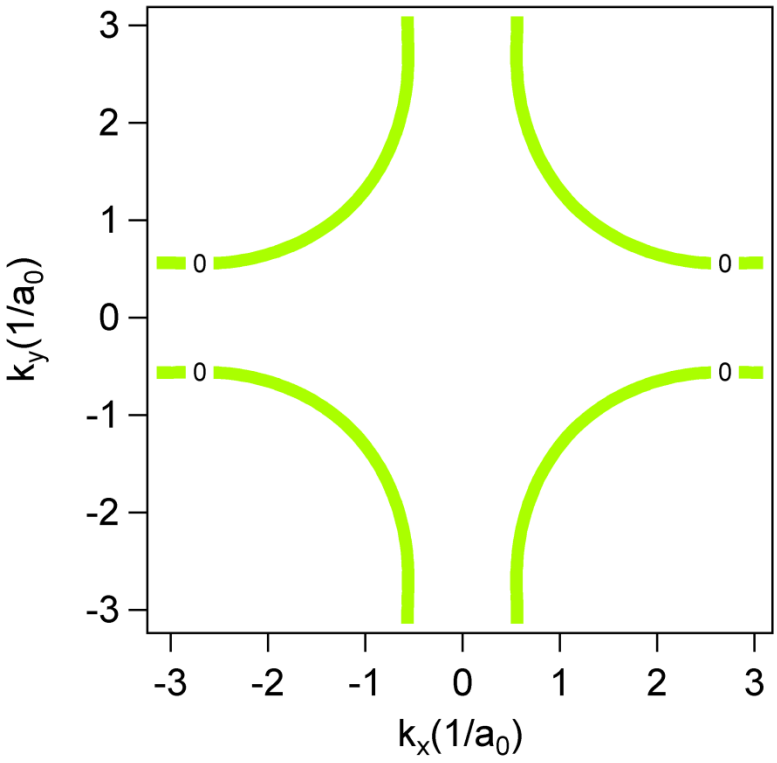

Figure 3.2: Simulated Bi2212 Fermi surface using the band structure from [38].

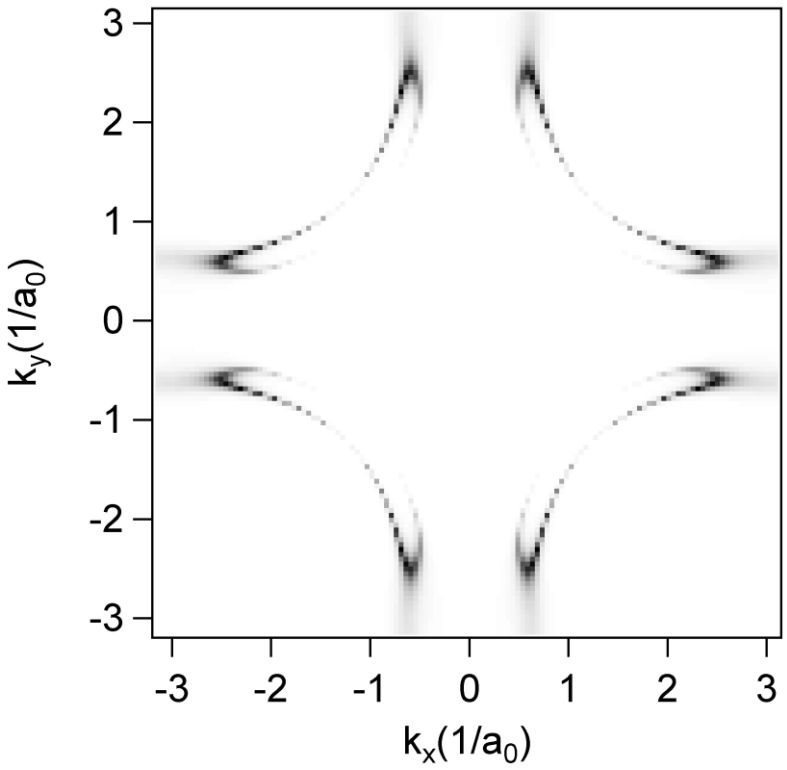

Figure 3.3: Simulated A(k,ω) showing the superconducting banana's around the hole pockets of the Fermi surface given in figure 3.2.

The quaisi particle density of state at a particular energy (E) is proportional to $\int \left|\nabla_{\vec{k}}\varepsilon(\vec{k})\right|^{-1}$ where $\varepsilon(\vec{k})$ is the band structure. Therefore, in the presence of a scatterer we expect the states near the edges of the banana's to contribute the most to the quaisi particle density of states. This creates seven unique wave vectors, as shown in figure 3.4. Within the context of Eq. 3.3 this should manifest itself as 24 peaks as observed by [36,37]. The symmetry of the d-wave gap causes the banana's to move towards the node as the energy approaches the Fermi surface. The peaks should be dispersive, which they are observed to be.

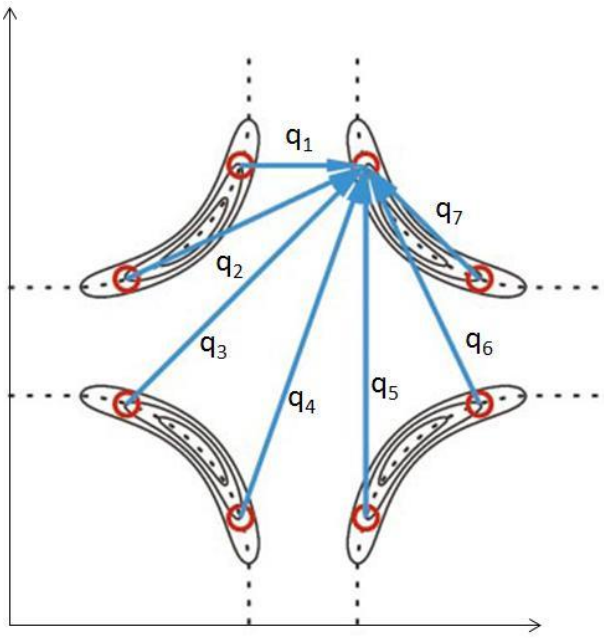

Figure 3.4: the seven unique wave vectors formed by quasi particles scattered from the edges of the superconducting banana [36].

Using the symmetry of the Fermi surface, it is possible to relate the peaks (q vectors) to reconstruct the Fermi surface and the gap. This geometrical relationship is as follows,

$$\vec{q}_1 = (2k_x, 0)$$

$$\vec{q}_2 = (k_x + k_y, k_y - k_x)$$

$$\vec{q}_3 = (k_x + k_y, k_y + k_x)$$

$$\vec{q}_4 = (2k_x, 2k_y)$$

$$\vec{q}_5 = (0, 2k_y)$$

$$\vec{q}_6 = (k_x - k_y, k_y + k_x)$$

$$\vec{q}_7 = (k_x - k_y, k_y - k_x).$$

The fact that peaks are dispersive also allows for the reconstruction of the k-space gap by using the geometrical relationship $\theta_{\vec{k}} = \tan^{-1}(\frac{\pi - k_y}{\pi - k_x})$, where $\theta_{\vec{k}}$ is the angle between the edge of the zone and the Fermi surface. The reconstruction of these quantities was done by [36] and the results are shown in figure 3.5.

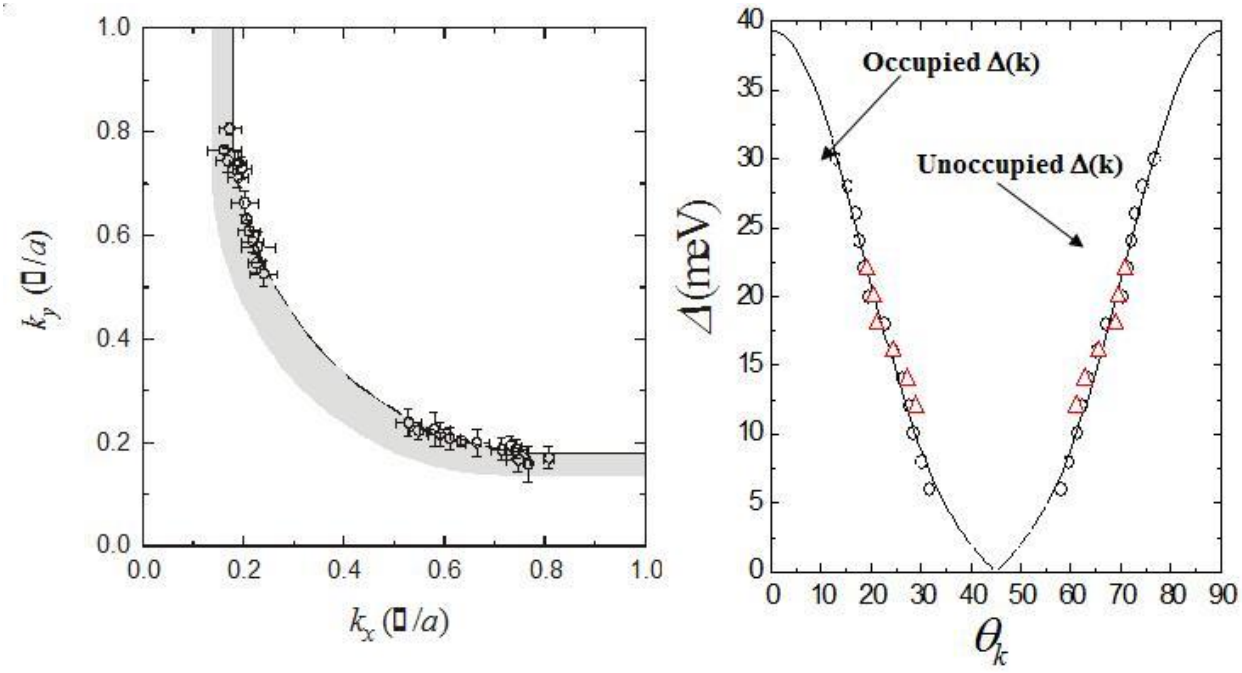

Figure 3.5: The Fermi surface and k-space gap reconstruction from [36].

Immediately we encounter some striking features. First there is a lack of spectral weight near the nodal direction in the Fermi surface reconstruction. Second the QPI signal terminates exactly where the anti-ferromagnetic parent compound Fermi surface intersects the current Fermi surface. Finally, the reconstructed gap does not look like the simple d-wave gap,

$$\Delta_{\vec{k}}(\theta_{\vec{k}}) = \Delta_0 \cos 2\theta_{\vec{k}}, \tag{3.4}$$

but rather looks like a d-wave gap with a second harmonic contribution, given as follows,

$$\Delta_{\vec{k}}(\theta_{\vec{k}}) = \Delta_0(B * \cos 2\theta_{\vec{k}} + (1 - B) * \cos 6\theta_{\vec{k}}) \quad (3.5).$$

3.2 Comparison to Angle Resolved Photo Emission

Angle resolved photo emission (ARPES) provides a direct probe to the k-space nature of the electronic states. Therefore, one would expect the Fermi surface and k-space gap seen by QPI to agree with ARPES. However, ARPES measurements of the Fermi surface show spectral weight all the way down to the node [48,39,40]. Furthermore, a recent experiment by [39, 40] indicate that across the full range of the phase diagram the k-space gap has the expected simple d-wave form. A graph of the k-space gap measured by ARPES is given in figure 3.6.

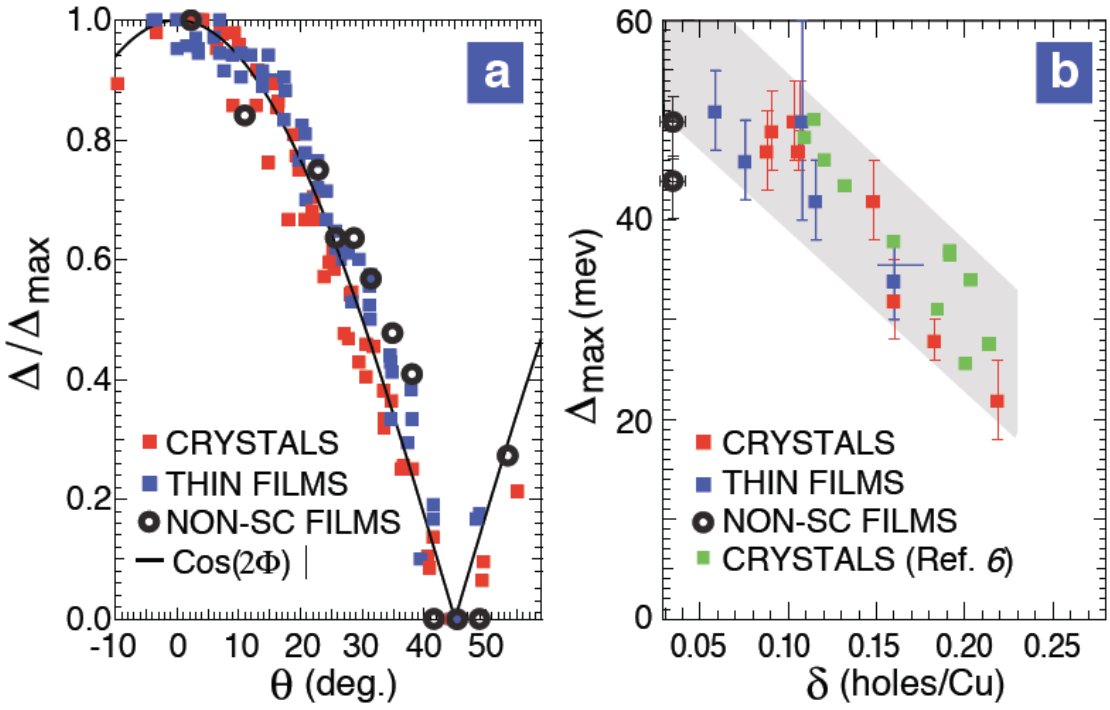

Figure 3.6: (A) The reconstructed k-space gap from [39], normalized by the gap maximum. (B) The maximum gap as a function of number of holes.

This figure suggests that the empirical nature of the gap is that given by Eq 3.4 and not Eq. 3.5. A reasonable assumption is that the gap measured by QPI, Eq.

3.5, is simply caused by experimental effects. If that is the case then perhaps the gap will look the same across the phase diagram. This experiment was done by [41], and the results are given in figure 3.7.

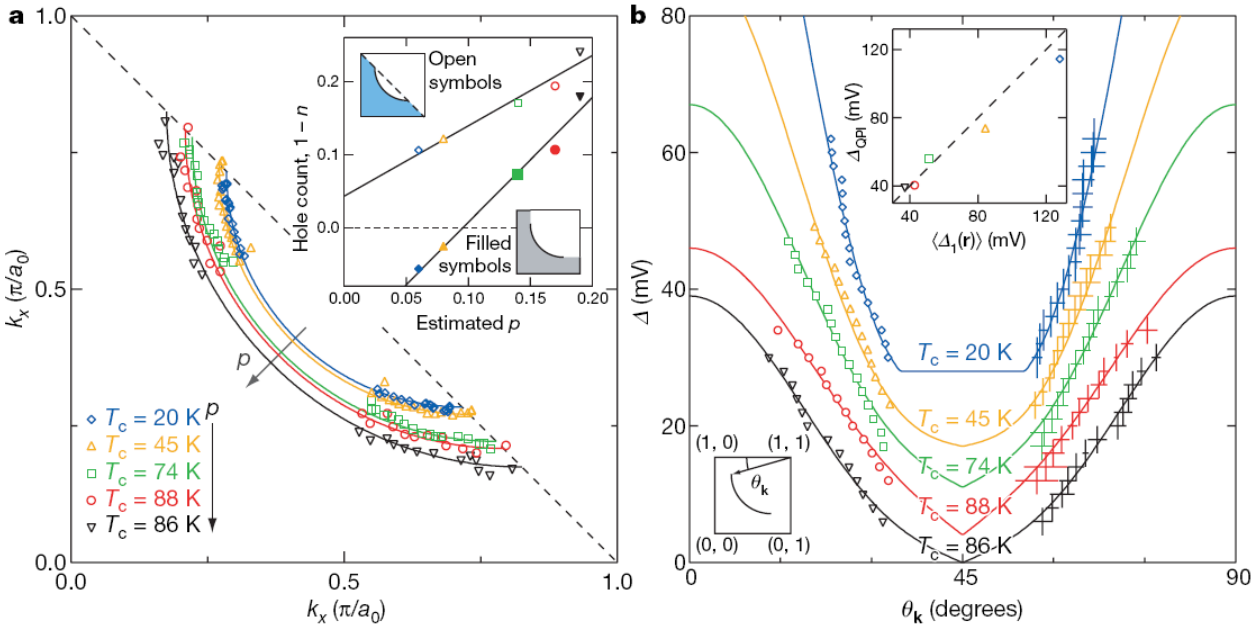

Figure 3.7: (A)The reconstructed upper quarter of the Fermi surface from [41] across 6 different hole doping's. (B) The reconstructed k-space gap across 6 different doping's, offset for clarity.

Figure 3.7 clearly shows that the empirical nature of the k-space gap measured by QPI varies as a function of doping. In particular the B constant from Eq. 3.5 seems to be increasing as the sample becomes more underdoped. In particular the UD 20K sample shown in figure 3.7 cannot be fitted quantitatively without a substantial B term. This is in direct contrast to what ARPES observes across the phase diagram. Furthermore, an experiment was recently done where the doping was kept constant as the temperature was varied in order to reconstruct the k-space gap using QPI [42]. The results are given in figure 3.8.

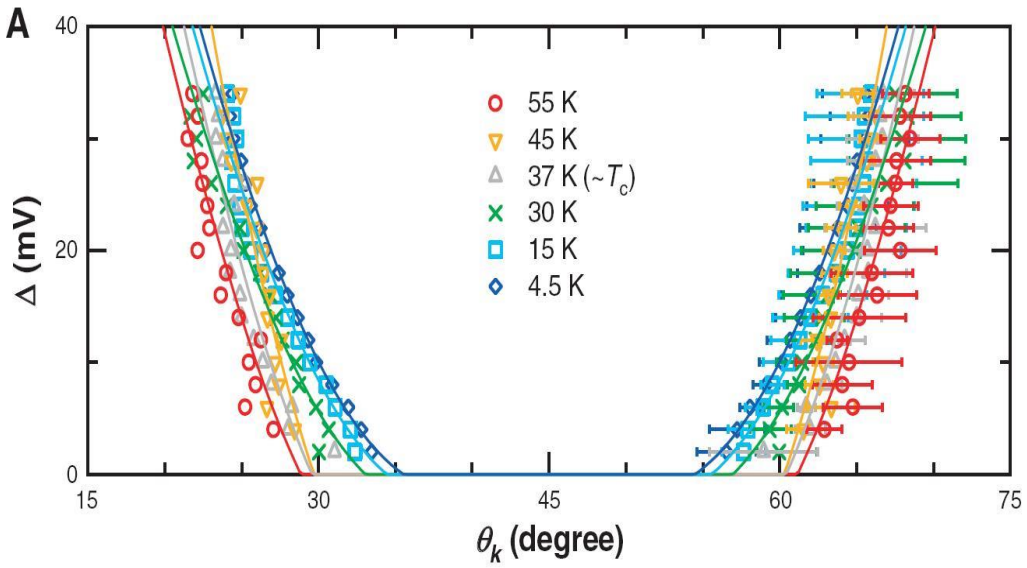

Figure 3.8: The reconstructed k-space gap of a underdoped Tc=37K sample as a function of temperature [42].

The results seem to suggest that the k-space gap begins to avoid the node more as the temperature increases. This is consistent with the formation of a so called "Fermi arc", which is the formation of a non-superconducting section of the Fermi surface. The idea is that if these Fermi arcs exist then only the superconducting portion of the Fermi surface would contribute to the QPI signal, hence creating this nodal avoidance. However, recent ARPES work indicates that such a partially gapped Fermi surface [40]. So the question is raised, is the STM observing some intriguing new physics that ARPES is not sensitive too, or can we reconcile the two experiments by carefully considering experimental effects.

3.3 Simple QPI simulation

The simplest way to begin to examine the experimental effects on the QPI signal is to consider the Green's function from Eq. 1.9, $G^{-1}(\vec{k},\omega) = (\omega + i\delta)I - \varepsilon_k\sigma_3 -$

Δ_k, where δ can be thought of as broadening, and Δ_k is just the d-wave order parameter $\Delta_0(\cos(k_x) - \cos(k_y))$. The simplest QPI simulation simply involves using the band structure from [38], and computing the JDOS from Eq. 3.3. The results of simulation are given in figure 3.9 B.

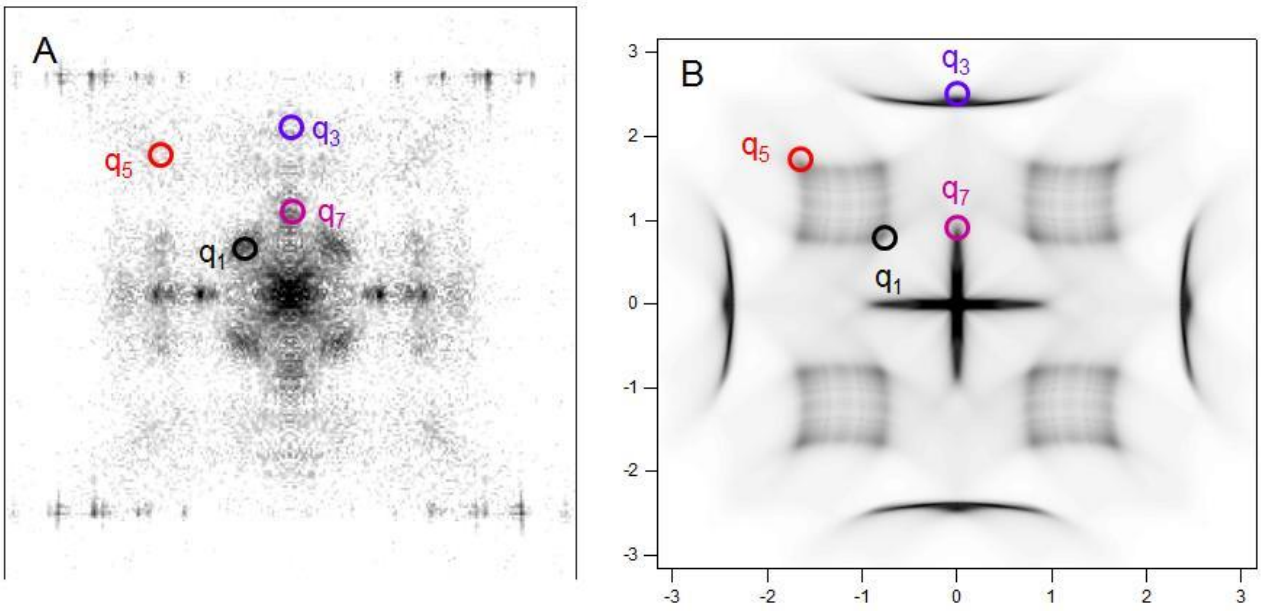

Figure 3.9: (A) Raw QPI data of an optimally doped sample. (B) Simulated data using the simple model.

When compared to figure 3.9 A, which is a raw QPI signal, we see that it is possible to identify the q vectors, but we do not find good qualitative agreement between the two pictures. It is also possible to reconstruct the k-space gap and Fermi surface. The results are shown in figure 3.10 A and B.

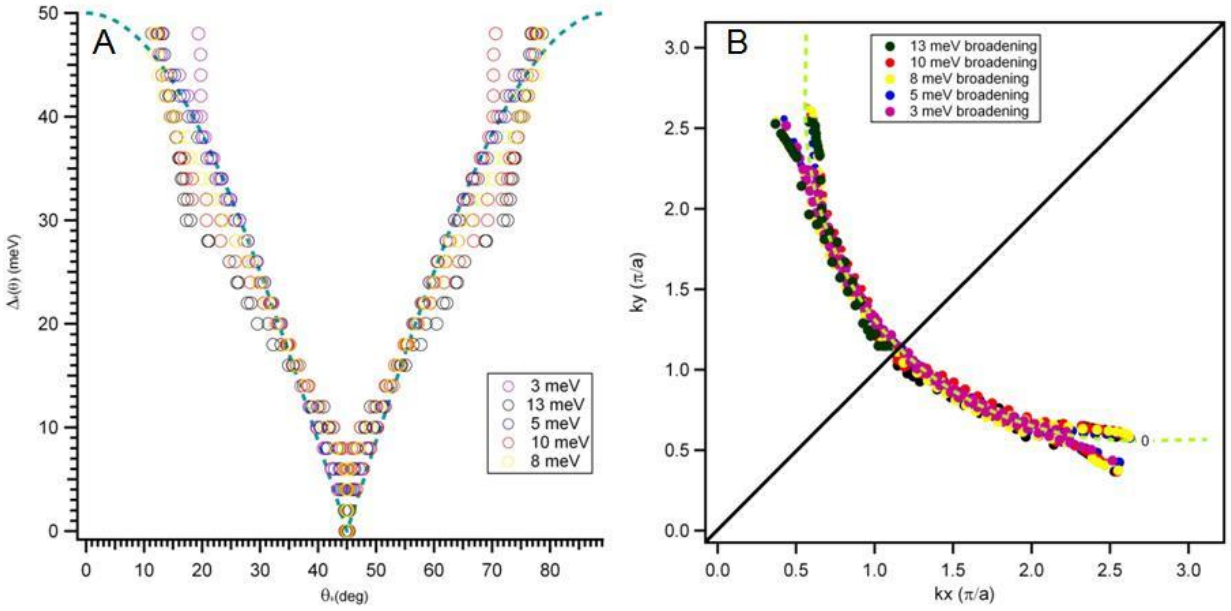

Figure 3.10: (A) Reconstructed k-space gap from the basic simulation as a function of broadening. (B) Reconstructed Fermi surface from the basic simulation as a function of broadening.

It is immediately obvious that the basic simulation fails to capture any of the experimentally observed effects. There is spectral weight at the nodes and the gap seems to consistently follow the dashed line which is Eq. 3.4. The strange behavior near the zone face is due to the van hove singularity caused by the band structure. This suggests that the simple simulation of the QPI signal is not sufficient to explain the experimental effects.

3.4 Matrix Element

The "bare model" ignores certain experimental effects, such as matrix elements. In ARPES the matrix element has a drastic effect on the observed signal [44].One can use the ARPES signal to compute the JDOS, [43] showed that the ARPES matrix element has a strong effect on the JDOS. In the STM signal the hopping matrix element worked out by [45], helps explain various phenomena such

as, the spatial structure of Zn and Ni impurities in Bi2212 [46]. This same matrix element also explains the missing zero bias resonance observed in vortices in Bi2212 [47]. This suggests that the hopping matrix element could be playing a significant role in the QPI signal.

The hopping matrix element computed by [45] is $|M|^2 \propto \left|\cos k_x a - \cos k_y a\right|^2$. It is a simple to step to simulate the QPI signal with the inclusion of a matrix element, the resulting QPI signal is given in figure 3.11 A. Once again we see poor qualitative agreement when comparing the simulated signal to the experimental signal. The reconstructions of the Fermi surface and k-space gap are given in figure 3.12. In contrast to the "bare model" it becomes obvious that the nodal states are suppressed by the matrix element, which agrees with the experimentally observed signal. However, the nodal avoidance seen by [42] is not present in this model, suggesting that Fermi arcs remain a possibility.

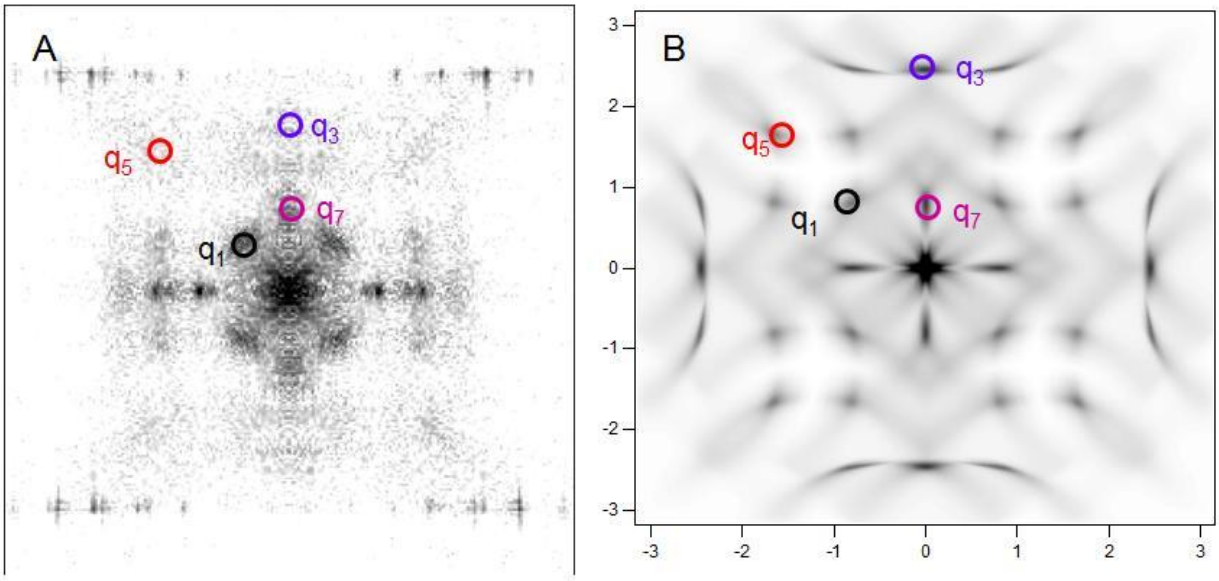

Figure 3.11: (A) Raw QPI data of an optimally doped sample. (B) Simulated data using the simple model with the hopping matrix element.

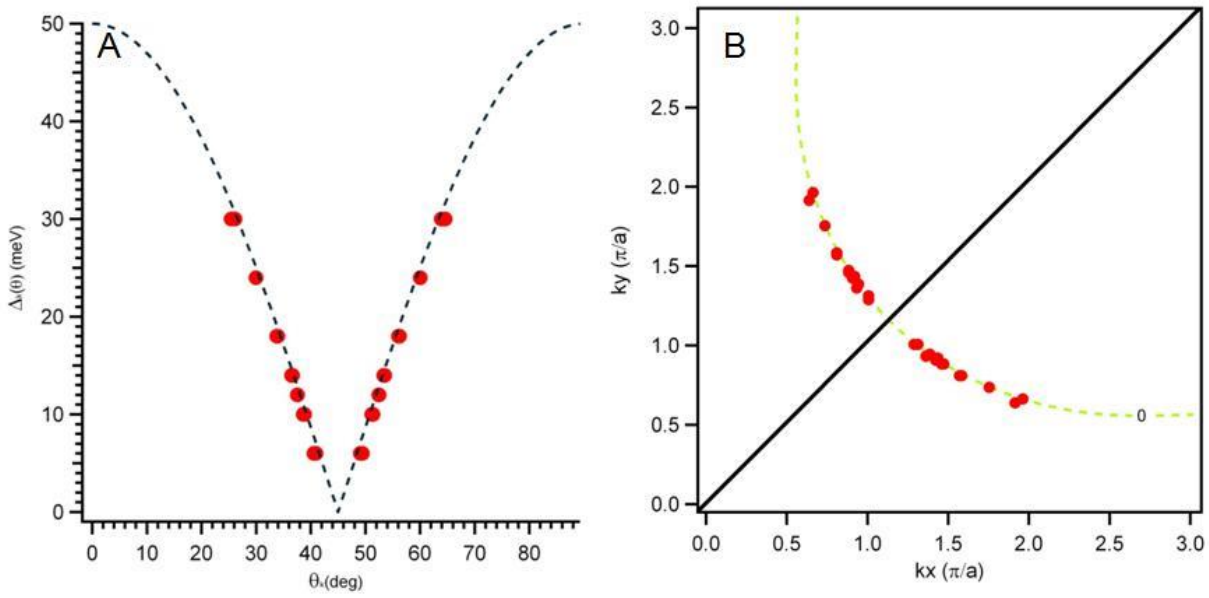

Figure 3.12: (A) Reconstructed k-space gap from the basic simulation with the hopping matrix element. (B) Reconstructed Fermi surface from the basic simulation with the hopping matrix element.

3.5 Finite k-space resolution

The QPI is a result of a standing wave pattern formed from scattering sites in Bi2212, this suggest that there should be a finite k-space resolution. We modeled this by convolving Eq. 1.9 with a 2-d Gaussian function, and we assumed that the length scale of the standing wave was approximately 250 lattice constants. When the Gaussian convolution is combined with the matrix element effect described in the previous section we get good qualitative agreement between the experimental data and the simulated data as shown in figure 3.13.

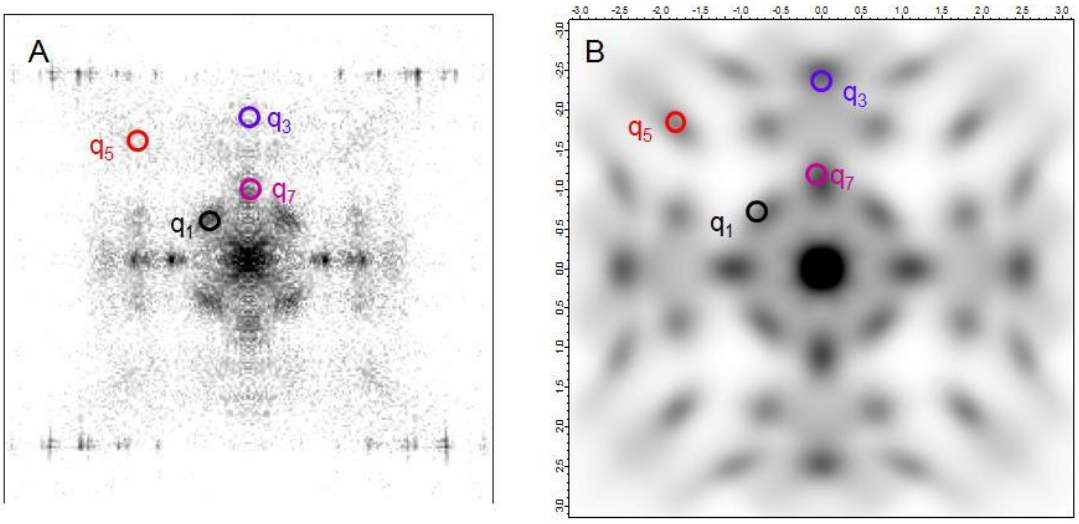

Figure 3.13: (A) Raw QPI data of an optimally doped sample. (B) Simulated data using the simple model with the hopping matrix element and k space broadening.

The reconstruction of the Fermi surface and the k-space gap is given in figure 3.14, this clearly shows the same behaviors as a Fermi arc. As the broadening is increased it seems like the gap avoids the node at an earlier angle.

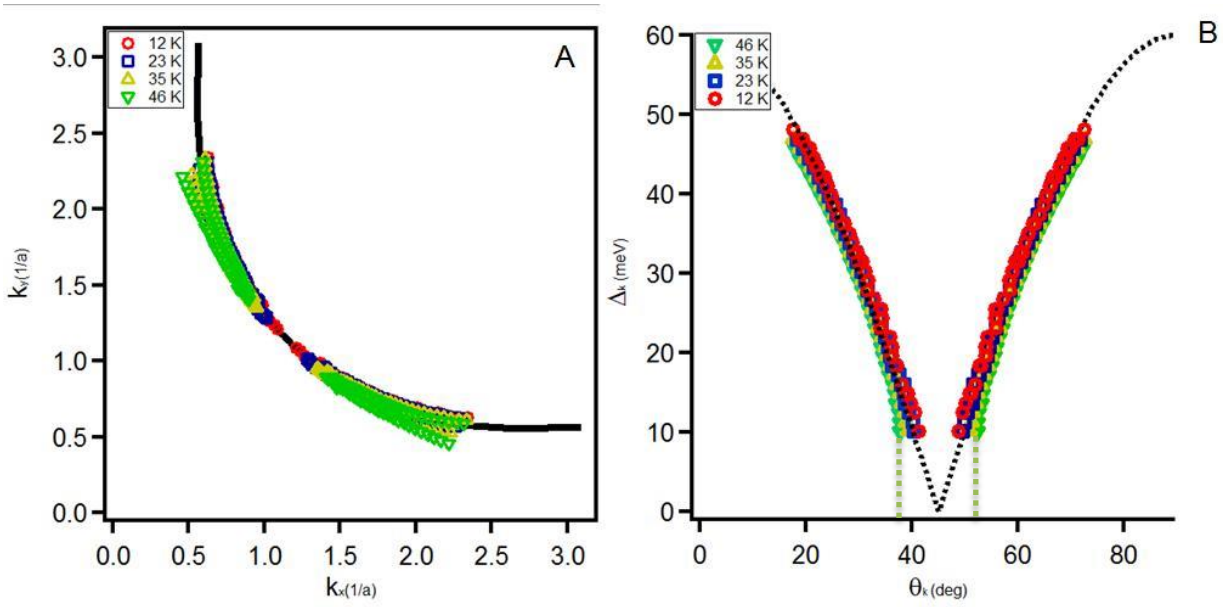

Figure 3.14: (A) Reconstructed Fermi surface from the full simulation at multiple broadenings. (B) Reconstructed k-space gap from the full simulation at multiple broadenings.

3.6 Experimentally Simulating Fermi Arcs

In order to test the validity of the effect of broadening on the QPI signal we decided to take advantage of the bias modulation used in the standard lock in technique explained in chapter 2. Increasing the bias modulation signal effectively broadens the dI/dV signal which is then Fourier transformed to retrieve the QPI signal. A schematic of this idea is given in figure 3.15. The concept is to increase the amplitude in order to mimic the broadening, which is essentially what increasing the temperature accomplishes. The experiment was done as two different bias modulation voltages, 2 mV and 6 mV. The QPI reconstructions using q1 and q7 for an under doped 58K sample are given in figure 3.16. The results seem to indicate that the STM data can artificially produce "Fermi arc" behavior just from increasing the broadening effects of the experiment.

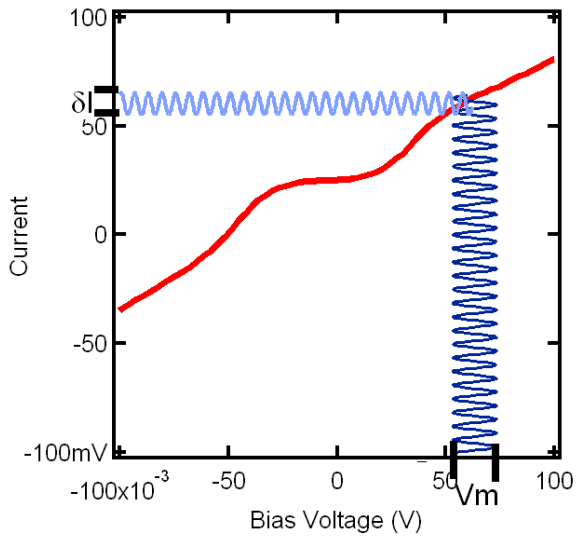

Figure 3.15: A simple schematic of how increasing the bias modulation effectively broadens the dI/dV signal. Where the red line represents the I-V characteristic of Bi2212 and the blue line indicates the bias modulation of some voltage amplitude Vm and δI is the amount of current measured after it has been broadened.

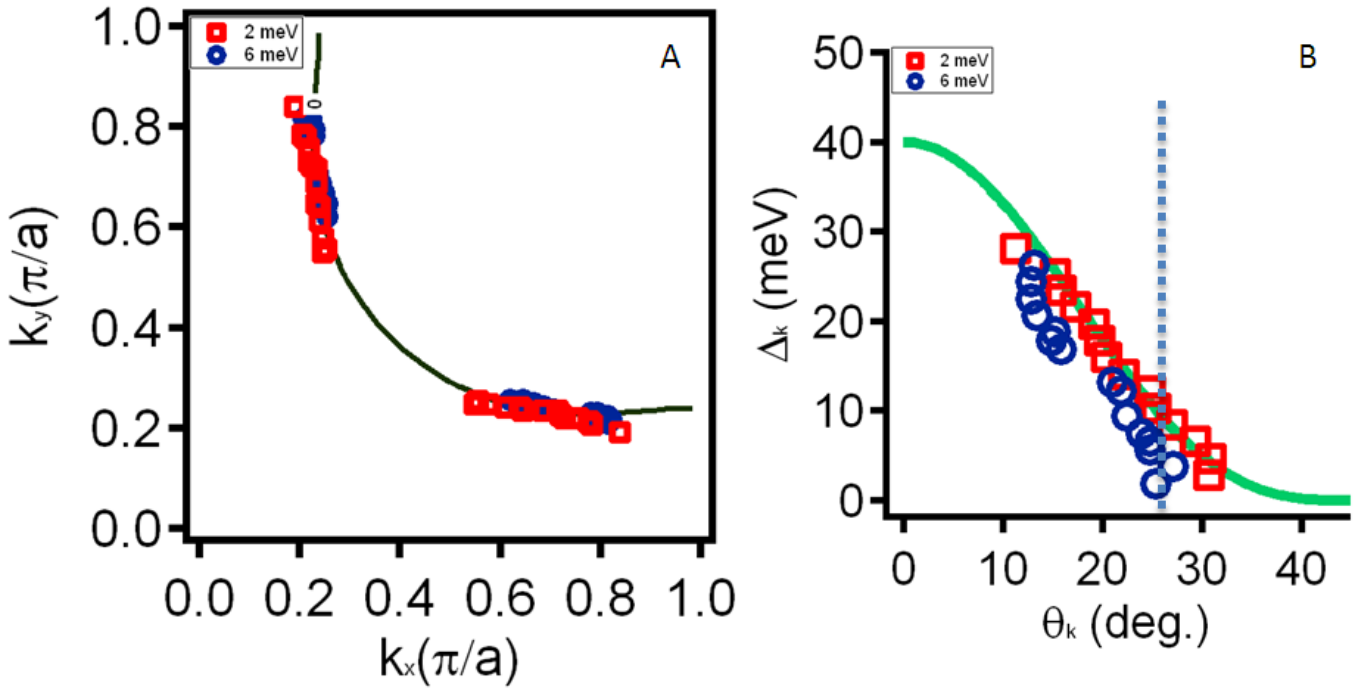

Figure 3.16: A) Reconstructed Fermi surface using q1 and q3 on a UD58K sample at two different bias modulations, where the blue circles represent a bias modulation of 6 meV and the red squares represent a bias modulation of 2 meV. The black line represents the computed Fermi surface of Bi2212 using a tight binding model. B) Reconstructed k-space gap from the same UD 58K sample at two different bias modulations. The green line represents the fit to Eq. 3.5. The data was taken with a set up condition of I_{set}=200 pA and V_{bias}=-200 mV.

3.7 Conclusion

Our simulations suggest that the suppression of the nodal states in Bi2212 is completely due to the hopping matrix element. Furthermore, the phenomena reported by [42] of Fermi arcs can be completely understood by considering experimental broadening effects. This is illustrated in figure 3.15, were the nodal avoidance from the simulations is compared to the nodal avoidance from [42]. It is clear that the simulations show as much nodal avoidance as the experimental measurement, suggesting that a significant portion of their signal is completely due to the experimental broadening effects.

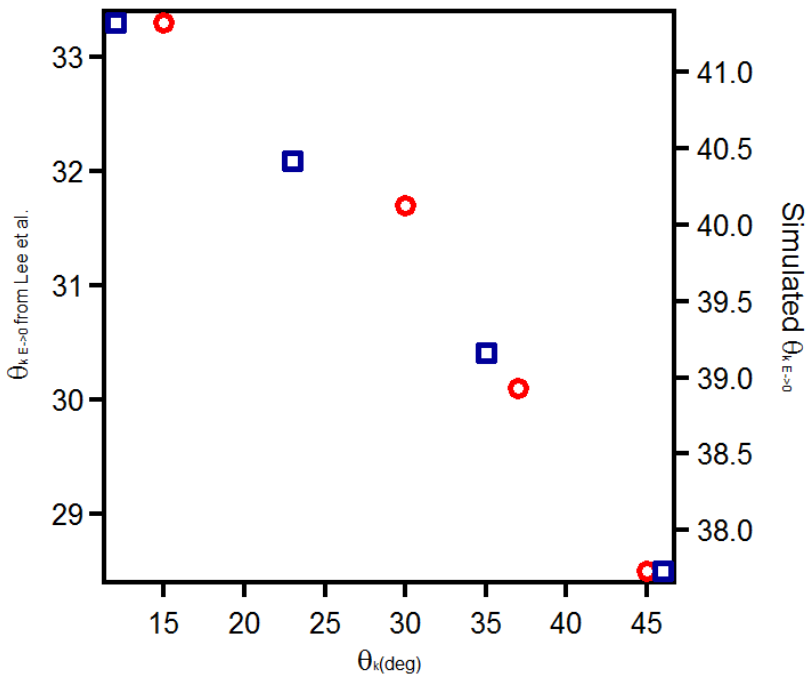

Figure 3.17: Comparison of nodal avoidance from [42] with the simulated data. The simulated data is given by the blue squares and its axis is displayed on the left hand side and the data from [42] is shown as red circles and its axis is displayed on the left hand side.

This allows for reconciliation with ARPES, and gives a better interpretation of the QPI data. The experimental broadening effects are now better understood we have created a framework where more complicated Green's functions can now be simulated. The experiment described in section 3.6 also suggests that interpretation of this so called "Fermi arcs" in terms of conventional physics is very easy once experimental effects are not considered carefully.

CHAPTER 4

MAGNETIC IMPURITIES IN Bi2212

4.1 Impurity Studies in Bi2212

Previous experiments have used Spectroscopic Imaging Scanning Tunneling Microscopy (SI-STM) on cuprate samples with Ni and Zn substituted for Cu in the CuO plane to probe the nature of the superconducting state [22,23]. These experiments revealed the existence of a quasi-bound state on the impurity site which destroys the superconducting gap measured by SI-STM. Theoretical investigation [46] into the nature of these quasi-bound states suggest that they are predominantly produced by a large charge scattering potential. The study of these impurities allowed for a microscopic interpretation of discrepancies between μSR and NMR and furthermore identification of the strong scattering potential led to an explanation as to why Zn suppresses the T_c 20% more than Ni which at the time was thought to produce a magnetic potential, due to its magnetic moment (~1.5μ_B) [49].

The spectroscopic signatures of Ni and Zn are shown in figure 4.1. In the case of Zn we see a resonance near zero bias which is consistent with a strong charge impurity [50]. In the case of Ni we see an intra-gap resonance peak indicating that the strength of the scattering impurity is weaker than in the case of Zn and in fact it was proven [46] that there is a weak magnetic component, however charge scattering is still the predominant scattering channel.

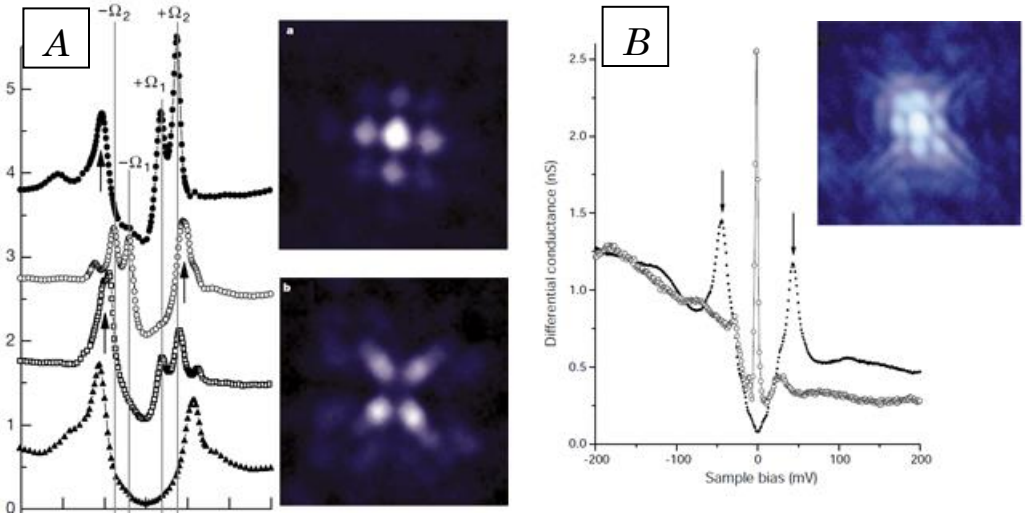

Figure 4.1: A) LDOS(E) of a Ni impurity in Bi2212 at different locations, the top spectra shows the LDOS on site. The top inset shows the positive LDOS(E,$\vec{r}$) at the impurity energy and the bottom inset shows negative LDOS(E,$\vec{r}$). B) LDOS(E) of a Zn impurity in Bi2212, the black spectra is the normal spectra in Bi2212. The inset shows LDOS(E,$\vec{r}$) for a Zn impurity.

In traditional superconductors magnetic impurities appear to be extremely destructive to superconductivity [51]. Recent work dealing with magnetic impurities in traditional superconductors [52,53] also reveal the appearance of a local Kondo effect on the impurity site. The Kondo effect results from a broken superconducting pair being used to screen the local moment. However, work on Ni impurities suggested that magnetic potentials have not been seen in a cuprate system. A recent bulk study [54] seems to indicate that the substitution of Fe atoms into the CuO plane in $Bi_2Sr_2CaCu_2O_{8+\delta}$ (Bi2212) not only suppresses the T_c but also appears to retain a magnetic moment down to T_c. In particular Fe was found to have a magnetic moment of ~5.2 μ_B which is 3.5 stronger than Ni.

4.2 STM studies on magnetic impurities

One might ask what a magnetic impurity looks like form the point of view of an STM. This work was done by [55], where cobalt atoms where deposited on a Au(111) surface. The LDOS was measured on and off a Co impurity. The results are shown in figure 4.2.

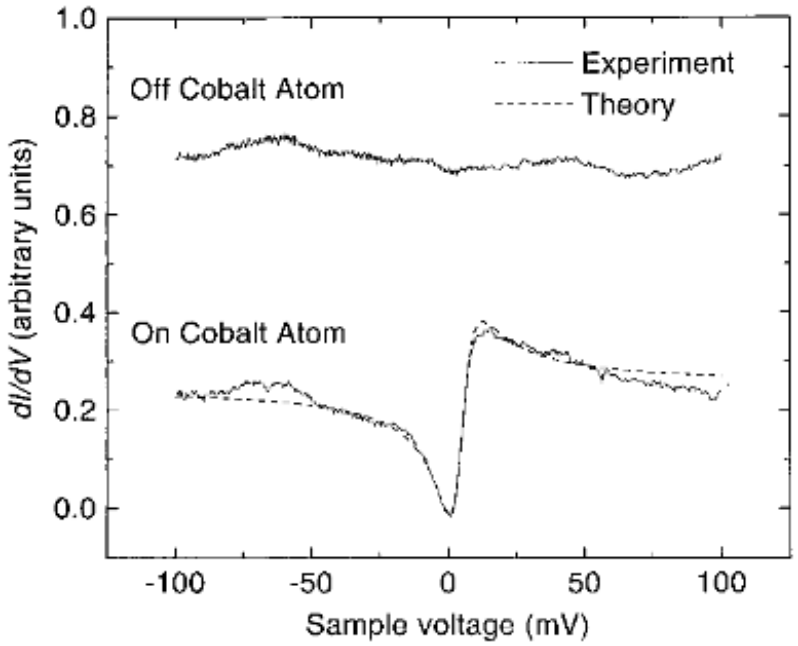

Figure 4.2: The LDOS on a Co atom and off a Co atom from [55]. The spectra off the Co atom shows a flat DOS as expected for a Au(111) surface where the LDOS on the Co atom shows evidence of a Fano resonance.

When measuring the DOS off a Co atom [55] shows a flat density of states (DOS) which is expected. However, on the Co the spectra it is quite different and can be interpreted as a Fano resonance. It is important to note that a Fano resonance is not a DOS effect but rather an interference effect. If there is an impurity state at a particular energy (E_b) sitting on top of a continuum of states (in this case gold which has a flat DOS) it is possible for electrons from the tip to tunnel into the impurity with a tunneling amplitude (t_f) and then into the continuum with

some energy broadening (ν). It is also possible for electrons to tunnel directly into the continuum with an tunneling amplitude (t_c). The ratio of tunneling into the impurity to the continuum is defined as $q= t_f/t_c$. The tunneling scenario is shown schematically in figure 4.2. Clearly since there are two tunneling channels there will be interference effects, these affects where worked out in a different scenario by [56]. Analytically the spectra measured by [55] can be expressed by:

$$\frac{dI}{dV} = R_0 \frac{(q+\frac{\epsilon - E_b}{\nu})^2}{1+(\frac{\epsilon - E_b}{\nu})^2} \tag{4.1}$$

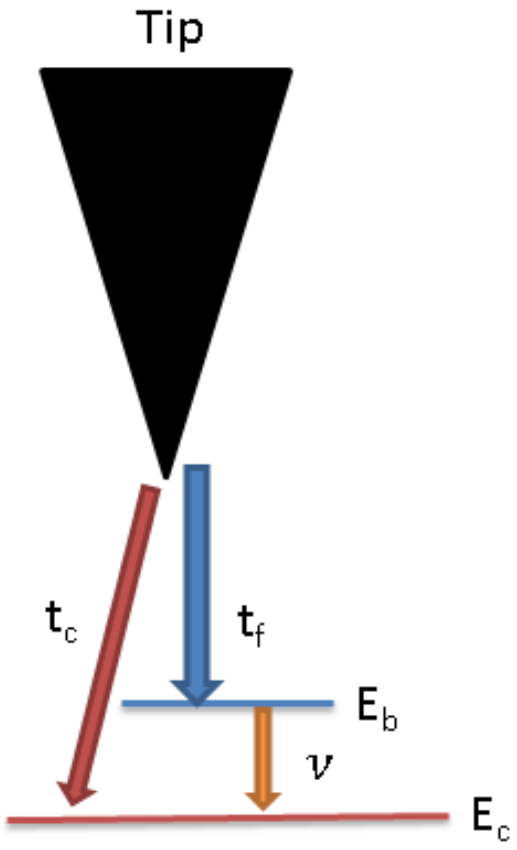

Figure 4.3: Schematic displaying a cotunneling process between tunneling into a continuum (E_c) and an impurity (E_b) where when tunneling into the impurity the electron tunnels through the impurity into the continuum with broadening ν. Where tc represents the tunneling amplitude into the continuum and t_f represents the tunneling amplitude into the impurity.

Where R_0 is just the amplitude and the rest of the parameters were previously explained. In the case of Co atoms ν is related to a local lifetime of the state which can then be related to a Kondo effect since a finite lifetime of the state indicates the presence of a screening cloud. [55] were able to relate the broadening to the local Kondo temperature on each Co atom.

In simple s-wave superconducting systems the Kondo effect is observed to compete with the superconductivity. This competition was recently measured by [52] where a magnetic organic mesh (manganese-phthalocyanine) was placed on top of a superconducting Pb surface. [52] then used SI –STM to measure the LDOS at different locations, their measured spectra is shown in figure 4.4. It is clear that they observe an enhancement of one of the superconducting coherence peaks. This enhancement shift from the electron side (negative bias) to the hole (side) at different locations throughout their surface and it is important to note that the superconducting particle-hole symmetry is broken in these spectra. There is also a location where they observe a zero bias resonance, which is interpreted to be a quantum phase transition.

In order to better understand these results it is necessary to review the fundamental physics of magnetic scattering in a metal. The simplest model one can write down for magenetic scattering is the s-d model [80], the Hamiltonian for this model is given in eq. 4.2.

$$H_{s-d} = -\frac{1}{2N}\sum_{\mathbf{k}\mathbf{k}'} J_{\mathbf{k}*\mathbf{k}'}\left(S^{+}\mathbf{c}^{+}_{\mathbf{k},\downarrow}c_{\mathbf{k}',\uparrow} + S^{-}\mathbf{c}^{+}_{\mathbf{k},\uparrow}c_{\mathbf{k}',\downarrow} + S_z(\mathbf{c}^{+}_{\mathbf{k},\uparrow}c_{\mathbf{k}',\uparrow} - \mathbf{c}^{+}_{\mathbf{k},\downarrow}c_{\mathbf{k},\downarrow})\right) \quad (4.2).$$

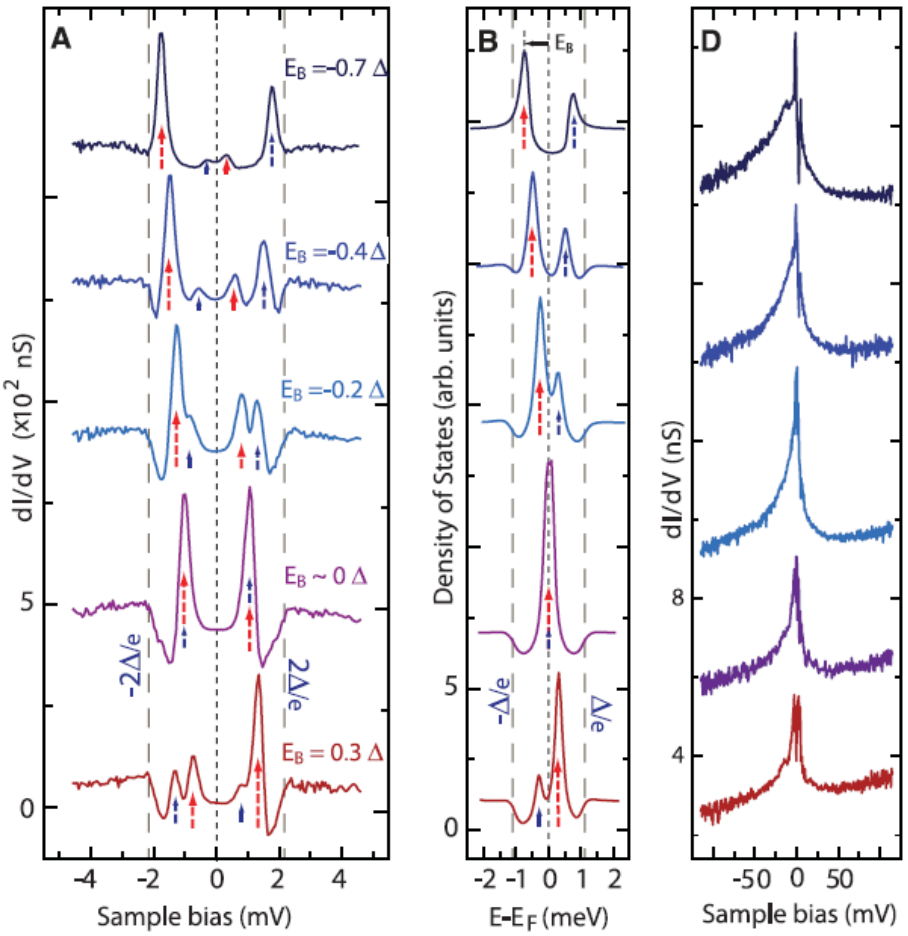

Figure 4.4: A) The measured dI/dV from [52] using superconducting-insulator-superconducting (SIS) tunneling. B) The deconvolved dI/dV spectra measured by [52], this represents the dI/dV of the surface. C) The dI/dV measured at higher energies by [52] indicating a non-particle number conserving asymmetry thought to be a Fano resonance.

Where c(c$^+$) are the fermionic destruction (creation) operators, S_+,S.,S_z are the spin operators, and J is the coupling constant between the conduction electrons and the local moment. Clearly eq 4.2 represents an electron with spin up or down coming into the local moment site where the electron flips its spin opposite the direction of the local moment to screen the spin of the local moment and is then scattered. This process eventually leads to the Kondo effect, in fact is one uses eq. 4.2 to compute the susceptibility of a metal with magnetic impurities one finds the following [80]:

$$\chi(T) = \frac{(g\mu_b)^2 S(S+1)}{3k_b T}\left\{1 - \frac{2J\rho_0}{1+2J\rho_0 \ln\left({}^{k_B T}/_{D}\right)} + c_2(2J\rho_0)^2\right\} \quad (4.3)$$

Where S is the spin quantum number, μ_b is the Bohr constant, k_B is Boltzmann's constant, ρ_0 is the density of states, g =2 for electrons, D is the band width, and T is temperature. It is clear from eq. 4.3 that for the case of J>0 (the antiferromagnetic case) that there is a divergence in the second term of this expansion. The location if this divergence is what has been defined as the Kondo temperature and is given as follows:

$$k_B T_K \sim D e^{\frac{-1}{2J\rho_0}} \quad (4.4).$$

Therefore in order to fully treat the Kondo problem it is not possible to use a peturbative approach, it is necessary to employ a renormalization group approach as was done by [77, 78, 79, 80].

However, we are interested in superconductivity and the Kondo effect. In order to treat both effects a self-consistency t-matrix framework was developed by [57]. From this picture it is clear that the energy of the bound state appears as the enhanced no particle-hole symmetric peak in the spectra which is caused by quantum mechanical interference effects and hence not indicative of the LDOS. Furthermore, [52] was able to increase the energy range of their experiment to reveal a non-particle number conserving asymmetry and by increasing the temperature above the superconducting transition temperature of Pb it was possible to abolish the superconductivity and fit the spectra with a model similar to eq. 4.2. This allowed for the extraction of local Kondo temperature and comparison to [57] self-consistency picture of the Kondo effect with superconductivity. The result is

show in figure 4.5, where there is very good agreement with measurement and theory.

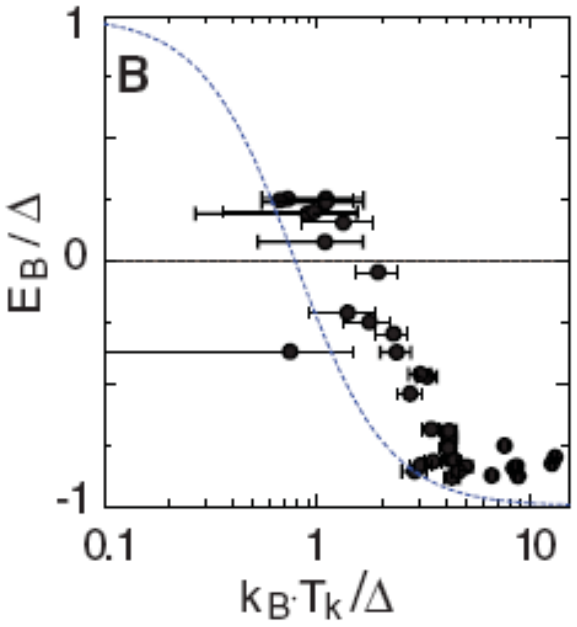

Figure 4.5: Measurements made from [52], represented as black dots, compared to the theoretical model of [57]. The Kondo temperature was a extracted from non-superconducting spectra and the bound state energy was measured as the energy location of the enhanced coherence peak.

This now allows for an explanation of the coherence peak enhancement. The Kondo effect an superconductivity are in direct competition, below some critical value of the coupling constant (J_c) the magnetic impurity can be completely screened and the cooper pair does not have to be broken this leads to the enhanced coherence peak happening on the electron side. Above J_c the impurity cannot be screened completely and the cooper pair must be broken in order to partially screen the impurity which leads to the enhancement of the coherence peak happening in the hole side. At J_c a quantum phase transition occurs which leads to a zero bias resonance.

These types of Kondo like effects have never been observed in a high T_c sample, as previously mention in spite of the fact that Ni has a magnetic moment it behaves as a predominant charge scattering potential. However, the bulk work of [54] shows Fe to be an excellent candidate. So we set out to investigate the effects of Fe impurities in Bi2212.

4.3 Investigation of Fe impurities in Bi2212

The effect on iron impurities in Bi2212 was initially investigated using an optimal doped sample with a Tc=83K and a nominal Fe doping of 0.05%. The initial survey of the sample was intended to identify the spectroscopic signature of the impurities. The signature was identified as a peak appearing on the hole side of the (LDOS) near the edge of the superconducting gap. A topographic image of the 24nmx24nm area of the initial survey is given in figure 4.6a. The corresponding LDOS($\vec{r}$,E) map was taken simultaneously with the topography, an energy layer of the map at 22 meV near the hole side of the superconducting gap is shown in 4.6b. The individual LDOS spectrum for 17 different impurities is given in figure 4.7.

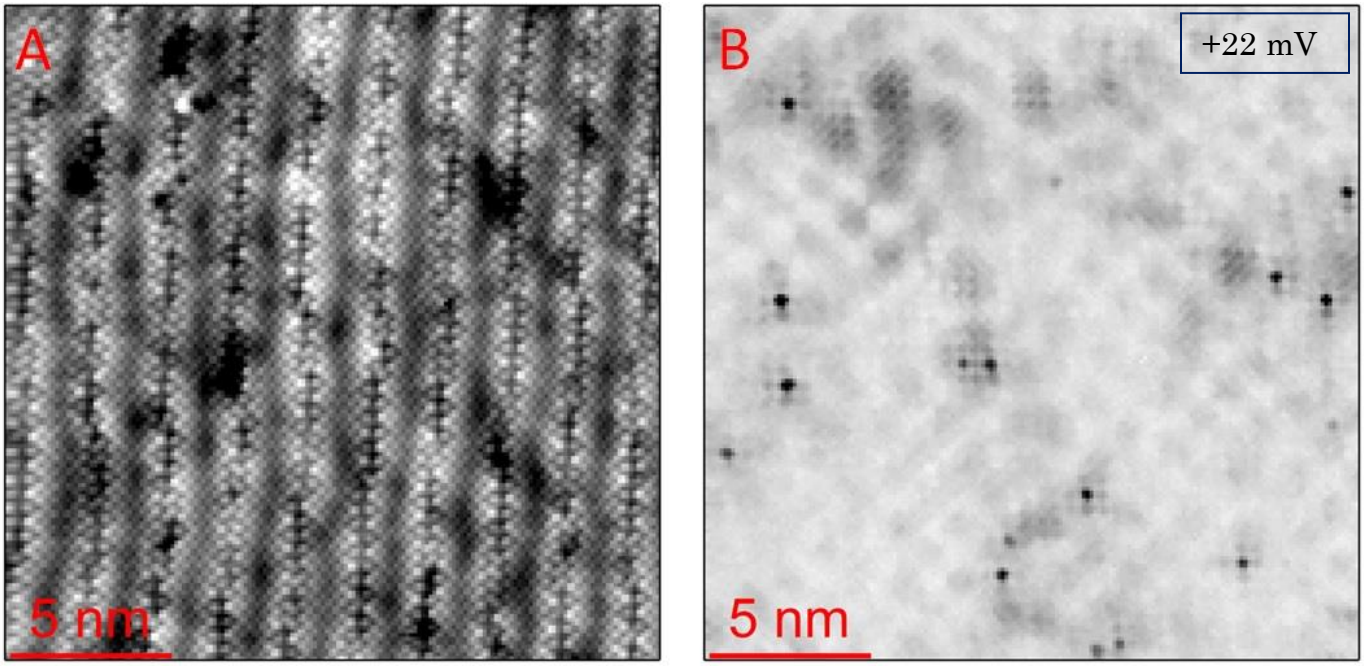

Figure 4.6: A) Topographic image of the intial 24 nm x 24 nm area surveyed on OP83K with a nominal Fe concentration of 0.05% and a set up condition of I=100 pA and V=-100 mV. B) The concurrent LDOS map taken over the same field of view and set up condition displayed at a bias voltage of 22 mV.

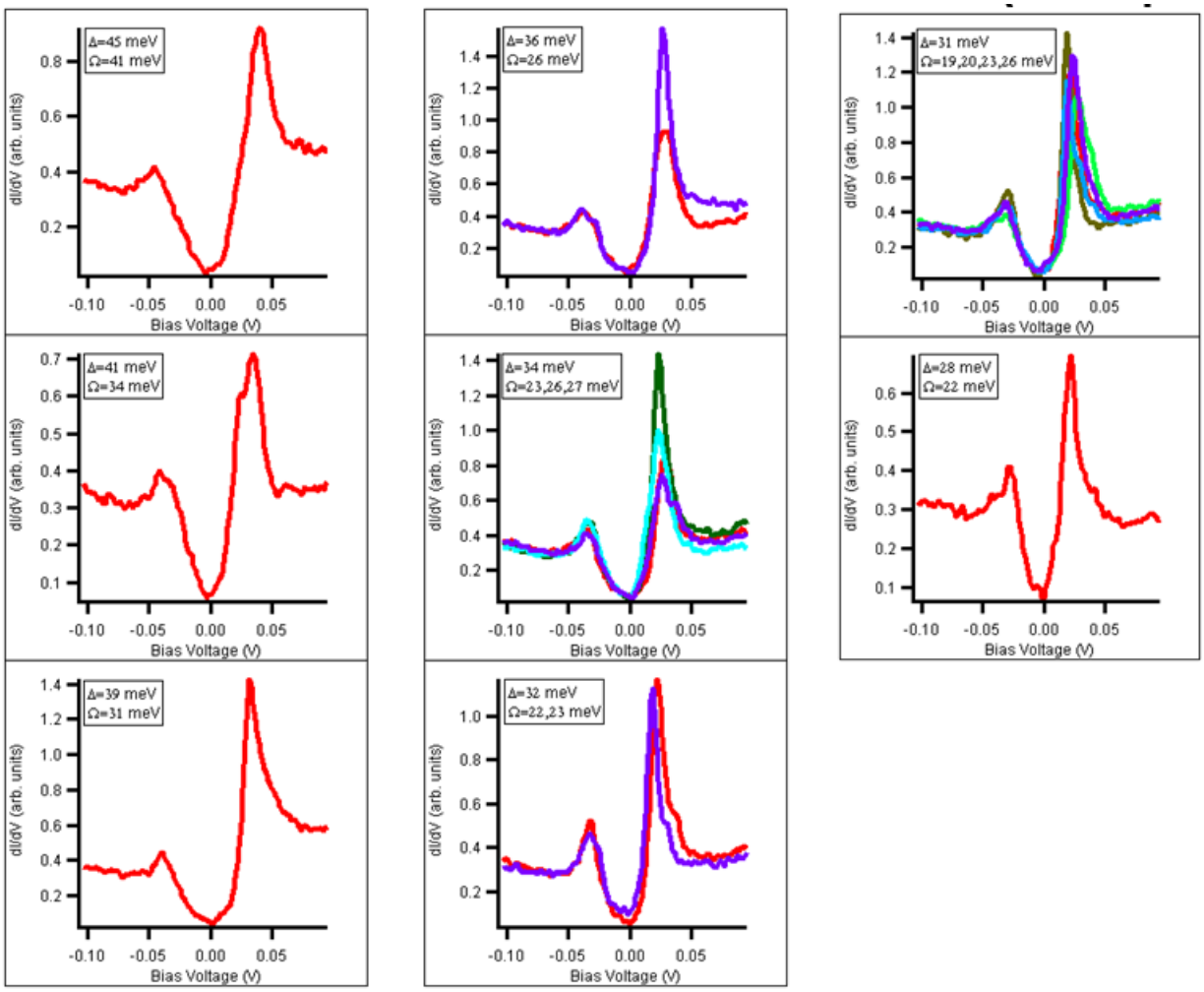

Figure 4.7: Individual spectra on 17 different Fe impurities, note that the energy location of the bound state shifts as a function of gap. The set up condition was I=100 pA and V=-100mV, taken with a 2mV bias modulation, and with an energy resolution of 1.56 mV/point.

There is clearly a lot of variation among the iron impurities. If it is assumed that the enhancement of the hole side is in fact caused by a quasi-bound state[46,58], it is clear that the energy location of the bound state appears to be moving relative to the gap edge measured on the electron side. To further investigate the impurities it was necessary to make sure that all the impurities were located, the fact that the bound state occurs near the edge of the gap makes the identification of the impurities difficult. In order to distinguish the Fe atoms

location from the non Fe atom location one can take advantage of the fact that there is a huge asymmetry between the electron and hole side of the LDOS. In typical non Fe doped Bi2212 the electron side of the LDOS is higher than the hole side of the LDOS due to the back ground asymmetry caused by the tunneling process [59]. This scenario is reversed for Cu sites that have been replaced with Fe atoms. Therefore computation of the following quantity $K(\vec{r}) = LDOS(\vec{r},\Omega)/LDOS(\vec{r},\Delta)$, where Ω is the energy location of the peak on the hole side of the LDOS and Δ is the location of the peak on the electron side of the LDOS, should give the Fe atoms site a clear spectroscopic signature. Figure 4.8 shows the calculated $K(\vec{r})$ for the 25 nm x25 nm area of figure 1A, the Fe atoms are clearly visible as they show up as bright peaks in the FOV. There were 17 impurities located using this method, hence we measure an Fe doping of 0.42 +/- 0.10 %, consistent with the nominal doping of 0.5%.

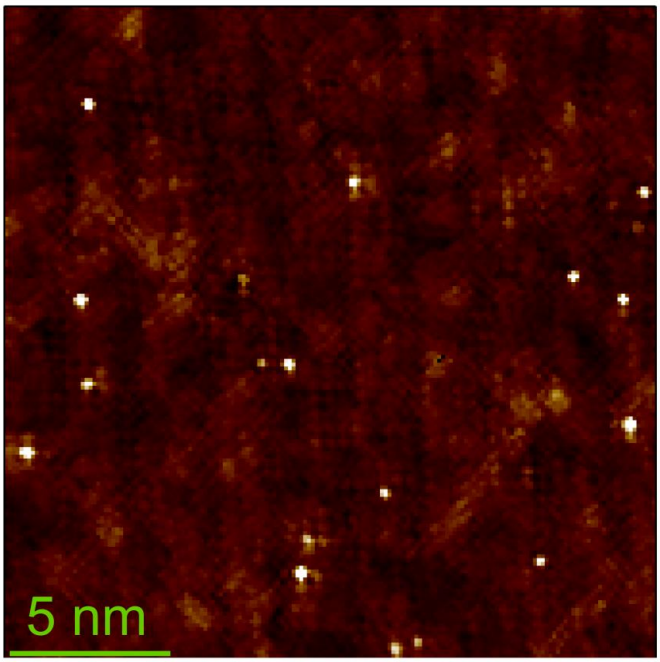

Figure 4.8: $K(\vec{r})$ for the FOV in figure 1A, the bright white spots represent the signature of an Fe impurity.

Following the identification of the Fe atoms, the relationship between the bound state and the gap edge was investigated. This was accomplished by taking the individual spectra shown in figure 4.7 and finding the location of the peak on the hole side (Ω) and the location of the peak on the electron side (Δ). This data was combined with a second set of data taken with lower tip resolution on a separate sample of OP83K with 0.5% nominal Fe doping whose results is summarized in figures 4.9 a-c. The combination of the two data sets was used to detect a correlation between gaps and bound state energy. This is shown in figure 4.10. It is important to note that that the Fe atoms are highly localized and their spatial resolution is very sensitive to the sharpness of the tip, it easy to see when comparing figure 4.6B to figure 4.9B that the dull tip can hide some of the spatial richness of the Fe impurities. Figure 4.10 clearly shows a correlation between gap and bound state. The peaks used for creating figure 4.10 were found using IGOR's peak finding algorithm which uses a numerical second derivative technique to find the maximum in each spectra.

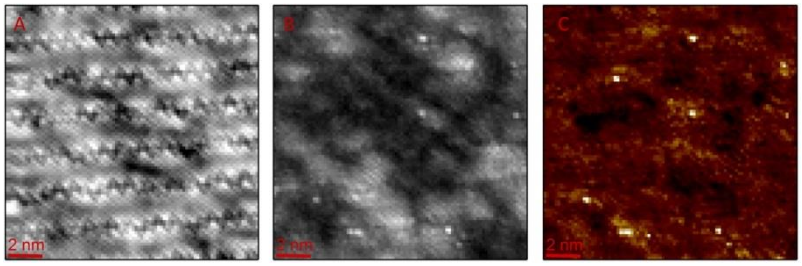

Figure 4.9: A) Topograph of a 15 nm x 15 nm FOV taken with I= 100 pA and V=-100 mV. B) LDOS map taken concurrently with figure A, with an energy layer of 22.5 mV dispayed. C) Computed $K(\vec{r})$ for the FOV shown in figure A.

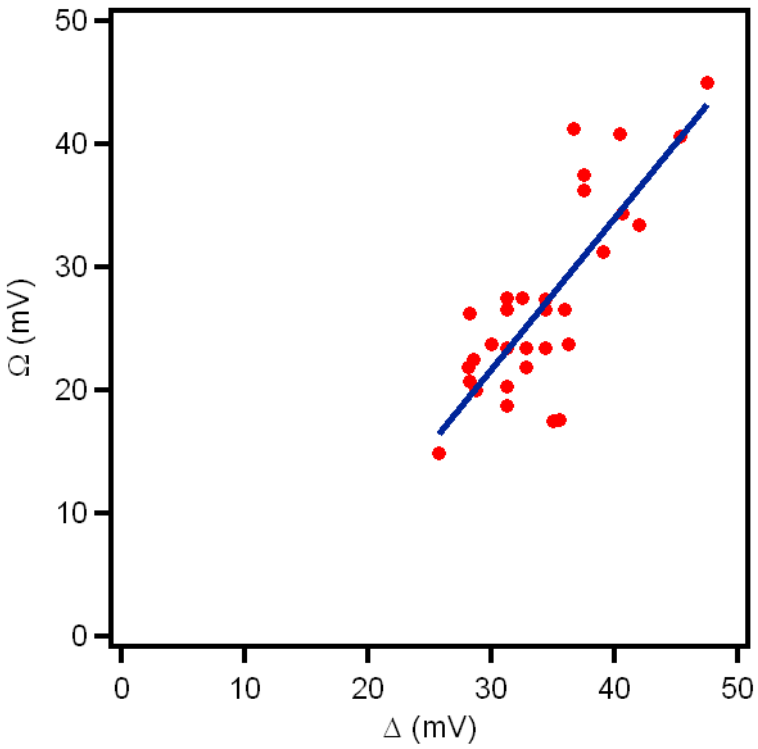

Figure 4.10: The relationship between the electron peak (Δ) and the bound state peak (Ω). The data is combined from the FOV's shown in figure 1 and figure 4. The fitted line gives a slope of 1.2 with and intercept of -15.2 mV.

In order to further model the relationship, a line was fitted to the data as shown in figure 4.10. The regression line indicated a slope of 1.2 with an x intercept of -15.2 mV. This behavior helps to explain some of the variation on Fe sites observed in figure 4.7 and in all of the Iron samples. Bi2212 is inherently a disordered material, and as previously observed in dozens of other STM experiments [14, 15, 81, 82, 83] shows a large spatial gap inhomogeneity. This is of course not expected from the point of view of a simple BCS superconductor where the gap should be homogenous throughout the material. The source of the gap inhomogeneity has been debated vigorously over the past decade, but recently it has been discovered that this effect is due to local doping [15,16]. Hence, when STM

images a Bi2212 surface it is actually imaging various Fermi surfaces, this implies that the carrier concentration varies spatially on a BSCCO surface on the order of a coherence length. Therefore, with in this picture it is expected that the local coupling of the magnetic moment of the Fe impurities to the conduction electrons (J) will vary spatially. This is a likely explanation to figure 4.10 where a higher gap is representative of a more underdoped sample and a lower gap is representative of a more overdoped sample. From experiments done on s-wave superconductors [52,53] it is known that there exists some critical J for which the asymmetry shifts from the hole side to the electron side, the data from figure 4.10 seems to suggests that the critical J in Bi2212 with Fe impurities occurs at a gap size of ~13 mV which would correspond to a severely overdoped sample.

4.4 Interplay of Fe atoms with Superconductivity

With an understanding of the signature of the bound state, it is possible to investigate the effect of the impurities on the superconductivity. In order to accomplish this, a larger FOV of 50 nm x 50 nm was used, this also allowed for an investigation of QPI as well. The topograph of the FOV used to investigate the effect of the impurities on the gap is given in figure 4.11a. The LDOS was mapped spatially and a layer at energy of 23.3 mV is shown in figure 4.11b. As previously discussed using the LDOS map to find all the Fe atoms is not optimal, therefore the quantity $K(\vec{r})$ was computed for the FOV and is displayed in figure 4.11d this yielded an Fe doping of 0.46 +/- 0.05%.

With all the Fe atoms located, it was possible to create a mask to find the average LDOS excluding the Fe atoms and compare it to the LDOS on the Fe atom sites. The result is displayed in figure 4.11c. If the peak on the electron side of the Fe LDOS is interpreted as the superconducting gap energy [46,57,61,62] then it is clear from figure 4.11c that the Fe impurities are decreasing the size of the superconducting gap. In previous work on Zn and Ni it was found that the impurities tended to lie in areas of smaller gap but it was not possible to distinguish whether this due to the impurities preferentially selecting areas with lower gap or whether the impurities were lowering the gap[63].

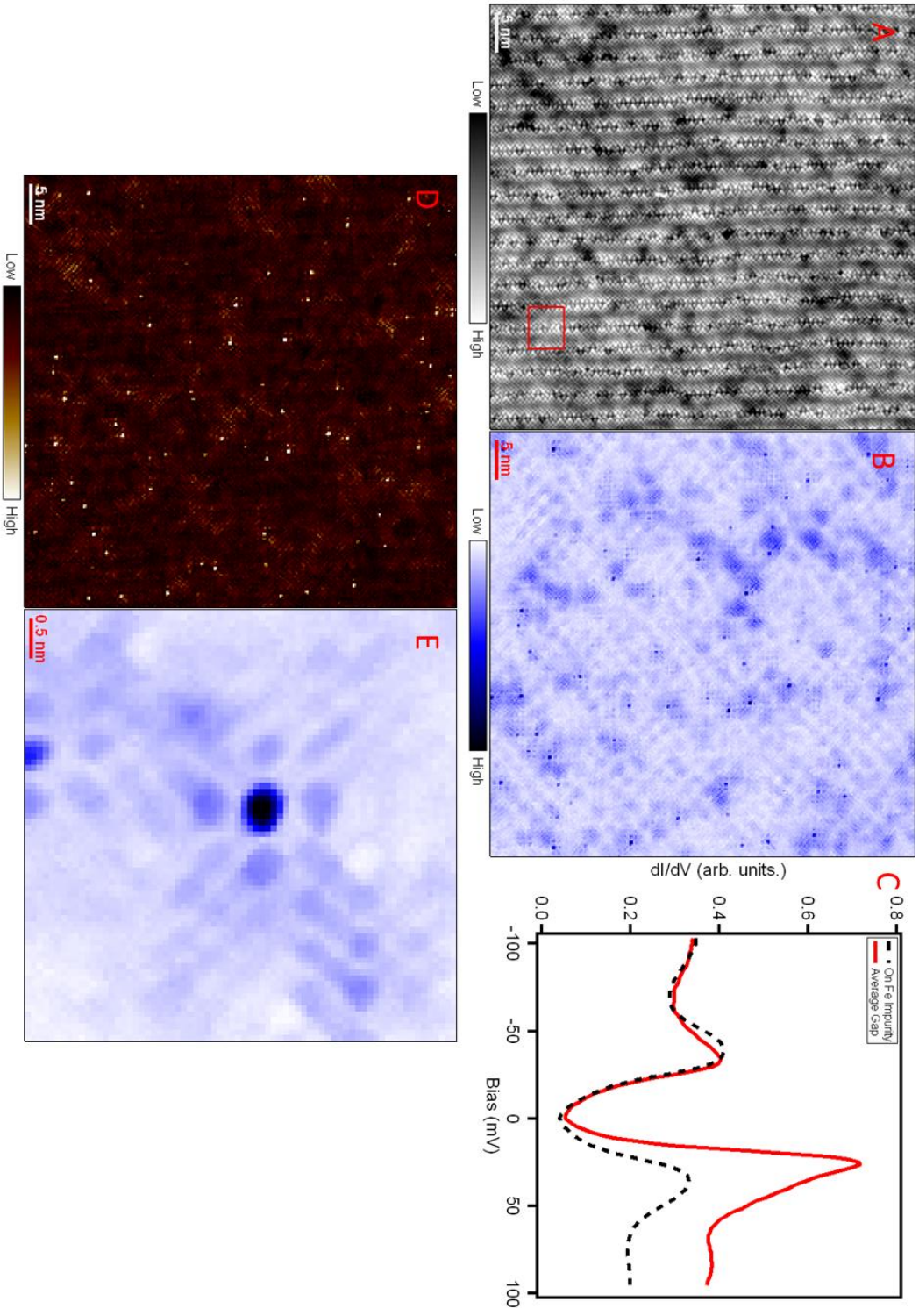

Figure 4.11: A) Topograph of the 50 nm x 50 nm FOV of OP83K with nominal 0.05% Fe doping. B) he concurrent LDOS map taken over the same field of view displayed at a bias voltage of 23.3 mV. C) The dashed lines represent the LDOS over the entire FOV excluding the Fe atoms. The solid line represents the LDOS on the Fe atoms averaged over every Fe atom in the FOV. D) The computed $K(\vec{r})$in the FOV, the bright white spots represent Fe impurities. E) A small FOV taken around the red box in figure 7A showing the spatial structure of a typical Fe impurity.

In order to investigate this effect further, a gap map was computed by finding the location in energy of the LDOS peak on the electron side, since the hole side peak is influenced by the Fe impurities. The gap map is displayed in figure 4.12 with the location of the Fe atoms indicated by the white circles.

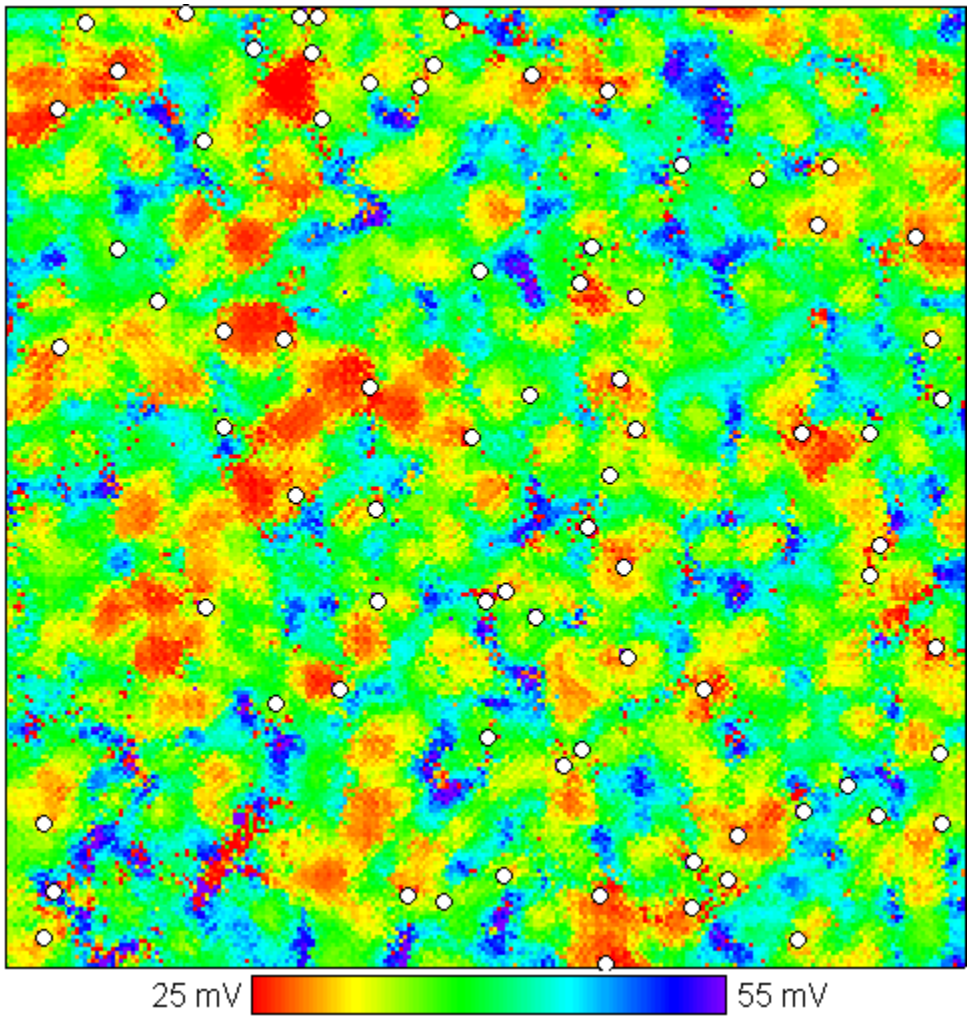

Figure 4.12: Gap map of the FOV shown in figure 7a, where the white circles represent the location of Fe impurities.

With the location of the Fe atoms known it is possible to compute the average gap at successive distances away from the Fe sites. This was done by generating a circular mask of around each Fe impurity and computing the average gap. The

distance of the circular mask from the impurity site was successively increased to find the average gap size as a function of distance from the impurity site. The result is displayed in figure 4.13 and suggests that the gap seems to decrease on the order of a coherence length. While this analysis suggest that the Fe impurities decrease the superconducting gap it does not give information as to whether this behavior is occurring due to the Fe impurities preferring sites with low gap regions or if the Fe impurities due in fact lower the superconducting gap.

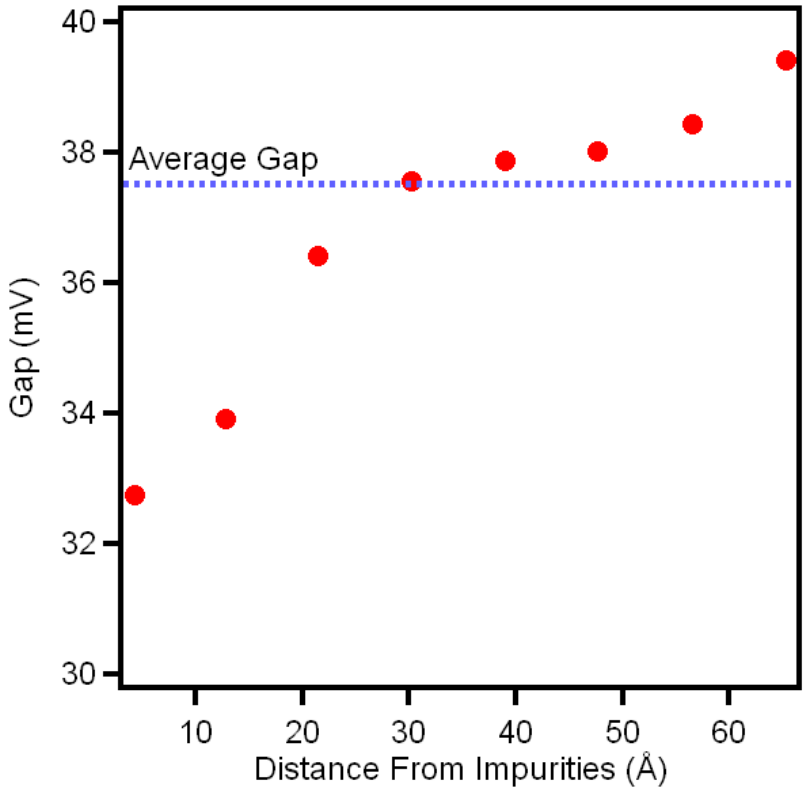

Figure 4.13: The average gap a as a function of distance from the Fe impurity site. This was computed by taking a circular mask around each Fe impurity and successively increasing the distance from the impurity site.

The Fe doped samples were initially grown as optimally doped samples with a Tc=91K (OP91K) and then had Fe substituted for Cu [84]. Therefore, in theory it is possible to compare the gap distribution of an OP91K sample to that of an Fe

doped sample. This analysis does not work very well due to the fact that there is enough disorder in Bi2212 to potentially bring into question any result learned from this line of reasoning. However, recent results [15,16] indicate that scaling the gap distributions by the average gap reveals that the gap distributions are identical across doping and in samples with Zn and Ni impurities. This was done for an OP91K sample whose gap map is displayed in figure 4.14 and the distribution was compared to that of the gap map from figure 4.12, the results are shown in figure 4.15. Figure 4.15 clearly shows that the Fe doped sample gap distribution contains a skew; this skew is not observed with other impurities such as Zn and Ni. This suggests that the Fe impurities do in fact lower the superconducting gap. If the impurities are removed from the FOV by applying a mask that sets the gap to 0 in a radius of one coherence length around the Fe impurities the histogram reveals the expected distribution for a non Fe doped Bi2212 sample, this is shown in figure 4.16. This is the first observation of impurities lowering the superconducting gap in Bi2212.

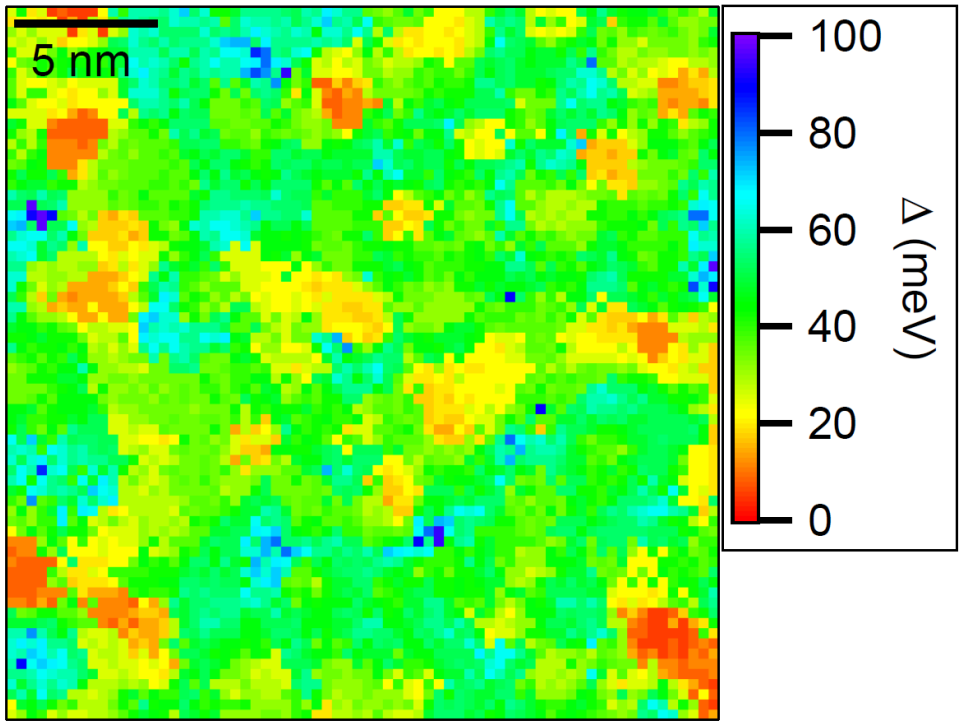

Figure 4.14: Gap map of a 24nm x 24nm FOV on an OP91K sample. Taken with set up conditions of I_{set}=200 pA and V_{bias}=-200 mV.

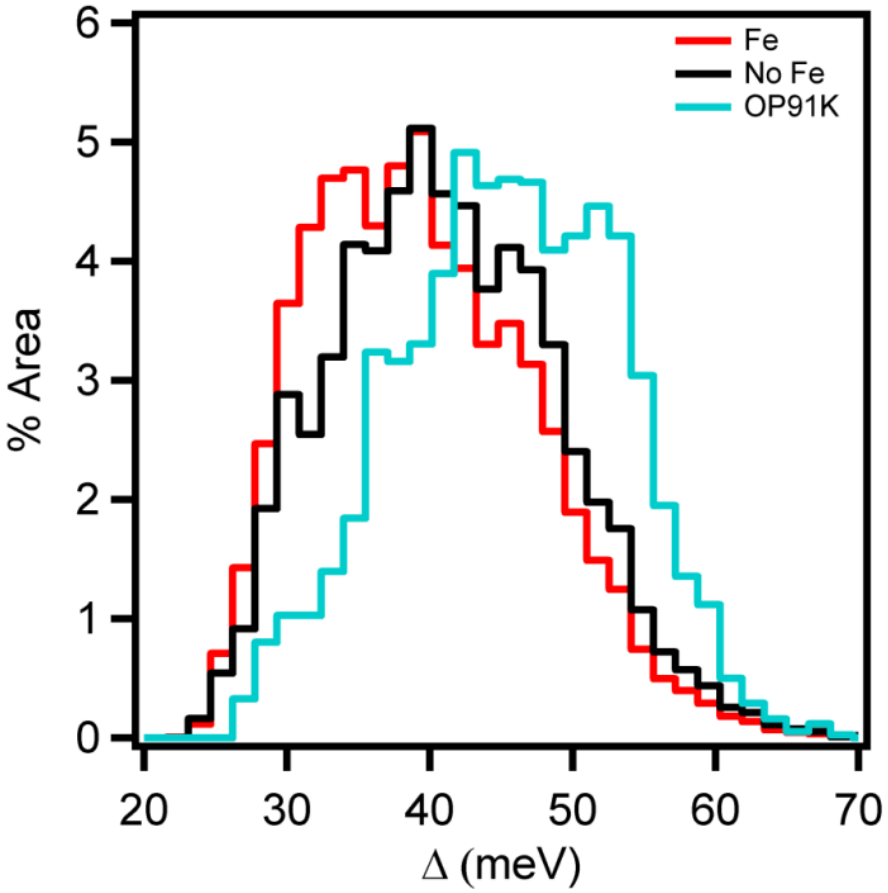

Figure 4.15: Comparison of gap distributions between the OP91K sample shown in figure 4.13 with the Fe doped sample shown in figure 4.11. The OP 91K sample is displayed in blue, the Fe doped sample is displayed in red, and the Fe doped sample with the Fe atoms artificially removed is displayed in black.

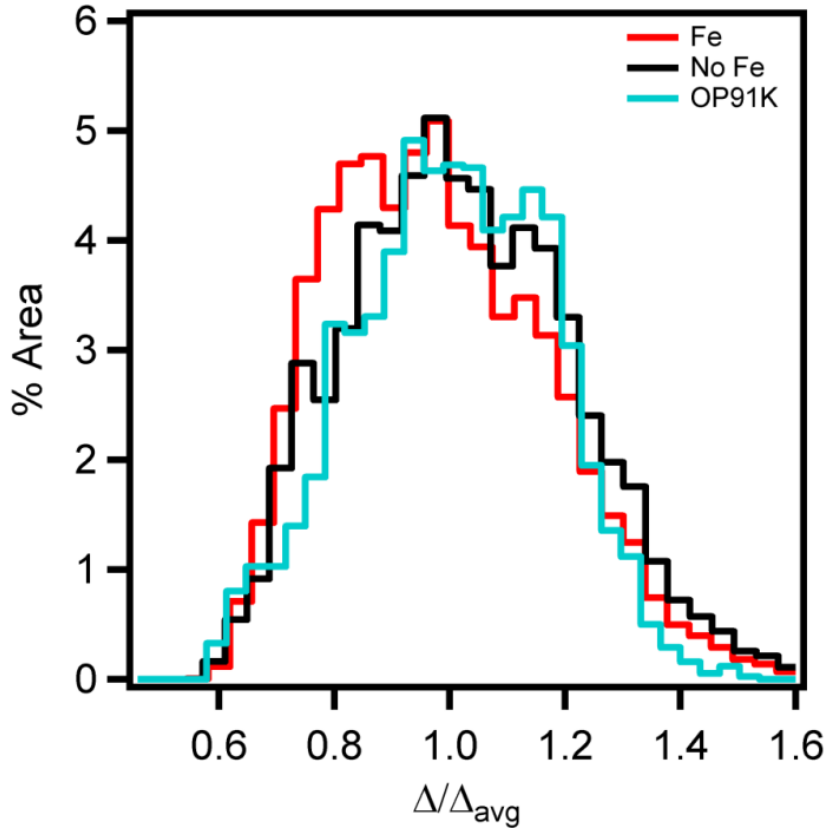

Figure 4.16: The gap distribution of the optimally doped Fe doped sample (displayed in black) with the gap set to zero around the Fe impurities with a 1 coherence length radius compared with the gap distribution of a no Fe doped OP91K sample(blue). Both distributions have been scaled by the average gap.

4.5 Understanding the Spatial Structure

An investigation into the spatial structure of the impurities was then conducted. Previous work on Ni and Zn [22,23] indicated that the impurity sites should have a particular structure. This shape is due to the fact that upon cleaving it is not the CuO layer that is exposed but rather the BiO layer. Therefore, electrons are transferred from the conduction plane to the tip via a particular combination of atomic orbitals. This provides a "filter" which yields the shape seen in Ni and Zn

[46]. Four different Fe impurities with different gap and bound state energy were individually imaged and are displayed in figure 4.17 A-H.

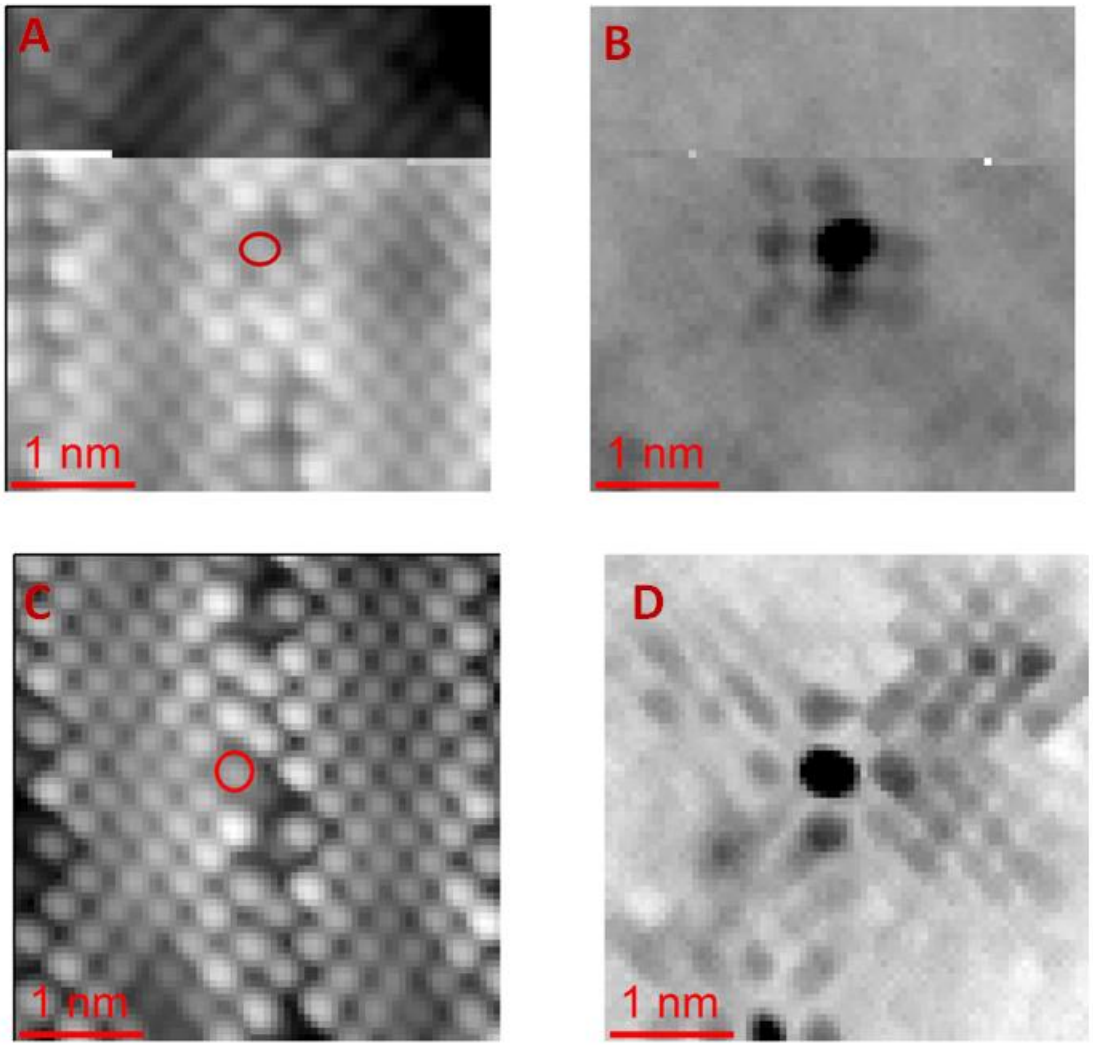

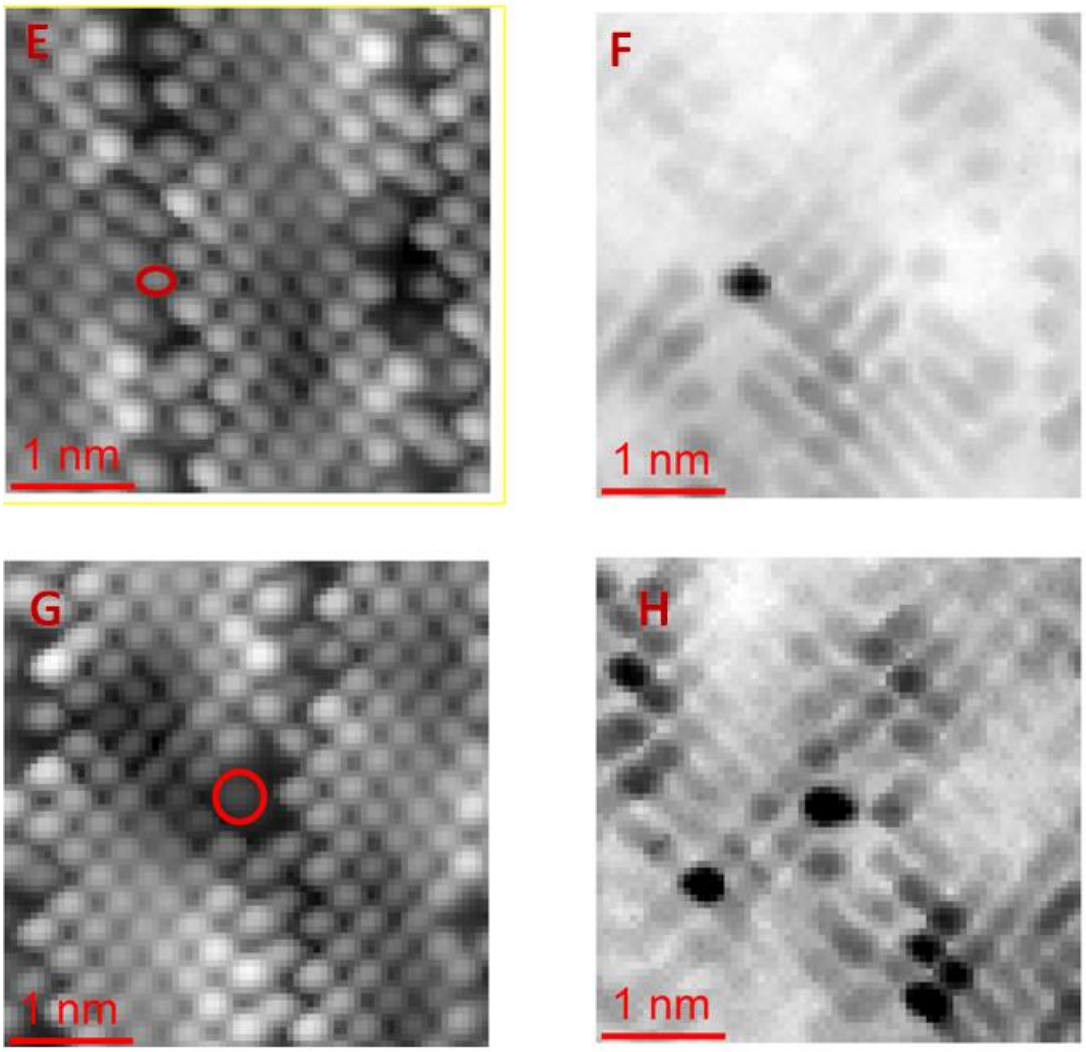

Figure 4.17: Topographic image and LDOS($\vec{r}$, E) of 4 different Fe impurities. The LDOS are given at energy Ω and the impurity is indicated in the topograph by a red circle. A-B) Δ=34.4 mV, Ω=20.3 mV C-D) Δ=31.3 mV, Ω=21.8 mV E-F) Δ=29.7 mV, Ω=25 mV, G-H) Δ=37.5 mV, Ω=40.6 mV.

The spatial structure is equivalent to that seen in Zn and Ni, however the intensity of the LDOS on the next nearest neighbor site seems to be smaller than in the previously reported impurities studied in Bi2212.

To further characterize the spatial nature of the quasi bound state formed by the Fe impurities line cuts were along axis of high symmetry through the impurity. In particular line cuts were taken along the direction of the nearest neighbors (Γ-X)

and next nearest neighbors (Γ-M). The line cuts for the three impurities shown in figures 4.17e, 4.17f, and 4.17h are displayed in figure 4.18a-b, 14.18c-d, and 4.18e-f. Clearly the impurity shows up as a high intensity point on the line cuts. These line cuts also reveal the spectroscopic signature of the electron side of the Fe impurities as demonstrated in figure 4.19, this signature is consistent with what has previously been observed in Ni and Fe and is predicted from the hopping matrix element. However, without the line cuts it would be extremely difficult to find due to its low intensity in the LDOS map.

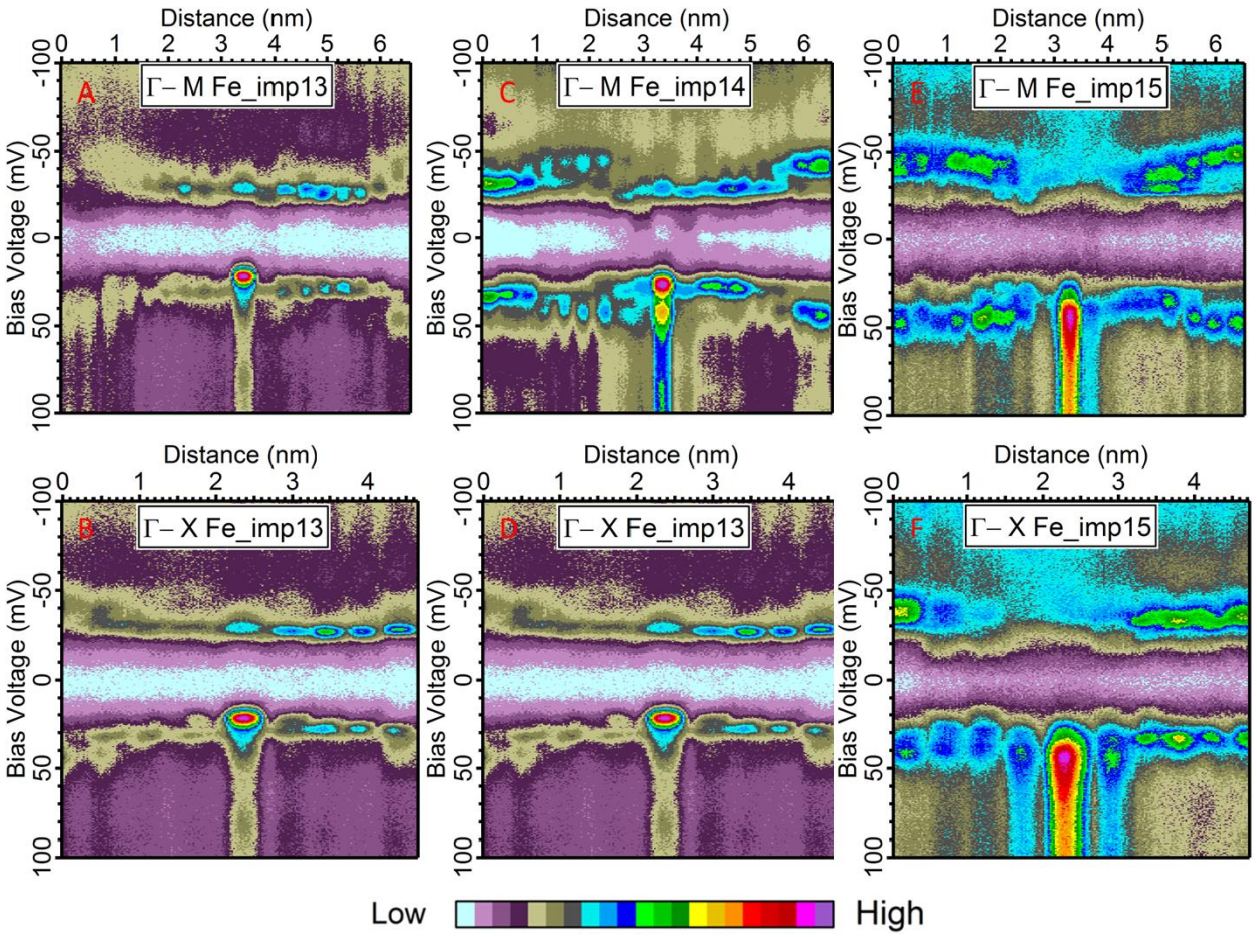

Figure 4.18: Line cuts taken across high symmetry directions for figures 4.17 d,h,f. The bright red spot indicates the location of the Fe atom.

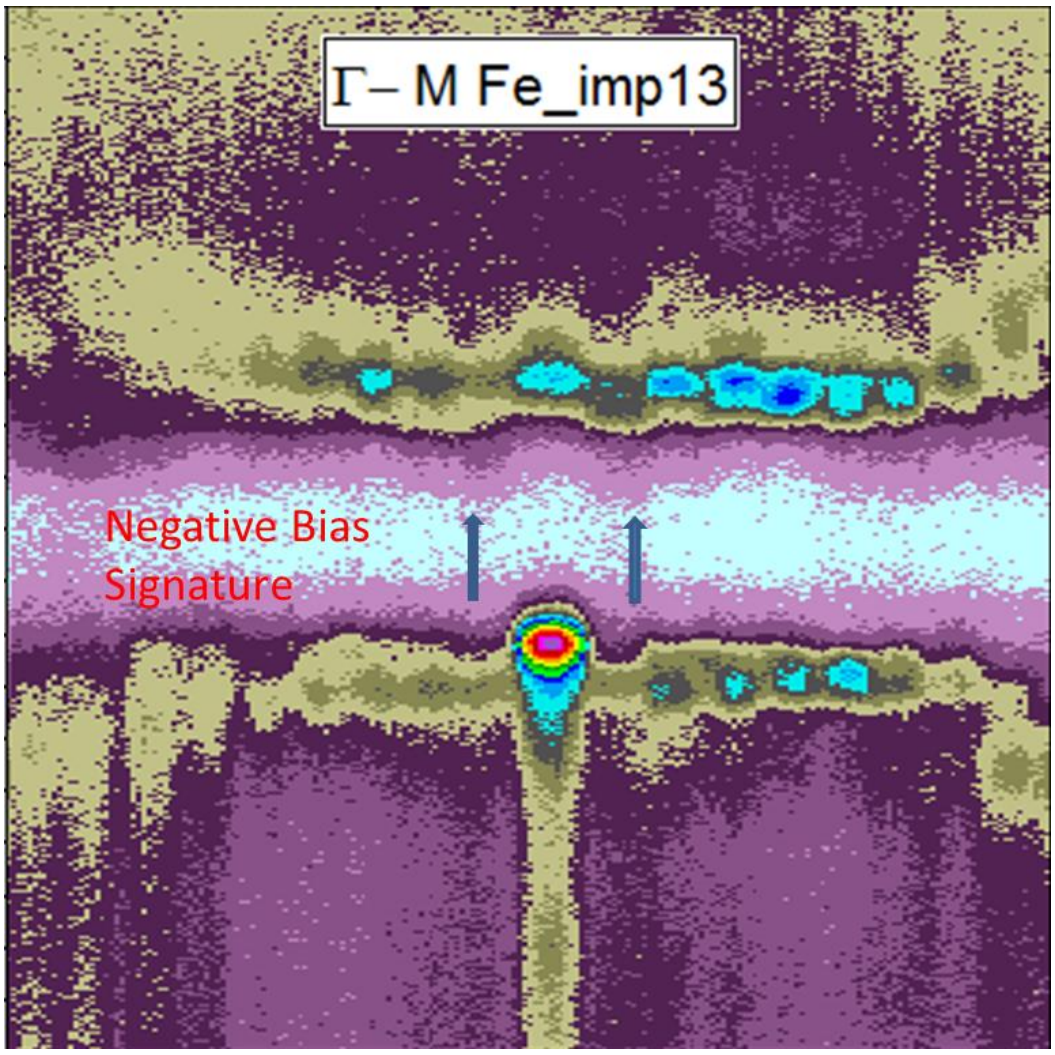

Figure 4.19: The line cute from figure 15a with arrows indicating the spatial spectroscopic signature of the Fe impurity.

The line cuts also allow the study of spatial variations of the LDOS at constant energy with extremely high spatial resolution (~40 pm). A spatial cut at the impurity energy reveals that the LDOS shows a spatial modulation along the direction of the next nearest neighbors, as shown in figures 4.20a, 4.20b, and 4.20c. This modulation is absent along the direction of the nearest neighbor as shown in figures 4.21a, 4.21b, and 4.21c. As is obvious from figure 4.20 a-b the LDOS modulation seems to decay as a function of distance away from the impurity, this is

less obvious 4.20 c because there is another impurity 3 atoms away, hence it is possible that the second impurity could be altering the patterns observed in figure 4.20 a-b.

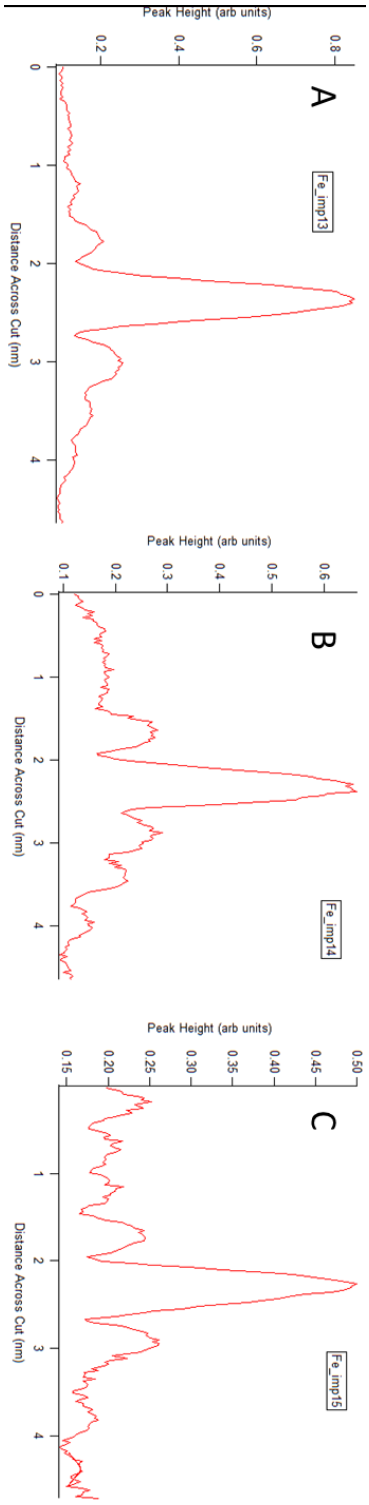

Figure 4.20: Amplitude of the LDOS taken at the energy of the impurity along the direction of the next nearest neighbor. A) Cut taken from figure 4.18 a. B) Cut taken from figure 4.18 c. C) Cut taken from figure 4.18 e.

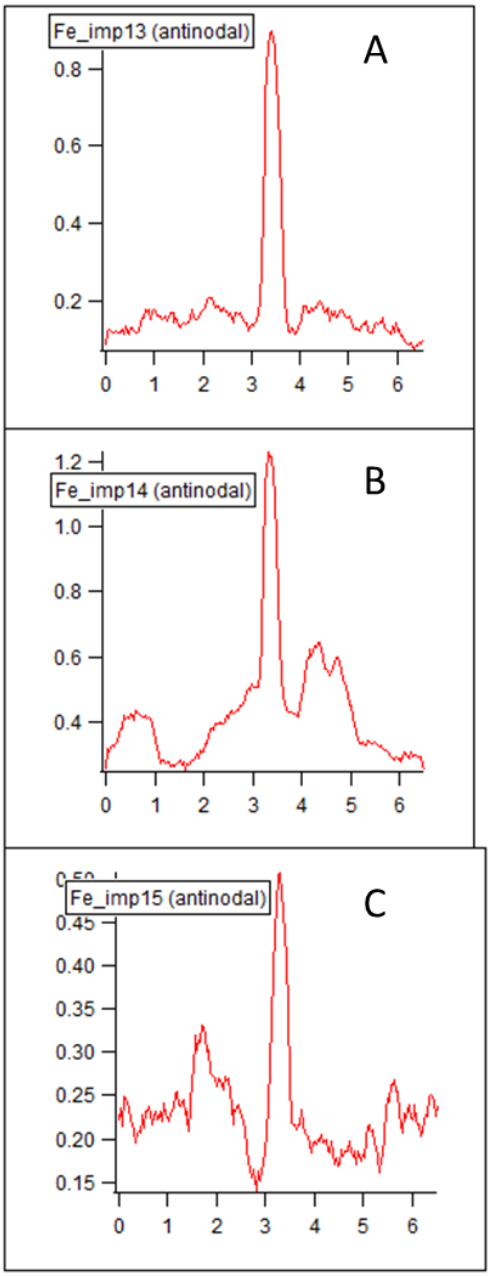

Figure 4.21: Amplitude of the LDOS taken at the energy of the impurity along the direction of the nearest neighbor. A) Cut taken from figure 4.18 a. B) Cut taken from figure 4.18 c. C) Cut taken from figure 4.18 e.

In an attempt to model the modulation, the height of the peak along with the distance it occurs from the impurity was found. This data seemed to indicate that the peak location was rapidly decreasing as a distance from the impurity with some

characteristic length scale. In order to attempt to extract the length scale an exponential function of the form $y_0 + Ae^{-r/\tau}$ was used to fit the data, the results are shown in figures 4.22 a-c. Immediately a characteristic length scale of ~2.5 nm emerges from the fits of figure 4.22 a and 4.22 b, however this length scale is not present in figure 4.22 c where the fit yields a length scale of 1.9 nm. The disagreement between the fits of figure 4.22 a and b with 4.22 c could be due to the second impurity in the vicinity of figure 4.18 h. There are other problems that arise, because the length scale is so short the LDOS modulation only appears to exist through 2-3 oscillations which means that a small number of data points are used for the fitting. Also, because the state resides close to the edge of the super conducting gap it is possible that coherence peaks in the vicinity might bias or hide the oscillations. However, the length scale extracted from the fits (~2 nm) seems to agree with the length scale from figure 4.13 which showed that the gap decreases on roughly the same length scale, this is suggestive of two competing effects. Whatever causes the LDOS modulation might also cause the superconducting gap to decrease, however once the modulation vanishes the gap seems to be able to rebound. Such an effect has never been reported in Bi2212.

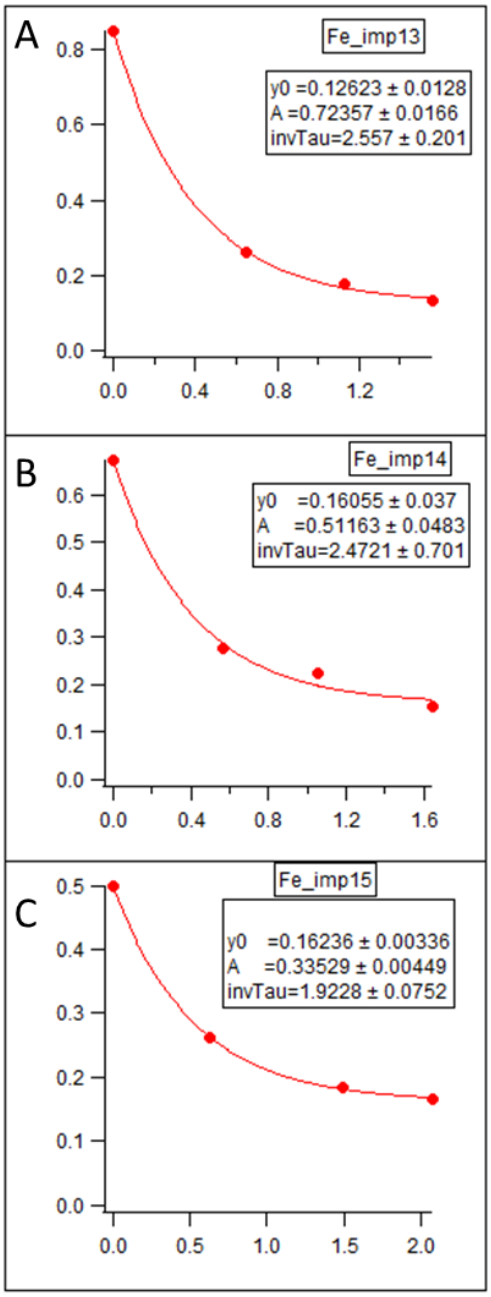

Figure 4.22: Peak height extracted from figures 17 a-c plotted against distance from the Fe impurity. A) Peak height from 4.18 a. B) Peak height from 4.18 c. C) Peak height from figure 4.18 e.

4.6 Zero Bias Enhancement

The superconductivity density of states can be modeled by the following formula discovered by [85]:

$$\mathrm{DOS(E)} = \mathrm{Re}\left[\int_{\vec{k}} \frac{(E+i\Gamma)d^2\vec{k}}{\sqrt{(E+i\Gamma)^2-\Delta(\vec{k})^2}}\right] \quad (4.5).$$

Where Γ is an energy broadening term that has been introduced to account for the lifetime of the quasiparticles. Recently Bi2212 spectra has been fit with an extension of this model where $\Gamma \longrightarrow \Gamma_0 + \alpha E$ by [86]. Among the discoveries, was the conclusion that a zero bias enhancement in the $\mathrm{LDOS}(\vec{r}, 0\ \mathrm{mV})$ was indicative of a decrease in quasiparticle lifetimes.

A recent ARPES experiment on Fe doped Bi2212 [87] indicates that introducing Fe into Bi2212 reduces the lifetimes of the quasiparticles near the nodal direction. In order to study these effects locally the $LDOS(\vec{r}, E)$ of an individual Fe atom was imaged over a 5 nm x 5 nm FoV and fitted with Eq. 4.5, the resulted fitted Γ is displayed in figure 4.23. We observe no local increase in the Γ near or at the impurity site when using Eq. 4.5, an increase in Γ would signify a decrease in quasiparticle lifetime. Furthermore, the data from [87] indicates that there should be no change in the superconducting gap of an Fe doped sample (i.e. the gap between a non Fe sample and an Fe doped sample is the same), however our STM data indicates that the gap has decreased by 5% in a 0.5% Fe doped sample vs. the non Fe doped sample. The gap decreasing is consistent with magnetic impurities, which have been known to have a strong effect on the gap of s-wave superconductors.

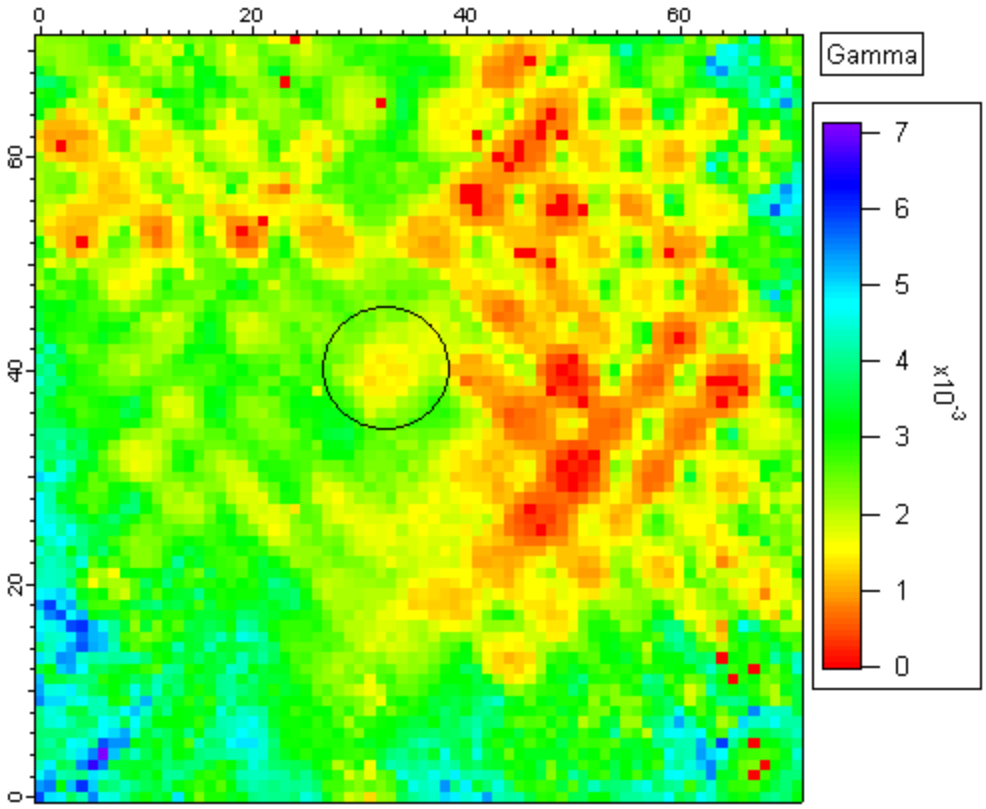

Figure 4.23: Spatially variance of Γ from Eq. 4.5. The black circle indicates the location of te Fe atom. The data shows no significant decrease in quasiparticle lifetime near the Fe impurity.

While, we observe no increase in Γ using Eq. 4.5 if the raw LDOS($\vec{r}$, 0 mV) is measured we observe clear spectral weight at zero bias on impurity sites. The zero bias layer over a 24 nm x 24 nm FoV is shown in figure 4.24. While the increased zero bias could be interpreted as a local on-site decrease of quaisparticle lifetime, as we shall see in the next section the onsite spectra is not a measure of the LDOS. The lack of reconciliation between ARPES and STM is as of date not understood. One possibility is that Fe impurities lower the gap one the order of a coherence length, hence this lower of the gap might be biasing the fittings.

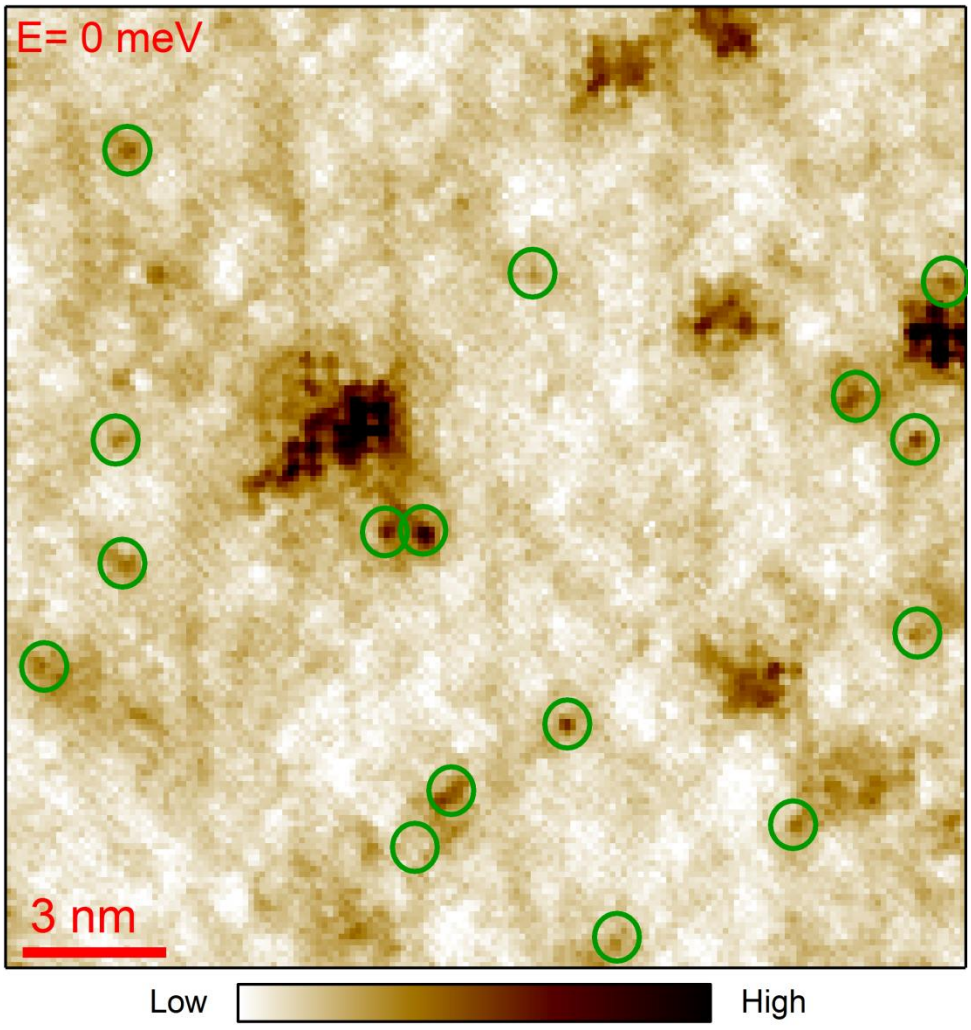

Figure 4.24: Zero Bias layer of a 24nm x 24 nm field of view. The green circles indicate the location of Fe impurities and the red circles indicated the location of native Cu vacancies. Zero bias conductance is enhanced but details depend on particular impurity.

4.7 Understanding the Spectra

It is clear from figure 4.7 that there is a non-particle number conserving asymmetry which is common to all Fe impurity sites. This asymmetry is caused by tunneling through a Kondo resonance [55,64]. This can be understood from a Fano resonance frame work as explained in section 4.2, where a continuum of states exists and there is a secondary level available for tunneling. If it is possible to

tunnel through the secondary level into the continuum, with some finite life time, and tunnel directly into the continuum, it was shown by [56] that the tunneling spectra will have a pronounced asymmetry due to interference effects of the two tunneling processes. However, it is clear that the spectra shown in figure 4.6 cannot be described by the model from [56]. This is due to the fact in the derivation of the model from [56] assumes a flat density of states for the continuum, but Bi2212 has a d-wave density of states therefore one would not expect a model with a flat density of states to be sufficient.

Tunneling through Kondo resonances is not restricted to substrates with a dilute concentration of magnetic impurities. Recently, [65] used SI-STM to image a Kondo lattice (where Konodo resonances exist at each lattice site) on URu_2Si_2. This so called heavy fermion material does not possess a simple density of states therefore the spectral features cannot be properly described by the model from [56]. Theoretical studies by [66] have used the Fano framework to develop a model that describes the tunneling spectra for a Kondo resonance where the continuum is allowed to have a more complicated DOS. This can be accomplished within a theoretical framework where a local spin-conduction electron composite is formed (local spin compensation) and that this composite hybridizes with the conduction electrons which lead to the observed resonance., the green function that results is as follows:

$$G(\epsilon) = \frac{(t_c i\pi\rho\upsilon + t_f)^2}{\epsilon - E_b - i\pi\rho(\epsilon)\upsilon^2} + it_c{}^2\pi\rho(\epsilon) \tag{4.6}$$

Where p is the desity of states of the material in question(the model was initially applied to heavy fermions) and the other parameters have been explained in section 4.2. The model can easily be extended for a d-wave DOS. However, Bi2212 represents a unique experimental challenge, in that SI-STM studies have shown that the local gap varies by as much as a factor of 2 on ~30 nm length scales. Therefore, the use of a local probe with atomic resolution is mandatory in order to measure the local DOS in the vicinity of an Fe impurity.

Using the fact that $\frac{dI}{dV} \propto \frac{-1}{\pi} \mathrm{Im}[G(\epsilon)]$ we use Eq. 4.6 to apply the model to the measured $g(\vec{r}, V)$ of individual Fe atoms by measuring the local DOS to be used in the model. The fitting parameters can be reduced to 4 independent variables which are A (over all amplitude), $|t_f/t_c|^2$(the ratio of tunneling amplitudes into the impurity ($|t_f|^2$) to the continuum ($|t_c|^2$)), E_b (the bound state energy on the impurity site), and T_k (the local Kondo temperature). Typical fitting results are shown as the dashed lines in figure 4.25, where it is clear that there is good agreement between theory and experiment. The model allows us to extract a local Kondo temperature (T_k) and local bound state energy (E_b), which when plotted against each other are observe to have large variations as shown in Figure 4.25. The apparent linear trend is unexpected, as a self-consistency model for superconductivity and the Kondo effect worked out by [57] predicts a nonlinear trend as shown in figure 4.27. However, it is possible to extract an average local Kondo temperature (T_{k_avg}) which we measure to be $29 \pm 5\,K$ which is in good agreement to the single impurity Kondo temperature measurement made by bulk

[54] which is $21 \pm 3\,K$. The linear trend shown in figure 4.8 and the increasing (T_k) spectra shown in figure 4.25 indicate that the (T_k) would be much higher in an UD doped Bi2212 Fe doped sample.

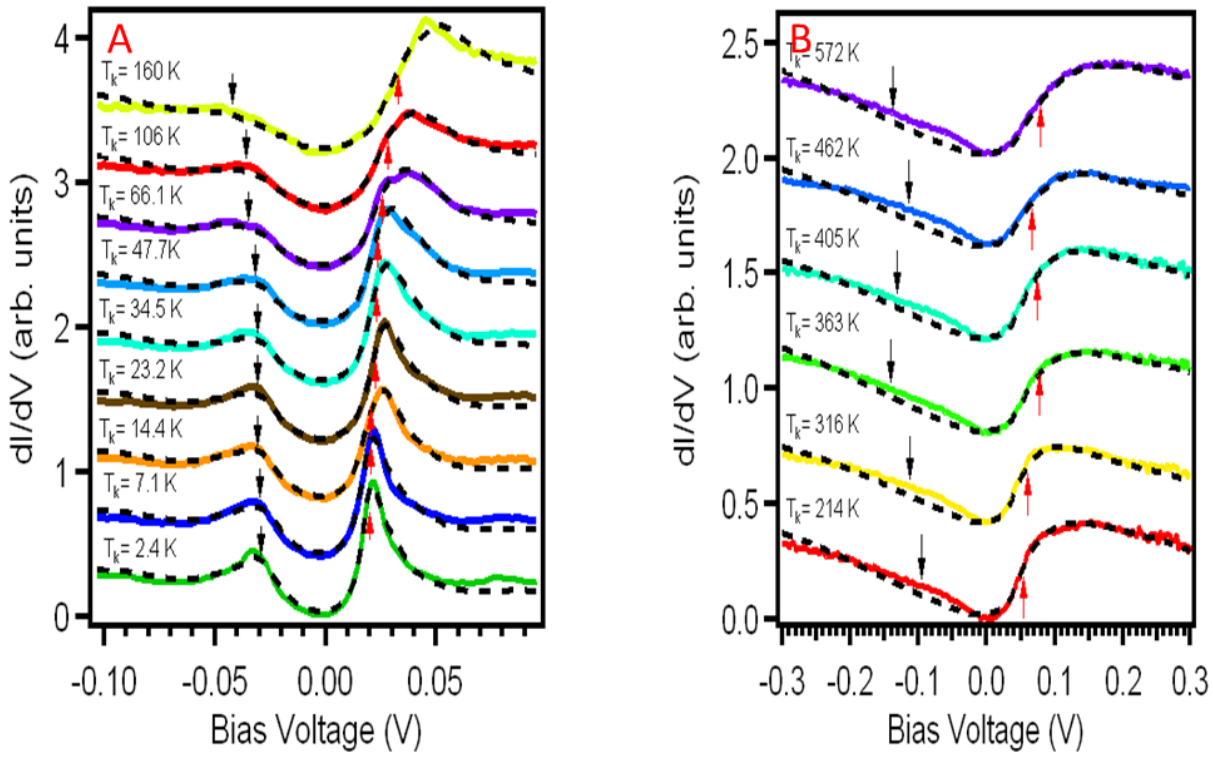

Figure 4.25: Averaged LDOS for different Fe impurities. The dashed line indicate the fit to the model from [66] using the offsite LDOS as the nonmagnetic DOS. The red arrows indicate the bound state energy (E_b) extracted from the model and the black arrows indicate the location of the superconducting gap extracted from a Dynes fitting to the electron side of the LDOS. A) Spectra averaged every 10 Fe impurities sorted by the extracted magnetic correlation temperature (T_{MC}) for OP Bi2212 with 0.5% Fe substituted for Cu at T=5.2K, with set up conditions of I_{set}=100 pA and V_{bias}=-100 mV. B) Spectra averaged every 5 Fe impurities sorted by the extracted magnetic correlation temperature (T_{MC}) for UD Bi2212 with 0.5% Fe substituted for Cu at T=5.2K, with set up conditions of I_{set}=100 pA and V_{bias}=-300 mV.

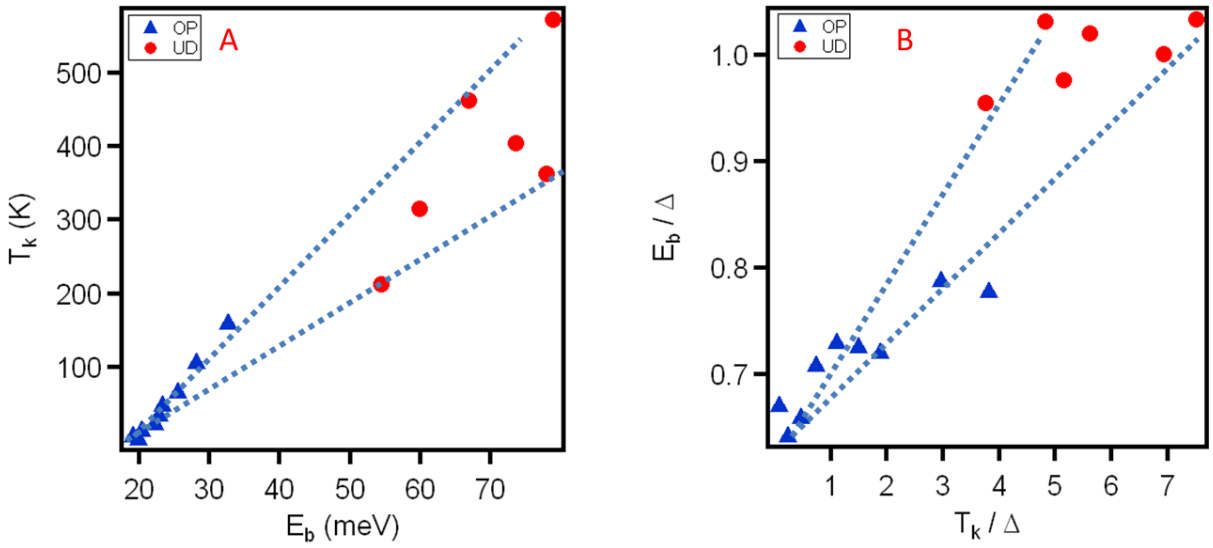

Figure 4.26: A) Relationship between the bound state energy(E_b) and the extracted magnetic correlation temperature (T_{MC}) extracted from the model in [66] using the offsite LDOS as the non-magnetic DOS. The parameters are extracted from the fits to the spectra shown in figure 4.25 A and 4.25 B for both dopings. The plot shows a linear relationship. B) Relationship between E_b and T_{MC} scaled by the superconducting gap (extracted by a Dynes fitting to the electron side of the LDOS). The data indicates a deviation from self-consistency calculations of non-disordered s-wave superconductors.

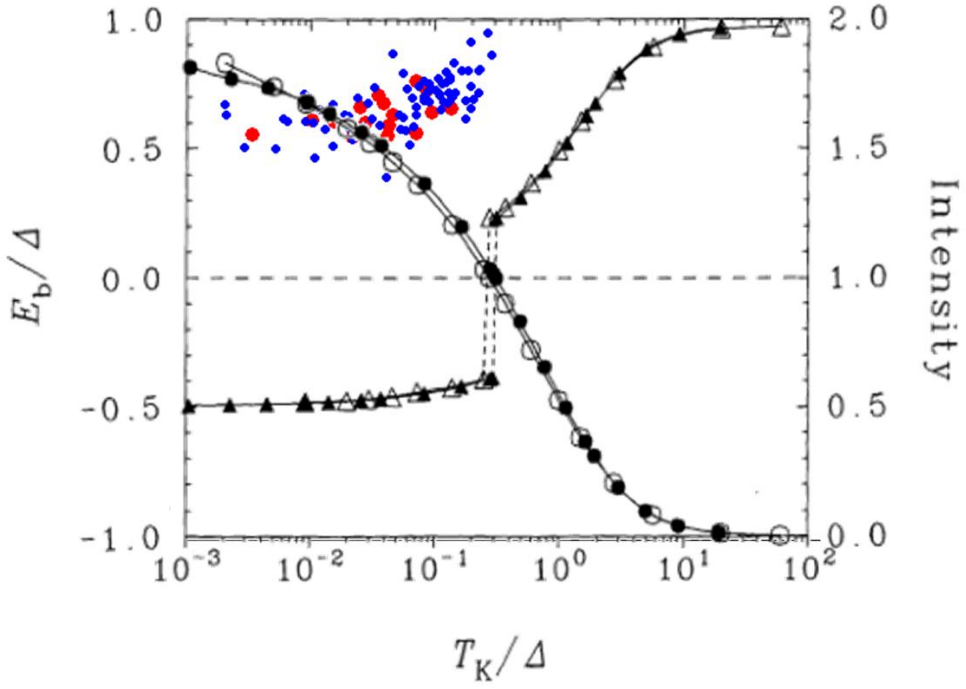

Figure 4.27: Extracted parameters from the theoretical model(the red and blue dots) of [66] from the optimally doped Bi2212 sample compared to the theoretical model of [57]. The experimental data shows a clear deviation from the expected trend.

In order to study this effect we performed SI-STM studies on a under doped grown sample with a nominal doing of 1.5% Fe and a Tc=55K. Typical spectra on Fe impurities are shown in figure 4.25 B, where it clearly seems that the large gap has become substantially larger than one would expect for a slightly under doped sample. The typical topography and LDOS($\vec{r}$,E) are shown in figure 4.28. Furthermore, when the model form [66] is applied to these spectra we measure a $T_{k\_avg} = 400 \pm 20\,K$, no bulk measurement exists as of the time of this writing for comparison. The LDOS for the under doped sample has the same spatial variation as the optimally doped sample. Therefore, SI-STM is still necessary to measure the local Kondo temperature at each impurity site.

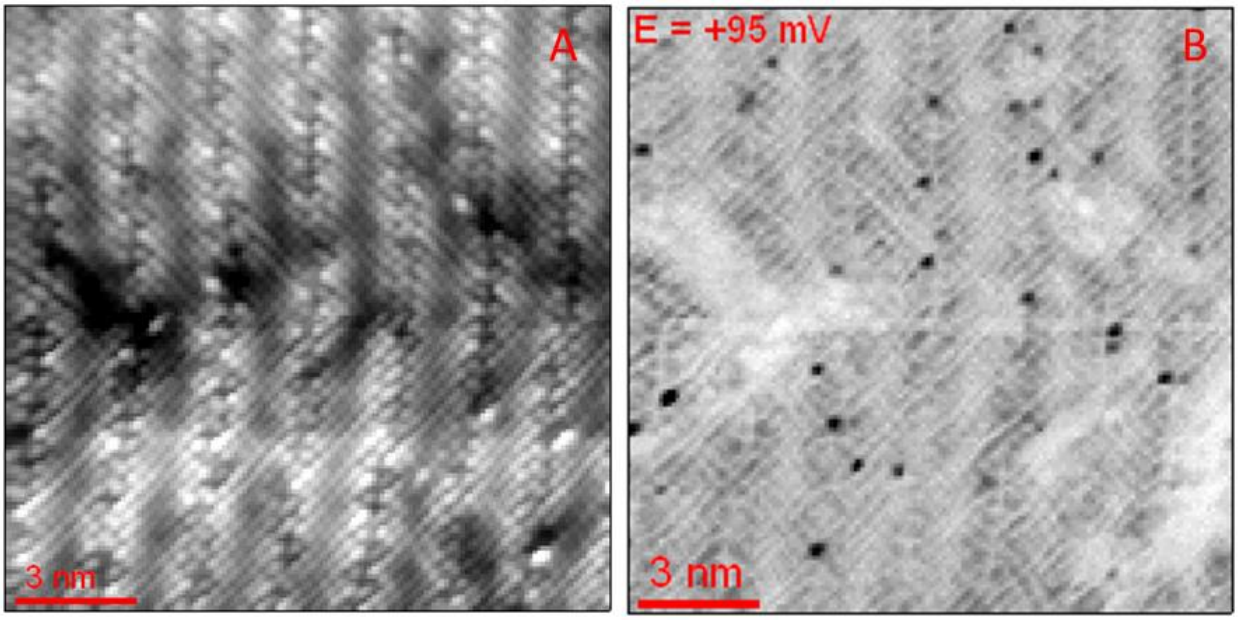

Figure 4.28: A) Typical topography in UD Bi2212 Tc=55K with 1.5% Fe conectration, with intila set up conditions of I=30pA and V=-300 mV. B) $LDOS(r, +95mV)$over the FoV in part A, withequvilant set up conditions. The localized dark spots are spectroscopic signatures of Fe impurities.

Due to the relationship found by [16] it is possible to phenomelogically relate the local gap to doping level. This was done and figure 4.29 shows the relationship

between T_k and doping across the Bi2212 phase diagram. Within this model the width (T_k) is directly proportional to the strength of the hybridization. This strength is naturally proportional to the strength of AF correlations in the layer, because the degree of compensation of a localized spin impurity in a conduction electron background will be enhanced if there is a tendency of these electrons to have a local AF order even without the spin present. The spatial variation of T_K and E_b for the various local hole doping levels then directly reflects the spatial variation and hence doping variation of the strength of AF correlations in the superconducting layer. The disappearance of T_k at a hole doping level slightly above 0.2 is indeed consistent with other observations that local AF correlations are not present at and above this doping level. The data is consistent with the magnetic ordering temperature measured [88] in YBCO.

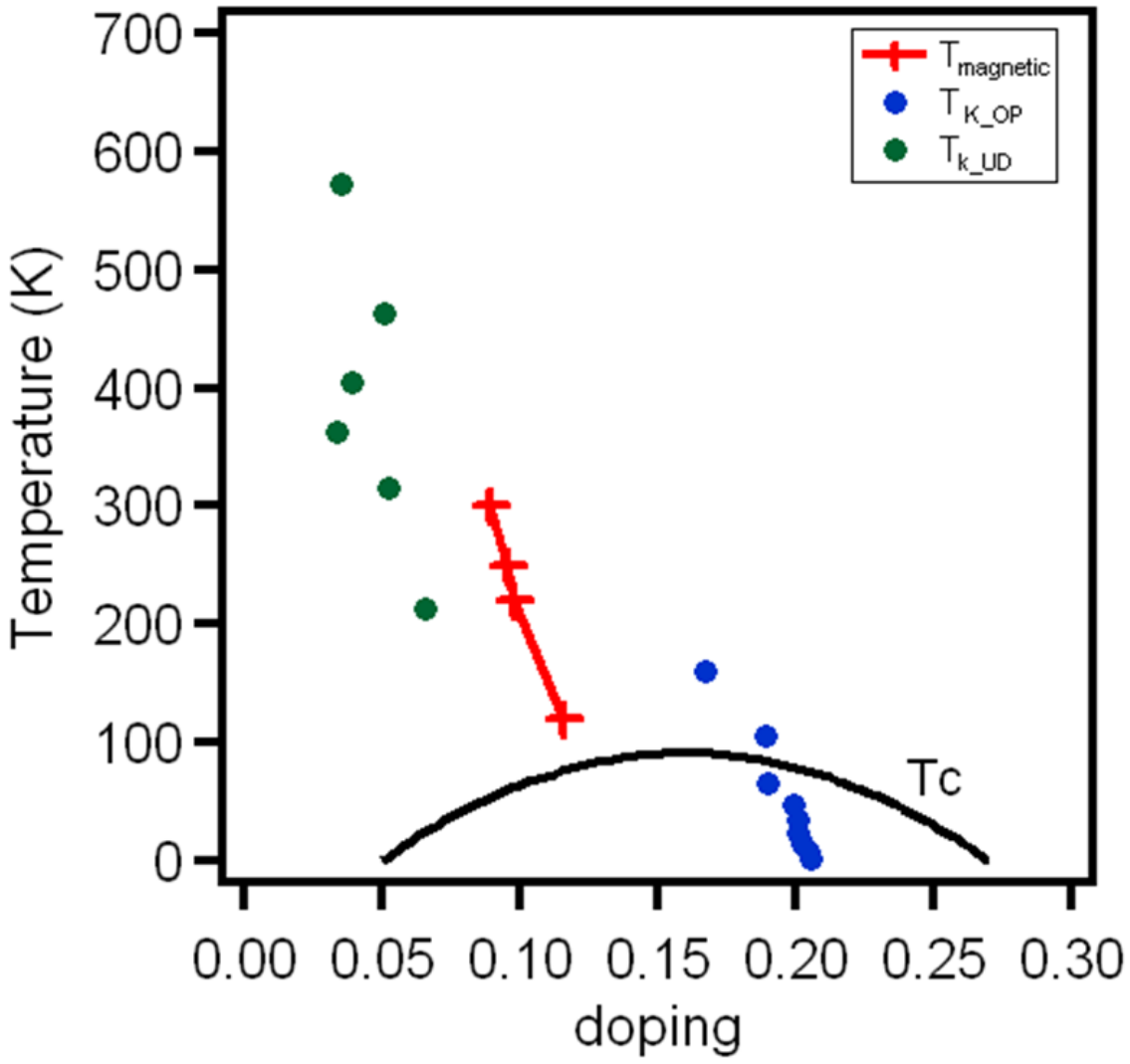

Figure 4.29: Local doping extracted from the local superconducting gap using the phenomelogical relationship from [16] vs the magnetic correlation temperature extracted from the fits to the spectra shown in figure 4.25 A and 4.25 B, where the blue markers are the T_{MC} for the OP sample and the green markers are the T_{MC} for the UD sample. The red markers indicate the magnetic gap temperature as measured by neutron scattering on a YBCO sample across the indicated doping[88]. The measured T_{MC} for BSCCO goes to 0 at a p~0.22 consistent with the theoretically predicted value for the Anti Ferromagnetic Quantum Critical Point [89].

4.8 Conclusion

Doping into a Mott insulator leads to many strange phenomena in the high temperature superconducting cuprates [90,91,92] Not only do they become

exceptional superconductors but they show a rich combination of different electronic phases throughout the underdoped part of the cuprate phase diagram .

How these different scales relate to their proximity to the Mott phase and how they compete/aide in the superconductivity remains uncertain.

By substituting Fe into the CuO2 and using the unique capabilities of SI-STM we have introduced a new technique that allows one to probe the spin degree of freedom in these materials. This is an invaluable tool towards making progress in understanding the competition between magnetism and superconductivity.

It is highly desirable to have data in severely overdoped Fe doped cuprates in order to perhaps observe the quantum phase transition hat should occur. It is also possible to dope the samples with Co instead of Fe, this should in theory introduce a higher magnetic potential which might lead to a better probe for examining the spin degree of freedom in these material. With this new probe in hand it will be possible to study the interplay of magnetism and superconductivity. Getting a handle on how these two physical phenomena compete in a system where they coexist will aid in understanding the physics of doping into a Mott insulator.

REFRENCES

[1] H. K. Onnes. Communications from the Physical Laboratory of the University of Leiden (1911).

[2] J. Bardeen, L. N. Cooper and J. R. Schrieffer, Physical Review **108,** 1175, 1957.

[3] W. Meissner and R. Ochsenfeld, Naturwissenschaften 21, 787, 1933.

[4] L.N. Cooper, Phys. Rev.,**104,** 1189, 1956.

[5] L.D. Labdau, J. Exptl. Theoret. Phys. (USSR), **30**, 1058, 1956.

[6] N.N. Bogoliubov, Nuovo Cimento, **7**, 6, 794, 1958/

[7] Maki, K., 1969, in Superconductivity, edited by R. D. Parks_Dekker, New York_, p. 1035.

[8] J. G. Bednorz and K. A. Müller, Z. Physik, B **64** (1): 189–193, 1986.

[9] Yayu Wang, S. Ono, Y. Onose, G. Gu, Yoichi Ando, Y. Tokura, S. Uchida, and N. P. Ong, Science **299**, 86, 2003.

[10] K. K. Gomes, A. N. Pasupathy, A. Pushp, S. Ono, Y. Ando, A. Yazdani, Nature **447,** 569, 2007.

[11] H. Eisaki *et al.,* Phys. Rev. B **69**, 064512, 2004.

[12] D. A. Wollman, D. J. V. Harlingen, W. C. Lee, D. M. Ginsberg, and A. J. Leggett, Physical Review Letters **71**, 2134–2137, 1993.

[13] C. C. Tsuei, J. R. Kirtley, C. C. Chi, L. S. Yu-Jahnes, A. Gupta, T. Shaw, J. Z.

Sun, and M. B. Ketchen, Physical Review Letters **73**, 593–596, 1994.

[14] S. Huefner, *et al.* Rep. Prog. Phys. **71,** 062501, 2008.

[15] M. C. Boyer*, et al.* Nature Physics **3**, 802 – 806, 2007.

[16] J. W. Alldredge, *et al.* Phys. Rev. B **85**, 174501, 2012.

[17] J.D. Fan, Y.M. Malozov, Physica C **364-365**, 101-180, 2001.

[18] M. J. Lawler, K. Fujita, Jhinhwan Lee, A. R. Schmidt, Y. Kohsaka, Chung Koo Kim, H. Eisaki, S. Uchida, J. C.Davis, J. P. Sethna & Eun-Ah Kim
Nature 466, 347–351, 2010.

[19] W. D. Wise, M. C. Boyer, Kamalesh Chatterjee, Takeshi Kondo, T. Takeuchi, H. Ikuta, Yayu Wang & E. W. Hudson Nature Physics **4**, 696 - 699 (2008).

[20] Colin V. Parker, Pegor Aynajian, Eduardo H. da Silva Neto, Aakash Pushp, Shimpei Ono, Jinsheng Wen, Zhijun Xu, Genda Gu, and Ali Yazdani,
Nature **468,** 677, 2010.

[21] Kohsaka *et al*., Science **315,** 1380-1385, 2007.

[22] E.W. Hudson *et al*., Nature **411**, 920, 2001.

[23] S.H.Pan *et al.,* Nature **403**,746, 2000.

[24] G. Binnig, H. Rohrer, Ch. Gerber, and E. Weibel, Appl. Phys. Lett., Vol. **40**, Issue 2, pp. 178-180, 1982.

[25] J. Bardeen, Phys. Rev. Lett., **6**, 57, 1961.

[26] J. Tersoff and D.R. Hamman, Phys. Rev. Lett., **50**, 1998, 1983.

[27] J. Tersoff and D.R. Hamman,PRB, **39**, 805, 1985.

[28] J. Curie and P. Curie. Comptes Rendus **91**, 383-386, 1880.

[29] G. Lippmann, J. de Phys., **10**, 381-394, 1881.

[30] G. Binning and D.P.E. Smith, Rev. Sci. Instrum. **57**, 1688-1689, 1986.

[31]http://www.efunda.com/materials/piezo/material_data/matdata_output.cfm?Material_ID=PZT-8

[32] S. H. Pan. International Patent Publication Number WO 93/19494,

International Bureau, World Intellectual Property Organization), 30

Sept. 1993.

[33] D.-J. Kim and J.-Y. Koo, Rev. Sci. Instr. **76**, 023703, 2005.

[34] K. McElroy *et al.,* Science **309**, 1048, 2005.

[35] Ilija Zeljkovic *et al.*, Science **337**, 320, 2012.

[36] K.McElroy *et al.*, Nature **422**, 592, 2003.

[37] J.E. Hoffman *et al.*, Science **297**, 1148, 2002.

[38] Norman *et al.,* PRB vol **52,** 615, 1995.

[39] U.Chatterjee *et al.*, Nature Physics vol **6**, 99, 2010.

[40] T. J. Reber *et al.*, Nature Physics **8**,606–610, 2012.

[41] Kohsaka *et al.*, Nature **454** 1072-1078, 2008.

[42] Lee *et al.*, Science **325**, 1099, 2009.

[43] K. McElroy *et al.,* PRL **96**, 067005, 2006.

[44] M. C. Asensio *et al.,* Phys. Rev. B **67**, 014519, 2003.

[45] Andersen *et al.*, J. Phys. Chem. Solids **56**, 1573, 1995.

[46] A.V. Balatsk *et al.*, Rev. of Mod. Phys. **78**, 373, 2006.

[47] Wu *et al.* ,Phys. Rev. B **62**, 14427–14430, 2000.

[48] M.Hashimoto *et al.*, PRL **106**, 167003, 2011.

[49] Mendels, P. *et al.,* Physica C **235/240**, 1595-1596, 1994.

[50] Robert Joynt , Journal of Low Temperature Physics, Vol. **109**, Nos. 5/6, 1997.

[51] Abrikosov, A. A. & Gorkov, L. P.,. Sov. Phys. JETP **12**, 1243-1253, 1961.

[52] K.J. Franke *et al.*, Science **322,** 940, 2011.

[53] A. yazdani *et al.*, Science **275,** 1767, 1997.

[54] T.M. Benseman *et al.*, PRB **84,** 144503, 2011.

[55] V. Madhavan V, W. Chen, T. Jamneala, M. F. Crommie, N. S. Wingreen, Science 280, **567**, 1998.

[56] U. Fano, PRL **124**, 6, 1961.

[57] O. Sakai et. al., Journal of the Physical Society of Japan, **69**, 3181 (1993).

[58] M.I. Salkola, A.V. Balatsky, and J.R. Schrieffer, PRB **55** ,648 (1997).

[59] Jouko Nieminen, Hsin Lin, R.S. Markiewicz, A. Bansil ,Phys. Rev. Lett. **102**, 037001, 2009.

[61] H. Shiba, Progress of Theoretical Physics **40**, 435 ,1968.

[62] M. E. Flatte and J.M. Byers, Phys. Rev. Lett. **78.,** 3761, 1997.

[63] J. Hoffman Thesis

[64] J. Li, W.-D. Schneider, R. Berndt, B. Delley, Phys. Rev. Lett. **80**, 2893, 1998.

[65] Mohammad H. Hamidian *et al.*, Proc. Nat'l Acad. Sci. **108**, 18233 - Nov 2011

[66] Marianna Maltseva, M. Dzero, and P. Coleman, Phys. Rev. Lett. **103**, 206402, 2009.

[67] T. Siegrist, S. Sunshine, D. W. Murphy, R. J. Cava, and S. M. Zahurak Phys. Rev. B **35**, 7137–7139, 1987.

[68] W.J. Zhu, Y.Z. Huang, T.S. Ning, Z.X. ZhaoMaterials Research Bulletin Volume **30**, Issue 2, February 1995, Pages 243–246.

[69] Y. Le Page et.al. Phys. Rev. B **37**, 9382–9389, 1988.

[70] Petricek, V., Gao, Y., Lee, P. & Coppens, P., Physical Review B **42**, 387-392, 1990.

[71] N.N. Kolesnikov et. al., Physica C: Superconductivity Volume **195**, Issues 3–4, 1 June 1992, Pages 219–224.

[72] Hu¨fner, S., Hossain, M. A., Damascelli, A. & Sawatzky, G. A. , Rep. Prog. Phys. **71**, 062501, 2008.

[73] Robertson, J. A., Kivelson, S. A., Fradkin, E., Fang, A. C. & Kapitulnik, Phys. Rev. B **74**,134507, 2006.

[74] Kivelson, S. A. *et al*., Rev. Mod. Phys. **75**,1201–1241, 2003.

[75] Sachdev, S., Rev. Mod. Phys. **75**, 913–932, 2003.

[76] Vojta, M., Adv. Phys. **58**, 699–820, 2009.

[77]Wilson, K.G. Rev. Mod. Phys. **47**, 773–840,1975.

[78] M. Fowler, A. Zawadowski Solid State Communications Volume **9**, Issue 8, 15 April 1971, Pages 471–476.

[79] Kenneth G. Wilson and J. Kogut Physics Reports Volume **12**, Issue 2, August 1974, Pages 75–199.

[80] Hewson AC (1993) The Kondo Problem to Heavy Fermions (Cambridge University Press, Cambridge)

[81] K. M. Lang *et al.*, Nature, vol. **415**, pp. 412-416, 2002.

[82] J. A. Slezak *et. al.*, Proc. Nat'l Acad. Sci., vol. **105**, no. 9, pp. 3203-3208, 2007.

[83] K. Gomes *et al.*, vol. **212**, pp. 460-462, 2007.

[84] G.D. Gu, vol. **137**, pp. 472-478, 1994.

[85] Dynes, R. C., Narayanamurti, V. & Garno, J. P., Phys. Rev. Lett**. 41**, 1509–1512, 1978.

[86] J. W. Alldredge *et al.* Nature Physics **4**, 319, 2008.

[87] S. Parham *et.al.*, Phys. Rev. B, vol. **87**, p. 104501, 2013.

[88] B. Fauque *et.al.* , PRL **96**, 197001 (2006)

[89] Takahiro Misawa, Masatoshi Imada ,arXiv:1306.1434 [cond-mat.str-el] (2013).

[90] A. Lee *et al.*, Reviews of Modern Physics, vol. **78**, pp. 17-85, 2006.

[91] A. Damascelli *et al.*, Journal of Electron Spectroscopy and Related Phenomena, Vols. **117-118**, pp. 165-187, 2001.

[92] P. Phillips *et al.*, Phys. Rev. Lett., vol. **95**, p. 196405, 2005.